NASA
CR
820
v.14
c.1

NASA CONTRACTOR REPORT

NASA CR-83

TECH LIBRARY KAFB, NM
0060190

NASA CR-833

LOAN COPY: RETURN TO
AFWL (WLIL-2)
KIRTLAND AFB, N MEX

ANALYSIS AND DESIGN OF SPACE VEHICLE FLIGHT CONTROL SYSTEMS

VOLUME XIV - LOAD RELIEF

by Robert D. Harris

Prepared by
GENERAL DYNAMICS CORPORATION
San Diego, Calif.
for George C. Marshall Space Flight Center

NATIONAL AERONAUTICS AND SPACE ADMINISTRATION • WASHINGTON, D. C. • AUGUST 1967

TECH LIBRARY KAFB, NM

0060190

NASA CR-833

ANALYSIS AND DESIGN OF SPACE VEHICLE FLIGHT CONTROL SYSTEMS

VOLUME XIV - LOAD RELIEF

By Robert D. Harris

Distribution of this report is provided in the interest of information exchange. Responsibility for the contents resides in the author or organization that prepared it.

Issued by Originator as Report No. GDC-DDE67-003

Prepared under Contract No. NAS 8-11494 by
GENERAL DYNAMICS CONVAIR
A DIVISION OF GENERAL DYNAMICS CORPORATION
San Diego, Calif.

for George C. Marshall Space Flight Center

NATIONAL AERONAUTICS AND SPACE ADMINISTRATION

For sale by the Clearinghouse for Federal Scientific and Technical Information
Springfield, Virginia 22151 – CFSTI price $3.00

FOREWORD

This report was prepared under NASA Contract NAS 8-11494 and is one of a series intended to illustrate methods used for the design and analysis of space vehicle flight control systems. Below is a complete list of the reports in the series:

Volume I	Short Period Dynamics
Volume II	Trajectory Equations
Volume III	Linear Systems
Volume IV	Nonlinear Systems
Volume V	Sensitivity Theory
Volume VI	Stochastic Effects
Volume VII	Attitude Control During Launch
Volume VIII	Rendezvous and Docking
Volume IX	Optimization Methods
Volume X	Man in the Loop
Volume XI	Component Dynamics
Volume XII	Attitude Control in Space
Volume XIII	Adaptive Control
Volume XIV	Load Relief
Volume XV	Elastic Body Equations
Volume XVI	Abort

The work was conducted under the direction of Clyde D. Baker, Billy G. Davis and Fred W. Swift, Aero-Astro Dynamics Laboratory, George C. Marshall Space Flight Center. The General Dynamics Convair program was conducted under the direction of Arthur L. Greensite.

TABLE OF CONTENTS

Section		Page
1	STATEMENT OF THE PROBLEM	1
2	STATE OF THE ART	3
3	RECOMMENDED PROCEDURE	9
	3.1 CRITERIA DETERMINATION	9
	3.2 CONSTRAINTS DETERMINATION	11
	3.3 CONTROL LAW SELECTION	15
	3.4 STABILITY ANALYSIS	22
	3.5 DETAILED CONSTRAINT AND CRITERIA ANALYSIS	34
	3.6 CONCLUSIONS	50
4	REFERENCES	55
Appendix		
	ATMOSPHERIC DISTURBANCES AND THEIR EFFECT ON VEHICLE LOADING	57
	A.1 INTRODUCTION	59
	A.2 DEVELOPMENT OF WIND CRITERIA	61
	A.3 QUASI-STEADY FLIGHT LOADS	62
	A.3.1 Analytical Approach	62
	A.3.2 Illustrative Example	68
	A.4 GUST RESPONSE	69
	A.4.1 Analytical Approach	69
	A.4.2 Illustrative Example	69
	A.5 COMBINED LOADS	71
	A.6 REFERENCES	73

LIST OF ILLUSTRATIONS

Figure		Page
1	Geometry of Vehicle, Pitch Plane	4
2	Comparison of Axial Loads at Burnout and Combined Axial Loads at Maximum Dynamic Pressure	10
3	Wind Profiles	17
4	Drift as a Function of Flight Time for the Saturn V Launch Vehicle — Wind No. 1: 99% Shear Peaking at 80 Sec	18
5	Drift as a Function of Time for the Saturn V Launch Vehicle — Wind No. 2: 95% Profile	19
6	Drift as a Function of Flight Time for the Saturn V Launch Vehicle — Wind No. 3: 99% Shear Peaking at 70 Sec	20
7	Planar System Diagram	24
8	Open Loop Frequency Response at Max q	25
9	Load-Reduction Autopilot Block Diagram	28
10	Low Frequency Approximation, $K_c'/(s + K_c')$, Atlas/Centaur Booster Actuator	29
11	Rigid-Body/Propellant Sloshing Stability at 84 Seconds (Maximum q, After Filter Change, No Load-Reduction Loop)	31
12	Rigid-Body/Propellant Sloshing Stability at 84 Seconds (Maximum q, After Filter Change, Load-Reduction Loop Closed)	32
13	First Elastic-Mode Stability at 80 Seconds (No Load-Reduction Loop)	33
14	First Elastic Mode Stability at 80 Seconds (Load-Reduction Loop Closed)	34
15	Autopilot Block Diagram, Load-Relief Loop	36
16	Limit Allowable Bending Moments	38
17	Avidyne Wind Profile, Montgomery, Alabama, 10 March 1955	39
18	Maximum Bending Moment Encountered During Flight	41
19	Launch Availability Sensitivity	42
20	Failure Time Analysis	43
21	Altitude Dispersions, Standard and Load Relief Autopilot (T = 102 Sec)	44

LIST OF ILLUSTRATIONS, CONTD

Figure		Page
22	Analog System Responses	47
23	Wind Schedules	48
24	Basic Gain Change Schedule	49
25	Maximum Bending Moment for 70-Second Wind	52
26a	Vehicle Responses to 70-Second Wind	53
26b	Vehicle Responses to 70-Second Wind (contd)	54
A1	Typical Wind Profile	60
A2	Coordinate System	63
A3	Vehicle Force Diagrams	64
A4	Load-Relief Autopilot Block Diagram	66
A5	Wind Speed and Direction Time History	68
A6	Centaur/Surveyor Interface Loads Due to Wind	70
A7	Centaur/Surveyor Interface Loads Due to Gust	72
A8	Atlas/Centaur Interface Bending Moments Due to Gust	73

LIST OF TABLES

Table		Page
1	Steady State Value Summary	6
2	Control Law Summary	7
3	Criteria Selection Guide	11
4	Summary of Possible Constraints	15
5	Maximum Bending Moment	21
6	Sixth-Order System	51

NOMENCLATURE

$B.M._i$	Bending moment at vehicle station i
D	Drag
d_i	Vehicle diameter at station i
g	Gravity acceleration
I_{yy}	Moment of inertia about pitch axis
j	$\sqrt{-1}$
K_A	Servoamplifier gain
K_I	Integrator gain
K_R	Rate gyro gain
K_M	Differential pressure sensor gain
K_c'	Engine servo gain
K_i	Differential pressure integral gain
K_n	Gain associated with X_n
K_v	Body axis velocity gain
$K_{\ddot{Z}_b}$	Body axis acceleration gain
$K_{\dot{Z}_I}$	Inertial axis velocity gain
$K_{\ddot{Z}_I}$	Inertial axis acceleration gain
K_α	Angle-of-attack gain
$K_{\Delta P}$	Differential pressure gain
K_θ	Displacement gyro gain

L_α	Aerodynamic load per unit angle of attack
ℓ_α	Distance from center of pressure to origin of body axis system
ℓ_c	Distance from origin of body axis system to engine gimbal point
ℓ_s	Distance from origin of body axis system to sensor location
m_T	Total mass of vehicle
q_i	Generalized coordinate of ith bending mode
s	Laplace operator $(\sigma + j\omega)$
SN	Vehicle station number
T_T	Total vehicle thrust
T_c	Control (gimbaled) thrust
V	Forward velocity of vehicle
V_w	Wind velocity parallel to Z_I axis
X_b, Y_b, Z_b	Body axis coordinates
X_I, Y_I, Z_I	Inertial axis coordinates
x_n	Output of sensor n measuring a dynamic quantity
$\ddot{Z}_{b_a}$	Body axis lateral accelerometer output
α	Angle of attack in pitch
α_w	Wind angle of attack in pitch
β	Angle of attack in yaw
ΔP	Differential pressure
δ	Engine gimbal angle
$\bar{\delta}$	Limit cycle amplitude of controlled engine
δ_c	Command signal to engines

ζ_f	Damping ratio of autopilot filter
ζ_n	Damping ratio of rigid body control mode
θ	Perturbation attitude angle
θ_c	Attitude command signal
$\dot{\theta}_i$	Output of ith rate gyro
θ_w	Wind velocity azimuth
μ_c	Control moment coefficient $= \dfrac{T_c \ell_c}{I_{xy}}$
μ_α	Aerodynamic moment coefficient $= \dfrac{L_\alpha \ell_\alpha}{I_{yy}}$
τ	Single lag filter time constant
τ_a	Single lag filter time constant for ΔP sensor dynamic model
τ_v	Single lag filter time constant for K_v feedback channel
ω	Frequency of engine gimbal limit cycle
ω_d	Vehicle lateral drift frequency
ω_f	Second order lag filter natural frequency
ω_n	Rigid body control mode natural frequency
$\cdot$	Time derivative

1. STATEMENT OF THE PROBLEM

The conventional launch vehicle autopilot (discussed in detail in Ref. 1) employs attitude and attitude rate feedback to provide stability and control of the launch vehicle and its parasitic modes. The topic of this monograph is the load-relief autopilot, which is defined as any autopilot employing an additional feedback channel or channels on a conventional autopilot baseline to alleviate vehicle loading or trajectory dispersions, or a combination of both. Use of other techniques such as seasonal pitch or yaw programs will not be discussed in detail here.

The load-relief autopilot is primarily used during the maximum dynamic pressure region of flight when wind velocities produce the largest vehicle bending moments. The time of usage is dependent, however, on the selected control law. Control law properties range from those which produce large load relief coupled with large trajectory dispersions to those which minimize trajectory dispersions and produce minimal load relief.

The analysis of a load-relief autopilot is a complex engineering task. To properly perform this task, the analyst must utilize the techniques of many technical disciplines including stability and control, structural loads, trajectory and performance, and aerodynamic heating. Constraints in each area must be adhered to, which result in compromises for the optimum overall design. In addition, hardware and reliability constraints must also be considered.

Stability requirements restrict autopilot gain and compensation values. These restrictions are determined through analyses of rigid body control, lateral drift, liquid propellant sloshing, and elastic bending modes.

Trajectory and performance analysis is necessary with a load-relief autopilot, in that the relief of loads creates trajectory dispersions of a magnitude different from those encountered with the conventional autopilot. The guidance system must allow for these dispersions and be able to correct for them. If there were no restrictions on the maneuvers which the launch vehicle might make during the powered flight, the guidance would be relatively simple, and the only major obstacle would be that of precision in guidance. However, the structural limitations due to loading and aerodynamic heating and flight performance requirements will combine to restrict the trajectory in such a way that only limited correction maneuvers can be employed.

The vehicle structure determines the limit allowable loads and hence the limit allowable bending moments. The bending moments on the vehicle during flight are imposed by axial acceleration, aerodynamic loading, propellant sloshing and rigid body control response. To get a true indication of actual flight conditions, a time-varying analysis using either design winds or statistical wind samples must be performed.

The aerodynamic heating analysis is dependent upon the vehicle trajectory. Aerodynamic heating input changes when the vehicle trajectory is altered by the wind response of the load-relief autopilot and also when these trajectory dispersions are corrected by guidance commands. Aerodynamic heating should therefore be analyzed in the same manner as the structural loading.

This monograph will describe the load-relief autopilot in enough detail to guide the analyst in application to a specific launch vehicle. Section 2, STATE OF THE ART, presents an introduction to control laws, the advantages and disadvantages of some typical control laws, and a résumé of the control laws investigated by industry and governmental institutions. Section 3, RECOMMENDED PROCEDURES, outlines five steps for analysis of load-relief autopilots with detailed examples from the references.

The load-relief autopilot is not a panacea for launch vehicles. For existing vehicles it is, however, one valid technique for possible alleviation of loads and/or trajectory dispersions. It is most powerful, however, if analyzed in conjunction with new launch vehicle designs. This allows the load-relief autopilot to help define the vehicle constraints rather than having the vehicle constraints define the load-relief autopilot.

2. STATE OF THE ART

Any discussion involving stabilization of aerodynamically unstable launch vehicles should begin with a control law. A general expression for control laws is

$$\delta = -K_A \sum_{n=1}^{N} K_n X_n \tag{1}$$

where K_n is the gain associated with X_n, a measured dynamic quantity. In this form necessary compensation for parasitic mode stabilization is neglected, allowing ease of comparison between typical control laws. The following linearized vehicle equations, to be used for this control law comparison, neglect the effects of elastic bending, propellant sloshing, engine actuator, and sensor dynamics.

$$\ddot{Z}_I = \frac{-(T_T - D)}{m_T}\theta - \frac{L_\alpha}{m_T}\alpha + \frac{T_c\delta}{m_T} \tag{2}$$

$$\ddot{\theta} = \mu_\alpha \alpha + \mu_c \delta \tag{3}$$

$$\alpha = \theta + \frac{\dot{Z}_I}{V} + \alpha_w \tag{4}$$

Figure 1 is a diagram of the coordinate systems associated with these equations.

Autopilot transient effects may be obtained by examination of the characteristic equation. To calculate this equation, assume a control law of the form

$$\delta = -K_A(K_\theta \theta + K_R \dot{\theta} + K_\alpha \alpha) \tag{5}$$

From Eq. (2) through (5) the characteristic equation can be shown as

$$\begin{aligned} s^3 &+ s^2\left[\mu_c K_A K_R + \frac{T_c}{mV}\left(K_A K_\alpha + \frac{L_\alpha}{T_c}\right)\right] \\ &+ s\left[\mu_c K_A(K_\theta + K_\alpha) - \mu_\alpha + \frac{K_A T_c K_R}{m_T V}\left(\mu_\alpha + \frac{\mu_c L_\alpha}{T_c}\right)\right] \\ &+ \frac{T_c K_A K_\theta}{m_T V}\left(\mu_\alpha + \frac{\mu_c L_\alpha}{T_c}\right) - \frac{(T_T - D)}{m_T V}(\mu_c K_A K_\alpha - \mu_\alpha) = 0 \end{aligned} \tag{6}$$

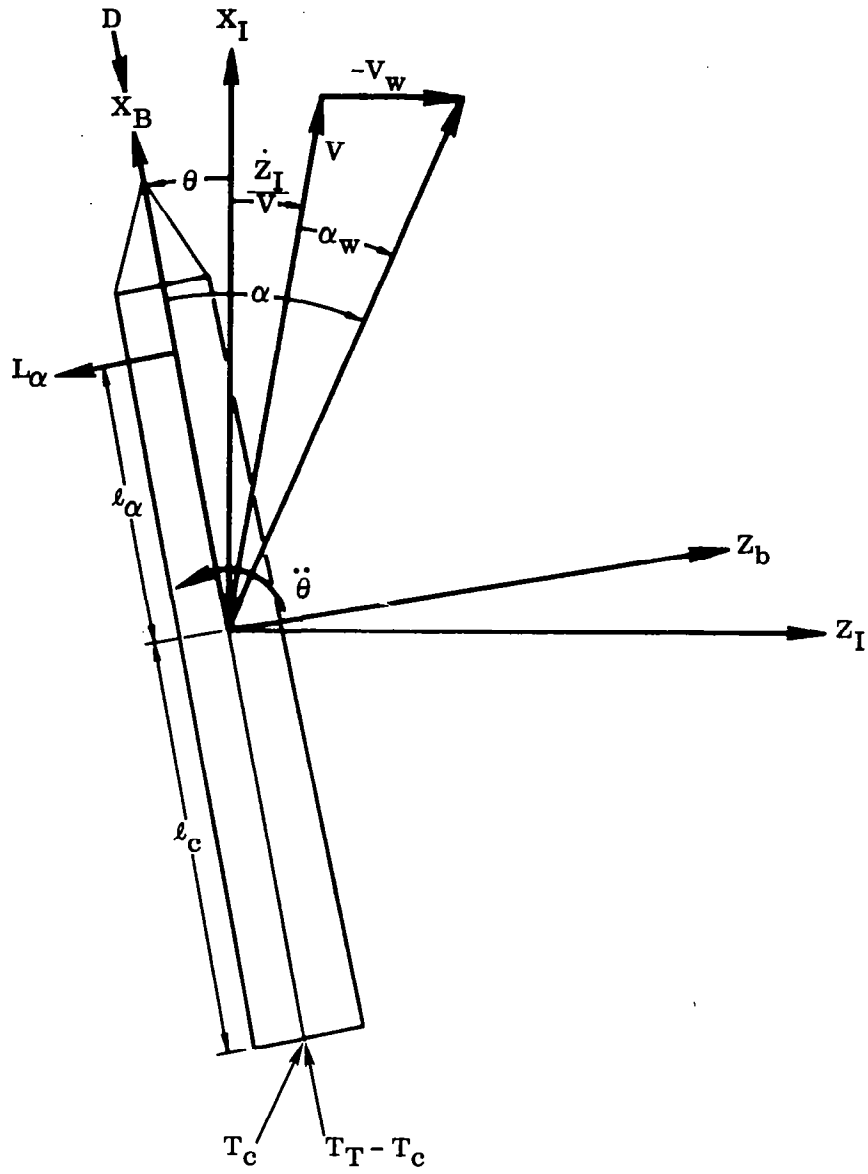

Figure 1. Geometry of Vehicle, Pitch Plane

The three roots are a complex conjugate pair associated with the rotation of the vehicle about its center of gravity (rigid body control mode) and a single root associated with the lateral drift of the flight path in response to wind.

The lateral drift root during the flight time of interest is small compared with the value of the rigid body control mode roots and therefore can be ignored.

The same results can be obtained by a derivation ignoring the lateral drift of the flight path, Eq. (2). Thus, substituting Eqs. (4) and (5) into (3)

$$\theta = \frac{\left[\mu_c K_A K_\alpha - \mu_\alpha\right]\left[\frac{\dot{Z}_I}{V} + \alpha_w\right]}{s^2 + \mu_c K_A K_R s + \mu_c K_A (K_\theta + K_\alpha) - \mu_\alpha} \tag{7}$$

Comparison of the denominator of Eq. (7) and the system characteristic equation, Eq. (6), shows the terms containing vehicle velocity, V, in the characteristic equation have been removed.

A "quasi-steady-state" will be defined as the condition when the derivatives of θ in Eq. (7) are set equal to zero. Performing this operation on Eq. (7) and manipulating the resulting equation with Eqs. (2), (3), and (4) produces quasi-steady-state equations for α, δ and $\dot{Z}_I$. Table 1 shows these equations for four typical control laws. The $\dot{Z}_I$ term is a measure of vehicle trajectory dispersion. Bending moments on the vehicle at any station i can be represented by $B.M._i = M_{\alpha_i}\alpha + M_{\delta_i}\delta$. Hence, α and δ are indications of vehicle loading.

The first control law in Table 1 is the attitude control law which utilizes attitude error and body rate for control and stability respectively. The drift velocity is a single time-lag function of the autopilot and vehicle parameters. Because $K_A K_\theta \mu_c > \mu_\alpha$ for rotational stability, the drift velocity approaches the product of the wind angle of attack and vehicle velocity. The direction of drift is with the wind. The engine gimbal angle is a function of the gain, K_θ, of the position reference. As K_θ increases, the engine gimbal decreases. The same is true for the angle of attack which decreases as K_θ increases. The upper value of K_θ is limited, however, by stability when higher order system dynamics and parasitic modes are considered.

Application of the load-relief control law with angle-of-attack feedback exhibits the same vehicle properties as the attitude control law. In addition, as K_α is increased, the values of α and δ decrease. This provides an additional control variable to adjust. The gain, however, has a lower and upper bound based on stability. The lower bound is $\mu_c K_A (K_\theta + K_\alpha) > \mu_\alpha$ for rotational stability. When the autopilot gains are such that $(T_T - D)(\mu_c K_A K_\alpha - \mu_\alpha) > K_A K_\theta (\mu_\alpha T_c + \mu_c L_\alpha)$ the vehicle changes drift direction and drifts into the wind. This drift mode is an unstable mode but may be tolerated for short periods of time.

A special case of the load-relief mode is the minimum drift control law. The gain criterion for this law is $(T_D - D)(\mu_c K_A K_\alpha - \mu_\alpha) = K_A K_\theta (\mu_\alpha T_c + \mu_c L_\alpha)$. This mode produces a zero steady-state drift while the load relief remains as discussed above. Vol. III, Part I of this series of monographs (Ref. 1) presents a comparative final value analysis which indicates that the drift velocity for a step input wind angle of attack is reduced by over a factor of 50 when comparing the drift minimum control law to either the attitude or load-relief control laws.

The last control law presented on Table 1 is minimum load. The control equation indicates that this mode does not use an attitude error feedback ($K_\theta = 0$) and results in

Table 1. Steady State Value Summary

CONTROL LAW	EQUATION	LATERAL VELOCITY, $\dot{Z}_I$	ENGINE CONTROL ANGLE, δ	ANGLE OF ATTACK, α
Attitude	$\delta = -K_A(K_\theta\theta + K_R\dot{\theta})$	$\dfrac{-\alpha_w V}{\dfrac{s}{\dfrac{K_A K_\theta(\mu_\alpha T_c + \mu_c L_\alpha) + (T_D - D)\mu_\alpha}{m_T V(\mu_c K_A K_\theta - \mu_\alpha)}} + 1}$	$\dfrac{-\left[\dfrac{\dot{Z}_{ss}}{V} + \alpha_w\right]}{\dfrac{\mu_c}{\mu_\alpha} - \dfrac{1}{K_A K_\theta}}$	$\dfrac{\left[\dfrac{\dot{Z}_{ss}}{V} + \alpha_w\right]}{1 - \dfrac{\mu_\alpha}{K_A K_\theta \mu_c}}$
Load Relief	$\delta = -K_A(K_\theta\theta + K_R\dot{\theta} + K_\alpha\alpha)$	$\dfrac{-\alpha_w V}{\dfrac{s}{\dfrac{K_A K_\theta(\mu_\alpha T_c + \mu_c L_\alpha) - (T_D - D)(\mu_c K_A K_\alpha - \mu_\alpha)}{m_T V[\mu_c K_A(K_\theta + K_\alpha) - \mu_\alpha]}} + 1}$	$\dfrac{-\left[\dfrac{\dot{Z}_{ss}}{V} + \alpha_w\right]}{\dfrac{\mu_c}{\mu_\alpha} + \dfrac{K_\alpha \mu_c}{K_\theta \mu_\alpha} - \dfrac{1}{K_A K_\theta}}$	$\dfrac{\left[\dfrac{\ddot{Z}_{ss}}{V} + \alpha_w\right]}{1 + \dfrac{K_\alpha}{K_\theta} - \dfrac{\mu_\alpha}{K_A K_\theta \mu_c}}$
Minimum Drift	$\delta = -K_A(K_\theta\theta + K_R\dot{\theta} + K_\alpha\alpha)$ with $K_A K_\theta \mu_\alpha + K_A K_\theta \mu_c L_\alpha = (T_D - D)(\mu_c K_A K_\alpha - \mu_\alpha)$	0	$\dfrac{-\left[\dfrac{\dot{Z}_{ss}}{V} + \alpha_w\right]}{\dfrac{\mu_c}{\mu_\alpha} + \dfrac{K_\alpha \mu_c}{K_\theta \mu_\alpha} - \dfrac{1}{K_A K_\theta}}$	$\dfrac{\left[\dfrac{\dot{Z}_{ss}}{V} + \alpha_w\right]}{1 + \dfrac{K_\alpha}{K_\theta} - \dfrac{\mu_\alpha}{K_A K_\theta \mu_c}}$
Minimum Load	$\delta = -K_A(K_R\dot{\theta} + K_\alpha\alpha)$	$\dfrac{\alpha_w V}{\dfrac{s}{\dfrac{(T_D - D)}{m_T V}} - 1}$	0	0

zero values for α and δ, causing the vehicle to turn and drift into the wind. This control law produces large trajectory dispersions due to this lack of attitude reference and the unstable lateral drift mode.

From this brief discussion it would appear easy to select a control law meeting the criteria imposed by the study. However, the selection is guided not only by the study criteria but also by the constraints imposed by the autopilot, vehicle, and mission. Table 2 is a résumé of the control laws that have been investigated by various private and governmental institutions. As the table indicates, the control laws extend from the previously discussed minimum drift concept to forms utilizing body and inertial coordinate system dynamic quantities in various combinations. The methods used to arrive at a control law and complete the required analyses are explained in the next section.

Table 2. Control Law Summary

DYNAMIC QUANTITY USED IN CONTROL LAW	REFERENCE NUMBER																									
	2	2	2	2	3	3	4	4	4	5	6	6	6	6	6	7	7	7	8	8	8	9	9	9	10	11	11	12	12
θ			▨	▨	▨	▨	▨	▨	▨	▨	▨	▨	▨	▨	▨	▨	▨	▨	▨	▨	▨	▨	▨	▨	▨	▨	▨	▨	▨
$\dot{\theta}$	▨	▨	▨	▨	▨	▨	▨	▨	▨	▨	▨	▨	▨	▨	▨	▨	▨	▨	▨	▨	▨	▨	▨	▨	▨	▨	▨	▨	▨
α	▨		▨		▨			▨		▨		▨															▨		
$\int \alpha dt$					▨					▨		▨																	
$\ddot{Z}_b$		▨		▨		▨					▨																		
$\int \ddot{Z}_b dt$						▨	▨				▨					▨		▨				▨		▨		▨			
$\ddot{Z}_I$														▨							▨								
$\int \ddot{Z}_I dt$														▨						▨					▨	▨	▨	▨	▨
$\int\int \ddot{Z}_I dt dt$																	▨	▨	▨										
$\ddot{Z}_b / \ddot{X}_b$									▨								▨	▨											
$\int (\ddot{Z}_b / \ddot{X}_b) dt$									▨																				
δ													▨																
q_1, q_2																												▨	
V_w																							▨						
ΔP															▨														
$\int \Delta P dt$															▨														

3. RECOMMENDED PROCEDURE

As in conventional autopilot analyses, the load-relief autopilot design must proceed through discrete phases, beginning with the determination of the goals of the study, usually in terms of required load alleviation and allowable trajectory dispersion. The next phase is the determination of all constraints on the analyses to serve as a guide in all remaining phases of analyses. Determination of a desirable control law utilizing highly simplified mathematical models then completes the foundation for detailed analyses. Detailed analyses utilizing more sophisticated and more correct mathematical models are then performed in the areas of stability and control, trajectory and performance, structural loading, aerodynamic heating, and reliability. This section presents a detailed résumé of these phases with supporting examples from the references.

3.1 CRITERIA DETERMINATION

In organizing a study to investigate load reduction methods, it is necessary to decide upon a criterion in terms of trajectory dispersions or load alleviation. The following discussion, based on Ref. 9, is primarily concerned with load alleviation as its criterion. For a given launch vehicle there is a definite lower limit below which there is no reason to reduce the bending loads, since there is always a point at which some condition other than bending load becomes critical. For typical large boosters, the axial load at burnout is higher than in the high dynamic pressure region. Thus if the bending load in the high dynamic pressure region becomes small enough, the combined loading due to bending and axial load will be less than the axial load at burnout. Therefore, there is a definite goal to strive for in load alleviation; and when this goal has been attained, further alleviation at the expense of additional drift or control system complexity is unwarranted.

To establish this goal for Marshall Space Flight Center (MSFC) model vehicle No. 2, axial load and bending moment time histories in response to the MSFC synthetic wind profile with embedded jet are calculated using a conventional attitude control system and time-varying digital loads calculation. The axial load at first-stage burnout (maximum axial load factor) and the combined axial load and bending moment at maximum dynamic pressure are shown in Fig. 2. Bending moment is converted to an equivalent axial load by the formula:

$$(\text{Axial Load})_{\text{equiv.}_i} = 4\ (\text{B.M.})_i/d_i$$

where d_i is the section diameter. As can be seen, the axial load at burnout will provide the design load for the central part of the vehicle, while the forward portion will be designed by the loads occurring during the maximum dynamic pressure portion of the trajectory. Looking at the loads at station 91 m., the bending moment due to wind

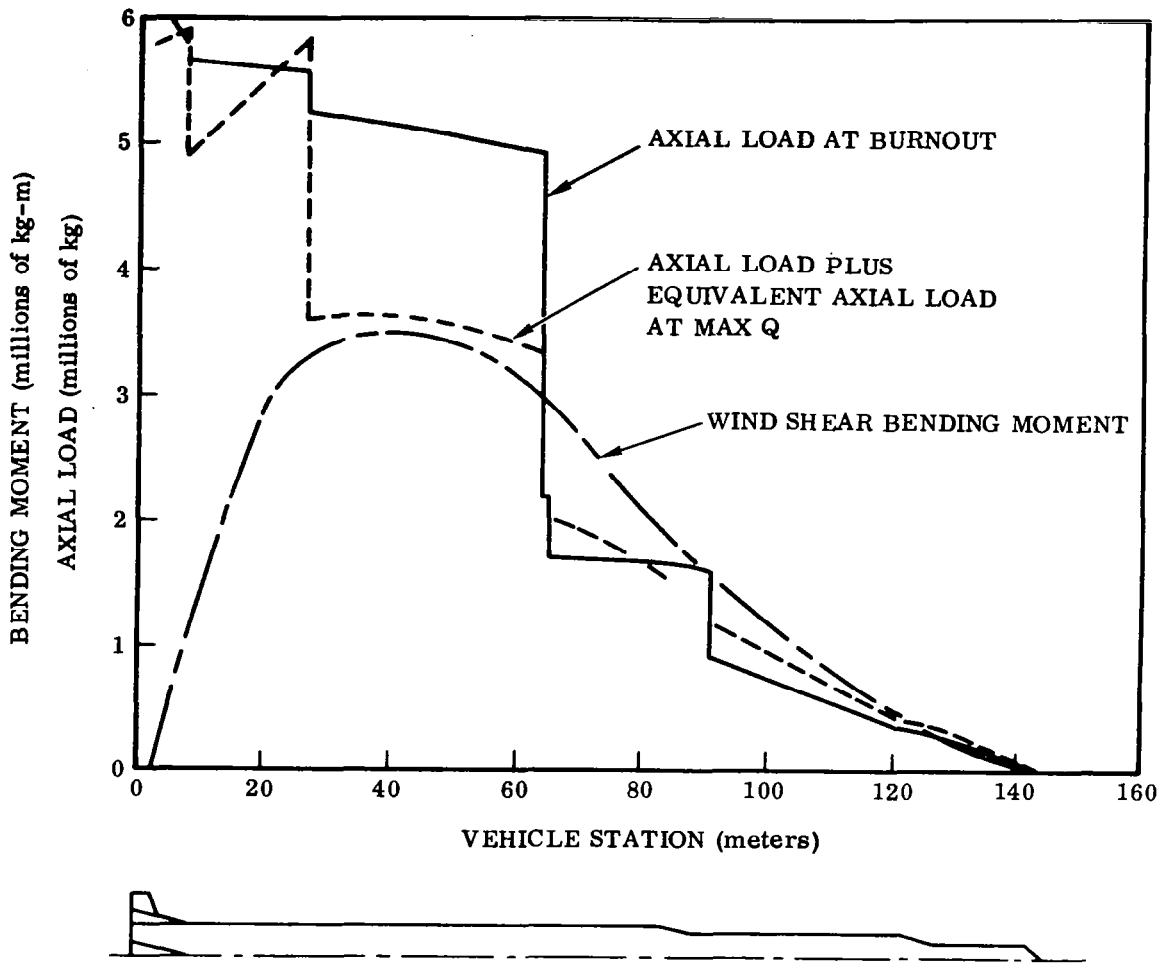

Figure 2. Comparison of Axial Loads at Burnout and Combined Axial Loads at Maximum Dynamic Pressure

shear must be reduced 38% to produce combined loads at maximum dynamic pressure equal to the axial load at first-stage burnout. If this goal is achieved, the maximum wind shear bending moment on the vehicle will be 2.2×10^6 kg.-m. at or near station 46.8 m., assuming uniform load reduction at all stations.

This example is one criterion applied as a basis for load-relief studies. The tradeoffs between load-relief and trajectory dispersion were discussed briefly in Section 2. In order to determine a valid criterion, these tradeoffs must be considered. Table 3 presents a guide for criteria selection in terms of vehicle trajectory, vehicle loading, and payload capability. The upper half of the table relates vehicle loading to trajectory; the lower half relates vehicle loading to payload capability. This table is

Table 3. Criteria Selection Guide

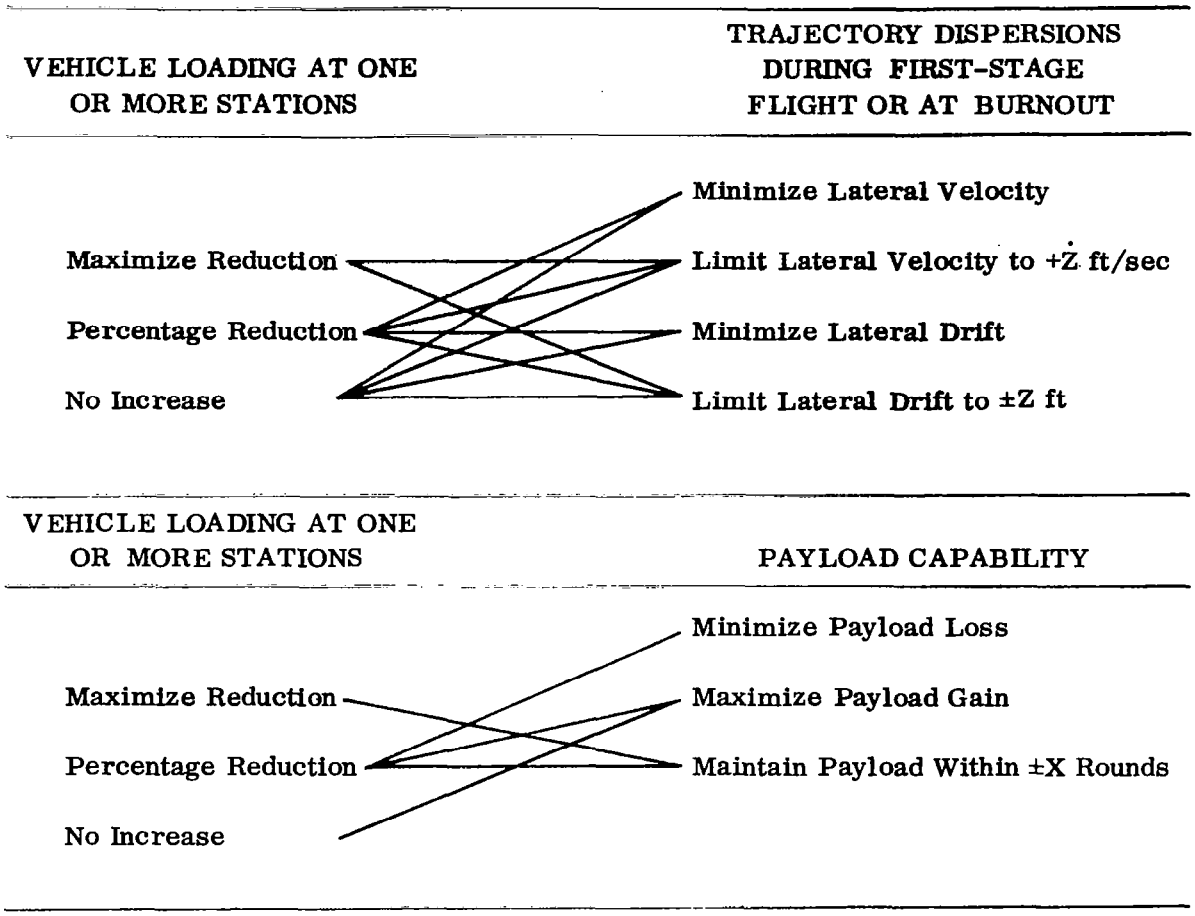

easily extended. For example, payload capability could be expressed as velocity at first-stage burnout and vehicle loading as launch availability. The black lines indicate possible combinations that can be utilized in establishing a criterion. Combinations of items not connected should be approached with caution. A typical non-joined set is "maximize load reduction and minimize lateral velocity." Section 2 shows that maximum load relief is not compatible with minimum drift.

After selection of a criterion, the study proceeds to definition of the constraints. The ability to satisfy the selected criterion is primarily dependent on the constraints imposed by the mission, vehicle, and autopilot as discussed in the next section.

3.2 CONSTRAINTS DETERMINATION

The constraints imposed on the load-relief study include allowable time and budget, mission requirements, vehicle constraints, and autopilot constraints. This phase of the analysis is often overlooked or minimized, resulting in wasted effort by proceeding

along a path leading to an unacceptable solution when a covert constraint is discovered. The detail that is necessary to prevent this occurrence is demonstrated by the following discussion of autopilot constraints from Ref. 6. In particular this example is primarily concerned with load-relief sensors. Several different load-reduction laws have been considered which differ chiefly in the type of sensor employed. The initial constraint of this study was that the existing autopilot configuration must be maintained and that changes would be in the form of an additional loop or loops to provide load relief.

A load-reduction autopilot which uses a lateral, body-fixed accelerometer sensor was the earliest system to be studied in detail, since it was felt at the time to be more feasible than systems employing aerodynamic sensors. In such a system, the accelerometer senses both the lateral acceleration of the vehicle produced by the aerodynamic loading and the thrust-vector deflection generated in response to this loading. At low frequencies, the signal is proportional to the lateral forces divided by the vehicle mass. The gain characteristic of the system is less than optimum, however, since the vehicle drift rate which it commands at later flight times, when the mass is reduced, is greater than necessary. Moreover, alignment of the sensitive axis of the accelerometer is critical. Any misalignment causes an appreciable component of the thrust acceleration to be picked up and interpreted as lateral acceleration. Since the maximum lateral acceleration due to wind is less than 0.3 g, only a small misalignment is required to produce a large error in the sensor signal. The second disadvantage of a $\ddot{Z}_b$-loop system is its sensitivity to parasitic modes of oscillation. The longitudinal location, or station number, of the accelerometer is critical. If the sensor is situated too far forward, the system is difficult to stabilize in body bending. On the other hand, in order to maintain rigid-body stability, it must be located ahead of the vehicle's center of percussion (as defined with respect to the engine gimbal point). This dictates a compromise location in the interstage adapter area, close to, but ahead of the first-mode node (point of zero deflection due to first-mode bending). A third major disadvantage is the severe vibration environment present in the interstage adapter. The instrument must therefore measure low-frequency, low-amplitude accelerations with accuracy while rejecting high-frequency, high-level accelerations. For these reasons, no attempt has been made to synthesize such an autopilot for Atlas/Centaur.

One of the sensors flown on the first Atlas/Centaur was the Edcliff conical transducer. This instrument has undergone a lengthy development program and gave good measurements of the angle of attack on this flight — with the exception of a large bias error, due to electrical bias and/or sensor misalignment. A load-reduction autopilot could be designed using this sensor, but it would require continuously programmed gains in a manner similar to that of a system flown by Marshall Space Flight Center. The gain variation is necessary in order to duplicate the change in aerodynamic loading occurring with changing dynamic pressure and changes in angle of attack, as measured by the sensor. The Atlas/Centaur autopilot does not lend itself to such changes. In addition, the location of the boom could cause a stability problem because of a

possible "flyrod effect" in the boom. This would occur at the higher bending frequencies — those for which the analysis is least accurate.

A similar system, using vanes mounted on the nose fairing, was rejected for similar reasons and also because of the inadequately evaluated effect of upwash-flow close to the nose fairing, which could lead to erroneous measurements of the angle of attack.

Under trim conditions, the thrust-vector deflection angle, δ, is approximately proportional to the aerodynamic loading on the vehicle. The engine-deflection angle can be sensed either through the feedback transducer or through the engine command signal, offering the advantage of requiring no auxiliary sensors. However, the stability properties of the system suffer from the fact that the engine position is delayed by the response time of the autopilot. This implies that the rigid body stability will suffer and that achievement of a relatively high gain in the auxiliary loop is precluded. On the other hand, the stability of the sloshing and bending modes is good.

The major defect of the δ-loop system is that of misalignment. In order that the system be workable, some means of eliminating uncertainties in the position of the booster engine is mandatory.

The misalignment problem places it at a considerable disadvantage at the present time; hence, no attempt has been made to synthesize an autopilot for Atlas/Centaur using this scheme.

It is possible to use the accelerometers mounted on the inertial platform, in conjunction with the on-board guidance computer, to determine the proper heading for the Atlas/Centaur in the presence of wind. A system of this nature has by far the largest potential of any load-reduction scheme, since the guidance computer could be capable of tailoring the vehicle commands to minimize loads and trajectory dispersions in a fashion dependent upon wind conditions actually existing, rather than upon some preprogrammed estimate of conditions. Such a system, however, is sensitive to computational lags within the digital computer loop as well as being sensitive to parasitic modes of vibration in much the same manner as the lateral-accelerometer system. Unfortunately, the development time for such a system would be prohibitive as the system requires capabilities beyond those of the present guidance computer.

A fifth type of system uses the difference in pressure measured between two ports on opposite sides of the nose fairing as a measure of the aerodynamic loading. The differential pressure measured is directly proportional to the product of the angle of attack (in the plane of the ports) times the dynamic pressure. There is, in addition, a small variation due to changes in Mach number, which is equivalent to a change in gain. Two types of differential-pressure sensors were considered which differ only in the location of their pressure ports. Though both sensors depend upon the differential pressure between their opposing sensor ports, the first is called the ΔP-sensor merely to distinguish it from the second, or "Q-ball," sensor. The ΔP-sensor uses pressure

ports located about half-way down the conical section of the nose fairing at points 45 degrees away from the vehicle axes. The signals are resolved to obtain the equivalent signals as if measured in the pitch and yaw planes. The ports are located at 45 degrees to mitigate surface-flow effects which might otherwise predominate if one set of ports were located next to the nose-fairing split line. This particular form of differential-pressure (ΔP) sensor is slightly nonlinear in that the pressure difference measured with one pair of ports is dependent not only upon the dynamic pressure, the Mach number, and the angle of attack in the plane of the ports, but also upon the angle of attack in the other plane. This nonlinearity influences the effective gain of the sensor to a small extent, depending upon the circumferential direction (with respect to the vehicle centerline) of the relative wind vector. Nevertheless, it is not judged to be a difficulty from the flight-control standpoint.

The ΔP-sensor is inherently least sensitive to sensor misalignment and is relatively insensitive to mislocation of the pressure ports. In fact, the largest error is likely to lie in the electrical bias rather than in misalignment of the sensors.

The second type of differential-pressure sensor, the so-called Q-ball, uses three pairs of pressure ports located on the hemispherical tip of the nose fairing. The first pair is located in the pitch plane at 45 degrees of latitude on the spherical surface. The second pair is situated similarly, but in the yaw plane. The third pair is used only for purposes of instrumentation, i.e., for direct measurement of the dynamic pressure. The first two pairs of ports are used to measure the aerodynamic loading in a manner similar to that of the ΔP-sensor except that no resolution of the signals is required. The fact that this sensor is located on the tip of the nose fairing makes it somewhat more sensitive to port location errors. A hundredth-of-an-inch mislocation of one port can result in a sensor misalignment of almost 0.05 degree. It is felt that manufacturing tolerances can be held more closely than this and that the misalignment, though worse than that possible with the ΔP-sensor, is nevertheless smaller than that of any other sensor discussed. Moreover, the nonlinearity which would impair the ΔP-system, viz., dependence of the sensor signal upon circumferential orientation of the relative wind vector, is not present in the Q-ball sensor.

The two differential-pressure sensors are substantially identical in their effects on vehicle dynamics and can be analyzed simultaneously. It is felt at this time, however, that the Q-ball, despite its inherently greater misalignment error, is slightly better as a sensor for the load-reduction autopilot. The Q-ball sensor requires no signal resolving and no pneumatic-line disconnects at the nose-fairing split-line, and has no nonlinearity dependent upon wind direction. From the standpoint of dynamic requirements, however, either is acceptable on the basis of what is presently known.

The above example describes one typical autopilot constraint evaluation. The allowable time and budget constraint needs no further amplification. It will be of value, however, to summarize constraints applicable to the mission, launch vehicle, and autopilot. This summary (see Table 4) will then serve as a check list to the analyst preparing to

Table 4. Summary of Possible Constraints

MISSION	LAUNCH VEHICLE	AUTOPILOT
Payload Requirement	Allowables	Allowables
Trajectory Dispersions	Bending Moment	Activation Time for L.R.
Launch-Window	Axial Load	Channels for L.R.
Hour	Aerodynamic Heating	Compensation for L.R. Channels
Day	Engine Gimbal Angles	Gain Switching
Month	Stability Margin	Reliability
Guidance	Bending	Allowable Decrease Due to Increased Components
Capability	Sloshing	Prelaunch Testability
Antenna Look Angle (Radio Guidance)	Rigid Body	Restrictions
Open Loop Steering	Allowable Initial Conditions for Second Stage Separation	Use of Existing Autopilot
Pitch	αq	Sensor Selection
Yaw	Vehicle Rate	
Roll	Attitude Error	
Wind Criteria		
Required Launch Availability		

study in detail load-relief autopilots. Although some constraints may seem trivial or may have already been considered in selection of a criterion, they have been repeated for completeness.

3.3 CONTROL LAW SELECTION

Selection of a control law and autopilot predesign are best accomplished using rigid body techniques. This allows the analyst to develop the necessary "feel" for the physical phenomena which are usually encountered in more complex analyses.

The rigid body study based on Ref. 8 and described in the following paragraphs was performed to provide data for comparing the drift and bending moments of drift-minimizing control systems using angle-of-attack or body-mounted lateral accelerometer feedback to a system using velocity perpendicular to the reference trajectory. As a baseline, the attitude control law was included.

Time histories of the rigid body response for the first-stage flight were obtained for these four types of feedback (attitude control, angle of attack, body accelerometer, and velocity meter) using a digital computer program. The simulated vehicle was subjected to each of the following wind profiles: 1) wind no. 1, a 95% maximum wind with 99% wind shears peaking at 80 seconds flight time, 2) wind no. 2, a 95% maximum wind profile, and 3) wind no. 3, a 95% maximum wind with 99% shears peaking at 70 seconds flight time (Fig. 3).

The feedback gains were calculated to yield a system with a rigid body control mode frequency (ω_n) equal to 1.3 rad/sec and a damping ratio (ζ_n) equal to 0.707. Gains were calculated for flight times of 30, 60, 80, and 140 seconds. All systems were flown with attitude control only for the first 40 seconds of flight. An interval of five seconds was then allowed for the gains to change to the 60-second flight time values. At 67.5 seconds to 72.5 seconds, the change was made to the 80-second flight time gain values. At 105 seconds to 110 seconds, the gains were changed to the values calculated for 140 seconds flight time.

For the cases of angle-of-attack and accelerometer feedback, the lateral drift root (ω_d) was given a value of zero. A value of ω_d equal to 0.2 sec was considered in the variable time analysis of velocity meter feedback. Figs. 4, 5, and 6 show the drift (Z_I distance off trajectory) for the various control laws as a function of flight time for each of the three wind profiles. The velocity meter feedback system has a lower drift value than the angle-of-attack and accelerometer systems for the 95% profile wind, but has a higher value for the shear winds. The maximum drift for any of the drift minimizing systems was 1.23 kilometers for the accelerometer feedback system with 95% maximum wind profile applied. The maximum drift for the velocity meter feedback system occurred with this wind and was 0.64 kilometers.

The drift rate ($\dot{Z}_I$) response of the system with velocity feedback follows the wind inputs. The angle-of-attack and acceleration feedback systems have regions where drift rate reverses for the high shear winds, even though winds are always in the same direction. This occurs at flight times where gains are not absolutely correct. If the combination of gains had not been such that reversals in drift rate occurred over part of the flight, the drift for the acceleration and angle-of-attack feedback systems would have exhibited higher values. Also of significance is the drift rate at burnout. The drift rate for the velocity feedback system approaches zero at burnout for all winds, while the other systems approach some non-zero, steady-state value.

Table 5 presents α and β along with the bending moments for the 60, 70, and 80 second flight times respectively for each of the three wind profiles. For the three winds, the maximum bending moment occurred at 70 seconds flight for wind no. 3 (95% maximum wind peaking at 70 seconds). For this condition the bending moment for the velocity feedback is lower than for the other systems.

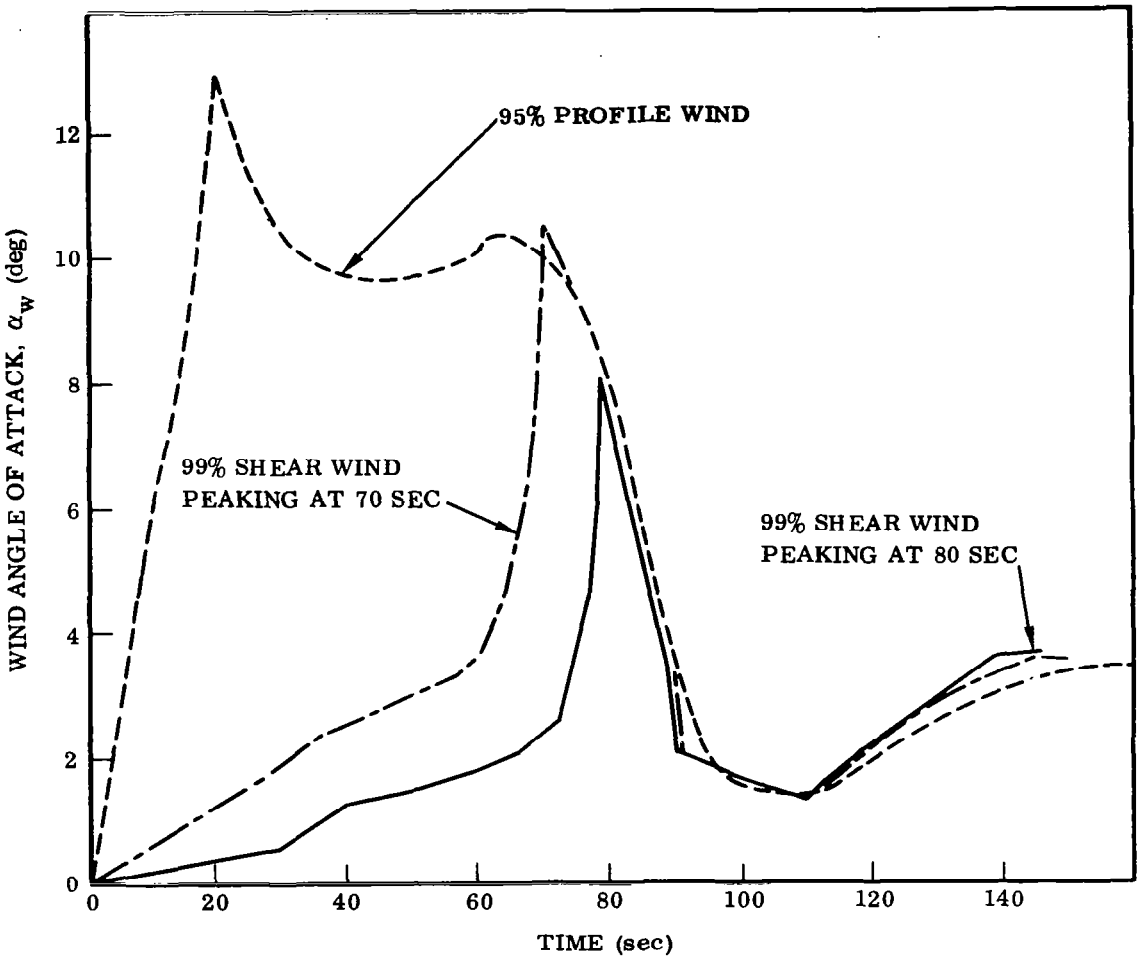

Figure 3. Wind Profiles

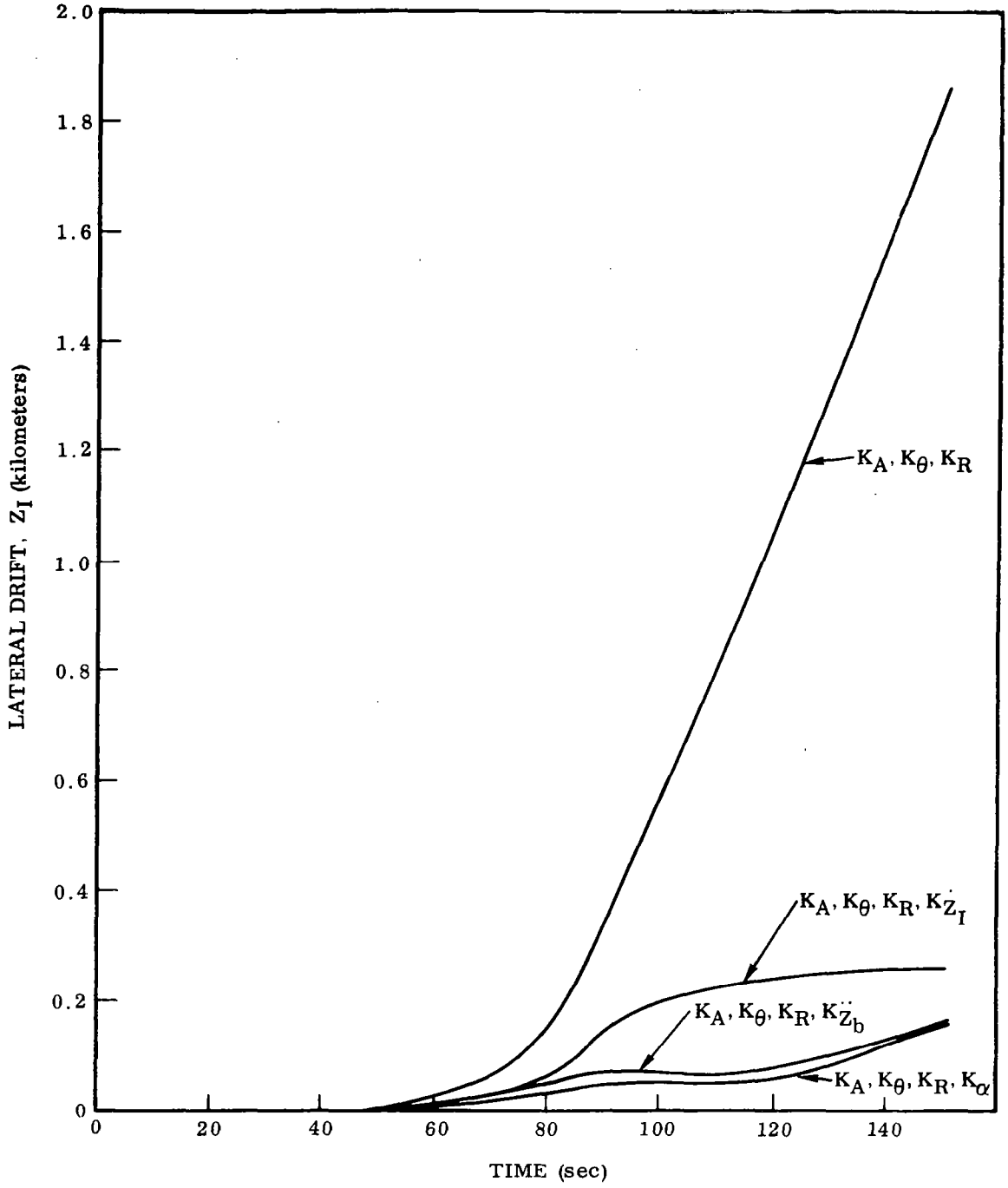

Figure 4. Drift as a Function of Flight Time for the Saturn V Launch Vehicle — Wind No. 1: 99% Shear Peaking at 80 Sec

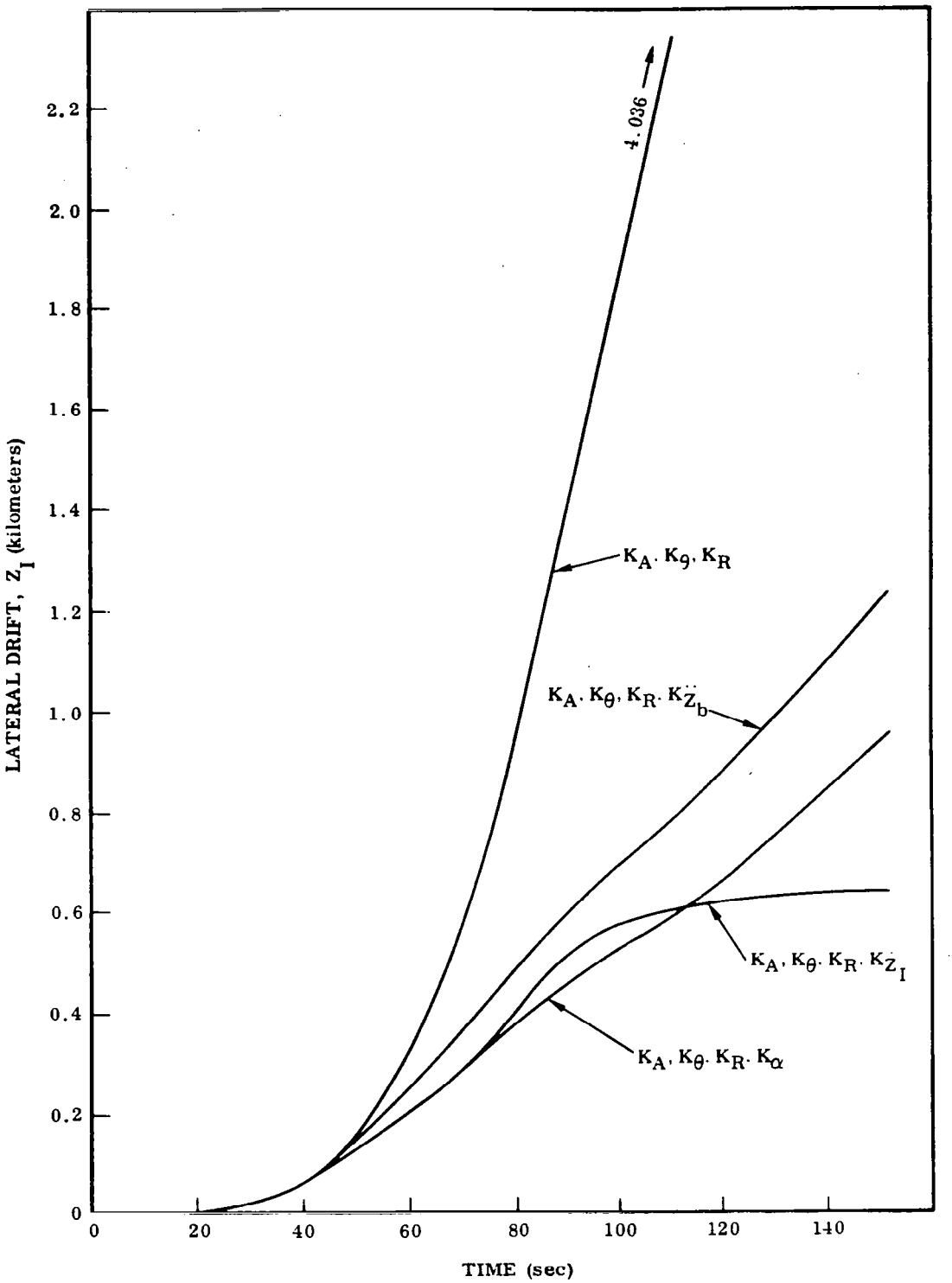

Figure 5. Drift as a Function of Time for the Saturn V Launch Vehicle — Wind No. 2: 95% Profile

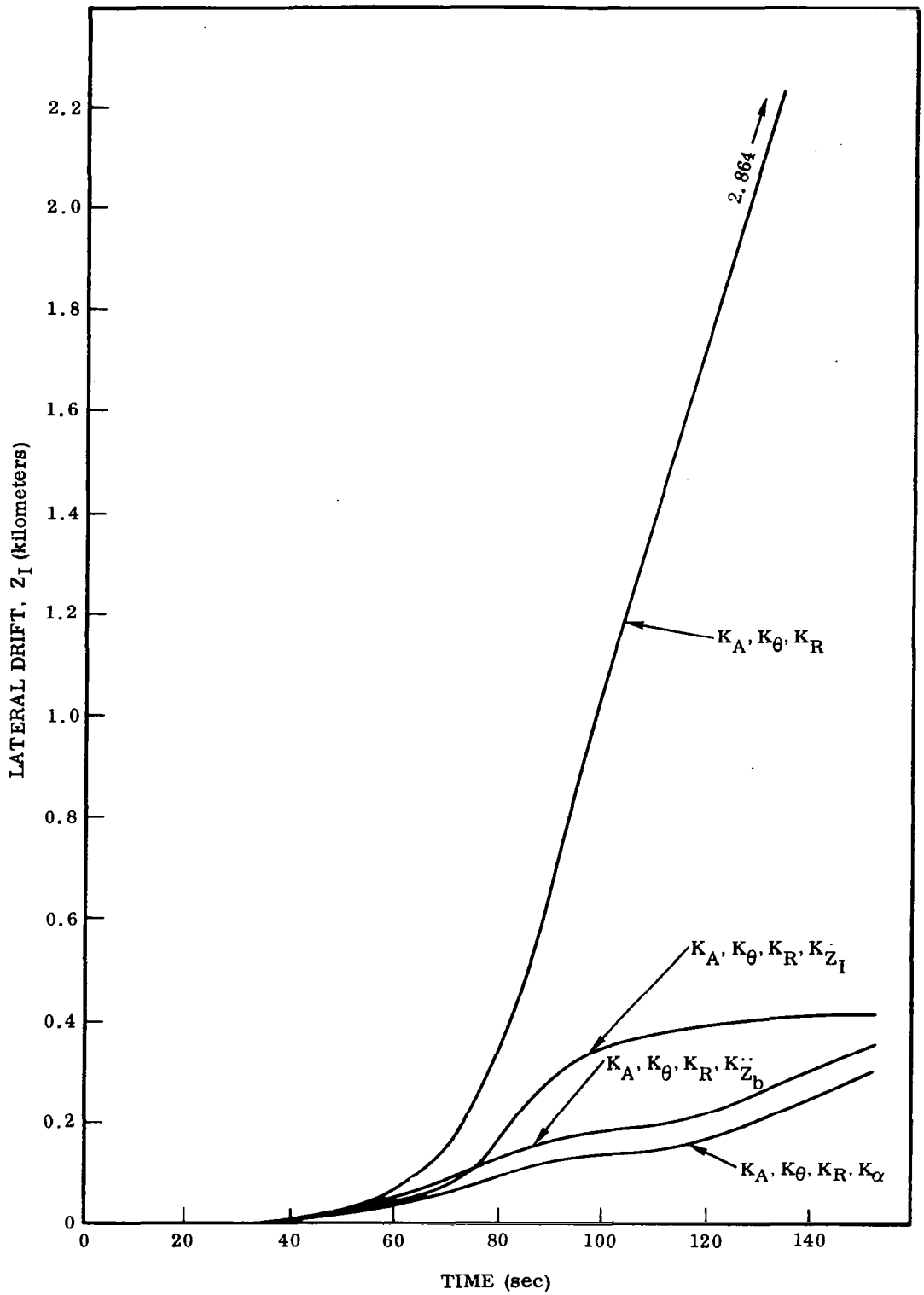

Figure 6. Drift as a Function of Flight Time for the Saturn V Launch Vehicle — Wind No. 3: 99% Shear Peaking at 70 Sec

Table 5. Maximum Bending Moment

CONTROL LAW						WIND	α (deg)	β (deg)	STATION (M)	BENDING MOMENT (in.-lb × 10^8)
K_A	K_θ	K_R	$K_{\dot{Z}_I}$	$K_{\ddot{Z}_b}$	K_α					
						FLIGHT TIME = 60 SECONDS				
√	√	√				1	1.32	0.12	80	0.200
√	√	√	√			1	1.24	0.12	80	0.188
√	√	√		√		1	1.17	0.11	80	0.178
√	√	√			√	1	1.25	0.12	80	0.190
√	√	√				2	6.66	0.63	80	1.011
√	√	√	√			2	6.65	0.63	80	1.011
√	√	√		√		2	6.06	0.57	80	0.920
√	√	√			√	2	6.54	0.62	80	0.992
√	√	√				3	2.75	0.26	80	0.418
√	√	√	√			3	2.61	0.25	80	0.398
√	√	√		√		3	2.44	0.23	80	0.371
√	√	√			√	3	2.59	0.24	80	0.393
						FLIGHT TIME = 70 SECONDS				
√	√	√				1	1.80	0.38	74	0.365
√	√	√	√			1	1.71	0.37	74	0.347
√	√	√		√		1	1.56	0.34	74	0.318
√	√	√			√	1	1.67	0.37	74	0.342
√	√	√				2	6.42	1.37	74	1.301
√	√	√	√			2	6.71	1.42	74	1.353
√	√	√		√		2	6.04	1.30	74	1.229
√	√	√			√	2	6.58	1.44	74	1.338
√	√	√				3	9.55	1.82	74	1.839
√	√	√	√			3	8.96	1.76	74	1.750
√	√	√		√		3	7.97	2.13	82	1.817
√	√	√			√	3	8.25	2.24	82	1.900
						FLIGHT TIME = 80 SECONDS				
√	√	√				1	7.55	1.82	78	1.760
√	√	√	√			1	6.97	1.75	78	1.528
√	√	√		√		1	5.99	1.95	79	1.641
√	√	√			√	1	5.99	1.95	79	1.639
√	√	√				2	4.23	1.13	78	1.040
√	√	√	√			2	4.67	1.23	78	1.141
√	√	√		√		2	4.58	1.22	78	1.126
√	√	√			√	2	4.79	1.30	78	1.176
√	√	√				3	5.99	1.55	78	1.422
√	√	√	√			3	4.80	1.27	78	1.172
√	√	√		√		3	5.10	1.36	78	1.251
√	√	√			√	3	5.14	1.37	78	1.263

These studies indicate that path velocity meter feedback can be used to reduce drift caused by winds. For the winds with high shears and embedded jets, the velocity feedback systems have lower bending moments than the drift minimum systems using angle-of-attack or accelerometer feedback.

As has been demonstrated above, a series of steps should be followed to determine the control law required and the preliminary gain value. These steps are as follows:

a. Select a control equation or equations based on criteria and constraint.

b. Determine a set of rigid body equations (see Section 2) and equations relating sensor output to vehicle dynamics.

c. Perform final value analysis to develop a feel for the selected control law or laws. It is helpful to compare results to the attitude control law.

d. Perform steady-state analysis as shown in Section 2.

e. Determine preliminary gains. The characteristic equation Eq. (6) can be represented by

$$s^3 + (2\zeta_n \omega_n + \omega_d) s^2 + (2\zeta_n \omega_n \omega_d + \omega_n^2) s + \omega_d \omega_n^2 = 0$$

Selection of vehicle parameters at applicable flight times and desired values of ζ_n, ω_n and ω_d allow solution for system gains or gain ratios.

f. Selected gains and vehicle parameters can then be applied to steps c. and d.

g. A time slice or time-varying simulation to determine vehicle response to design winds should be utilized. In addition, preliminary loads calculations can be performed.

Items c., d., e. and f. can be omitted, and cut-and-try simulation work can be substituted. However, it is the author's experience that the time spent on Items c., d., e. and f. provide the best foundation for the load-relief autopilot analyst. This is especially true for the specialist from a field other than stability and control.

3.4 STABILITY ANALYSIS

A discussion in detail of stability analysis techniques applicable to load-relief autopilots would be redundant with other monographs in this series.* However, two examples will be presented to demonstrate the effect of additional feedback loops on vehicle

*cf. Vol III, Part 1, Attitude Control During Launch, Vol I, Part 1, Short Period Dynamics and Vol I, part 3, Elastic Body Equations.

stability and attendant problems facing the analyst. These examples will cover both open-loop and closed-loop stability techniques.

The first example is an open-loop study presented in unedited form in Ref. 7. Using predesign analysis results as a design guide, the higher order dynamics and coupling terms were included in steady-state response studies. For these studies, a coupled rigid body structural mode digital program is used.

Each of the control laws studied exhibits different response characteristics, and in order to specify each critical stability margin region, the attitude control law is accepted as the standard for the accepted stability margins.

The control laws investigated are

$$\delta = -K_A(K_\theta\theta + K_{R1}\dot{\theta}_1 + K_{R2}\dot{\theta}_2)$$

$$= -K_A(K_\theta\theta + K_{R1}\dot{\theta}_1 + K_{R2}\dot{\theta}_2 + K_{\ddot{Z}_b}\ddot{Z}_{b_a})$$

$$= -K_A\left(K_\theta\theta + K_{R1}\dot{\theta}_1 + K_{R2}\dot{\theta}_2 + K_{\ddot{Z}_b}\ddot{Z}_{b_a} + \frac{K_V}{\tau_V s + 1}\ddot{Z}_{b_a}\right)$$

These control laws and the total system are illustrated on Fig. 7.

The Nichols diagrams for the analysis at maximum dynamic pressure are shown on Fig. 8; Fig. 8a establishes the aerodynamic gain margin for the attitude/attitude rate control law as +11 db, the rigid body phase margin as +30 deg, and the rigid body gain margin as -6.5 db. When this basic control law is modified with acceleration and/or filtered acceleration feedback, these rigid body margins are affected. For addition of acceleration feedback to the original attitude feedback (solid curve, Fig. 8b), it is seen that the aerodynamic gain margin is slightly increased and the rigid body phase margin is improved due to the additional lead obtained from the accelerometer angular term, but the rigid body gain margin is degraded. This results from the coupling between the rigid body mode and the first structural mode. The first structural mode has less amplitude with the accelerometer than with the attitude feedback only due to the summation of vectors at the first mode frequency. This is not in general the conclusion reached and is not true in this instance for the higher frequency bending modes. Observe from these response plots that insight into the values for $K_A K_{\ddot{Z}_b}$ and $K_A K_\theta$ required to obtain aerodynamic load reduction, which has been discussed, would be lacking if the structural dynamics were not included in the airframe model at this stage. Further analysis of the two response plots having acceleration feedback (solid curve, Fig. 8c) demonstrates the significance of including the filtered term, $\left(\frac{K_A K_V \tau_V}{\tau_V s + 1}\right)$, in the control law. The only apparent difference from a short period stability point of view is the slight reduction of the aerodynamic gain margin. The

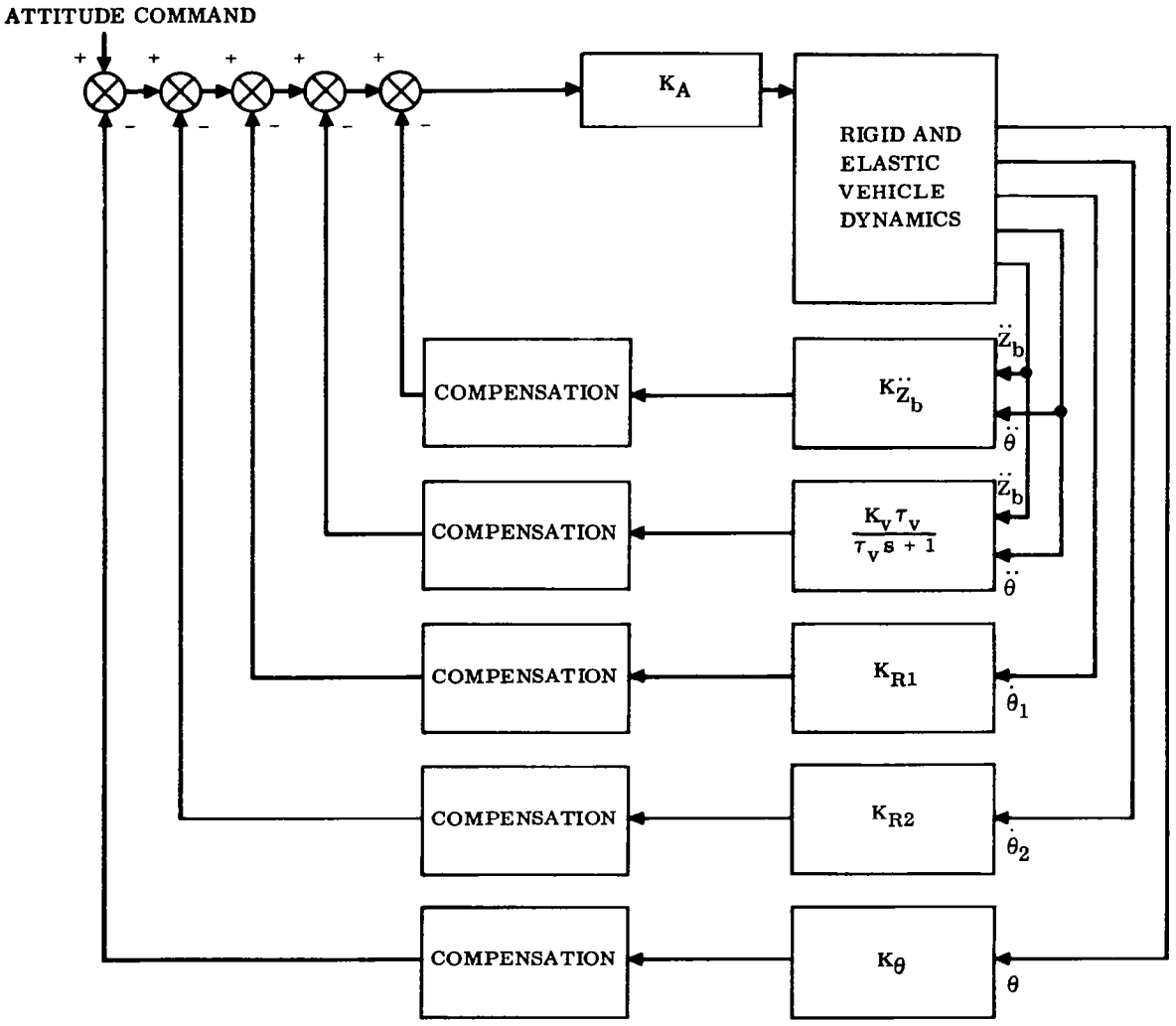

Figure 7. Planar System Diagram

$K_A K_\theta = 1.0$

$K_A K_{R_1} = 0.38$ SEC

$K_A K_{R_2} = 0.42$ SEC

COMPENSATION

$$\frac{1}{(TS+1)^2} = \frac{1}{\left(\frac{S}{15}+1\right)^2}$$

RIGID BODY FREQUENCY = 2.4 RAD/SEC
RIGID BODY DAMPING RATIO = 0.66

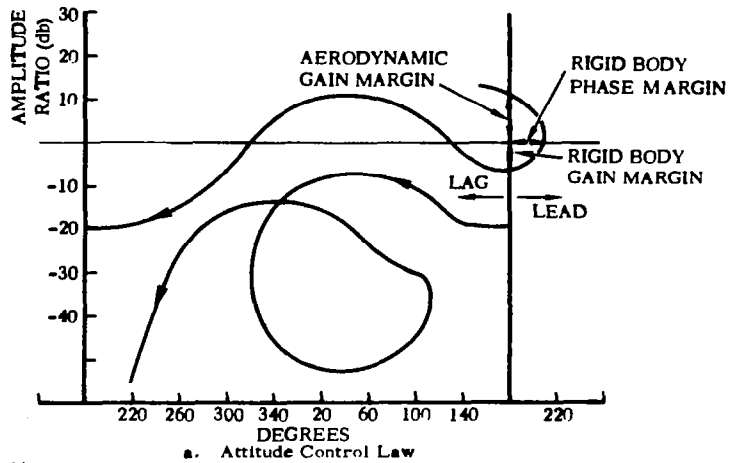

a. Attitude Control Law

$K_A K_\theta = 1.0$

$K_A K_{R_1} = 0.38$ SEC

$K_A K_{R_2} = 0.42$ SEC

COMPENSATION

ATTITUDE ACCELERATION

$$\frac{1}{\left(\frac{S}{15}+1\right)^2} \quad \frac{1}{\left(\frac{S}{10}+1\right)^2\left(\frac{S}{3}+1\right)}$$

RIGID BODY FREQUENCY = 1.82 RAD/SEC
RIGID BODY DAMPING RATIO = 0.48

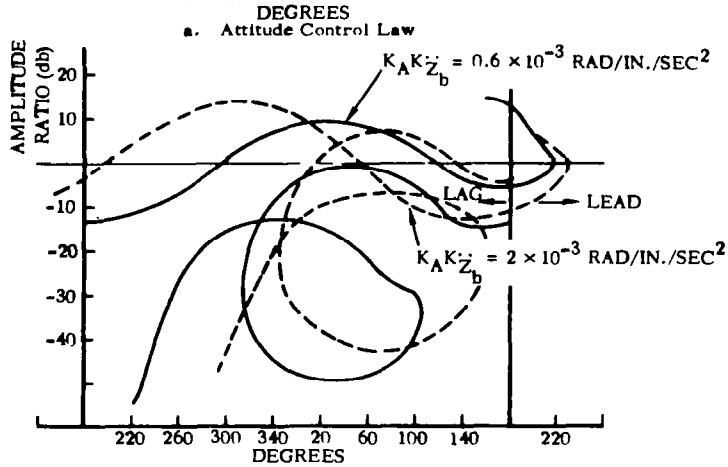

b. Attitude + Acceleration Control Law

$K_A K_\theta = 1.0$ $K_A K_V = 3.75 \times 10^{-3}$ RAD/IN./SEC

$K_A K_{R_1} = 0.38$ SEC

$K_A K_{R_2} = 0.42$ SEC

COMPENSATION

ATTITUDE LAGGED ACCELERATION

$$\frac{1}{\left(\frac{S}{15}+1\right)^2} \quad \frac{7.5K_V K_A}{7.5S+1} \quad \frac{1}{\left(\frac{S}{10}+1\right)^2\left(\frac{S}{3}+1\right)}$$

ACCELERATION

$$\frac{1}{\left(\frac{S}{10}+1\right)^2\left(\frac{S}{3}+1\right)}$$

RIGID BODY FREQUENCY = 2.2 RAD/SEC
RIGID BODY DAMPING RATIO = 0.51

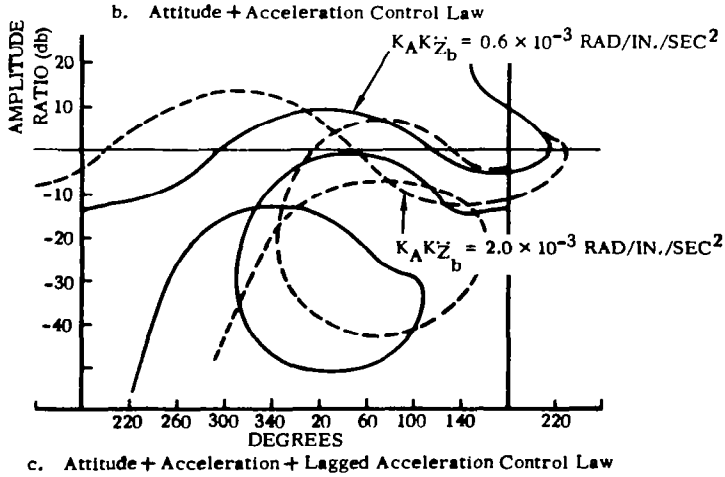

c. Attitude + Acceleration + Lagged Acceleration Control Law

Figure 8. Open Loop Frequency Response at Max q

remainder of the frequency spectrum is not altered by this term. Subsequent studies indicate that while from a structural stability point of view, little change is effected by the addition of this lagged acceleration feedback, a significant reduction in aerodynamic loads may be obtained.

The stability of the rigid and elastic modes is acceptable for the basic attitude control law and, with the additional acceleration control law, the margins are not adversely affected. The aerodynamic margin is altered slightly between the three control laws, the rigid body phase margin is improved with the addition of the accelerometer, and the rigid body gain margin is reduced but is within acceptable limits. The second and third structural modes are increased somewhat. The control law gains used for these (solid curve) stability plots are

$$K_A K_{\ddot{Z}_b} = 0.6 \text{ rad/in./sec}^2 \times 10^{-3}$$

$$K_A K_V \tau = 0.5 \text{ rad/in./sec} \times 10^{-3}$$

$$K_A K_\theta = 1.0 \text{ rad/rad}$$

$$K_A (K_{R_1} + K_{R_2}) = 0.8 \text{ rad/rad/sec}$$

The corresponding compensation dynamics are shown on the respective open loop response plots (Fig. 8). This set of parameters will result in a system that is approaching a minimum drift system, but drifting downwind. Calculations on a steady-state basis predicted that a $K_A K_{\ddot{Z}_b}$ of 1.9×10^{-3} and $K_A K_\theta = 1.0$ at the max q condition would result in a minimum drift system. In order to reduce aerodynamic loads lower than those obtainable with this minimum drift configuration, the method would be to reduce $K_A K_\theta$ and increase $K_A K_{\ddot{Z}_b}$. However, referring to the open-loop response plot, Fig. 8, it will be seen that the first mode has shifted in phase (dashed curve), reducing the phase margin, and its magnitude has increased. Furthermore, an attempt to rephase the first mode by reducing the corner frequency of the compensation filter will tend only to amplify all structural modes and, in the example shown, the second mode will become marginally stable. This example is completely dependent upon the elastic properties of the vehicle and therefore each case must be considered independently. The results tend to indicate the sensitivity of adjustment of control law feedback gains and compensation filters to obtain aerodynamic load reduction of an elastic vehicle.

In contrast to the open-loop stability analysis, the stability analysis in Ref. 6 was performed using root locus techniques as follows.

The synthesis of an autopilot configuration for Atlas/Centaur is strongly dependent on the root-locus technique to give a qualitative (and to a lesser extent, a quantitative) grasp of the stability situation. For the root-locus technique to be used, the system

nonlinearities, viz., the engine-positioning servo, the propellant slosh damping, and the deadzone in the auxiliary loop must somehow be linearized. In the following discussion, emphasis is placed upon those portions of the flight using the load-reduction autopilot. The autopilot block diagram is illustrated in Fig. 9. Its operation for the first 40 seconds of flight is identical to that of the standard autopilot. By 40 seconds of flight, the aerodynamic loading builds up to an appreciable value, and the auxiliary loop is activated. The differential-pressure signals are then fed through the deadzone circuit to the position-gyro torquer with a gain equal to $K_{\Delta P}K_i$ (where $K_{\Delta P}$ is the proportional gain and K_i the integral gain), and to the gyro-signal amplifier with a gain of $K_{\Delta P}$. The pitch program continues to torque the pitch-displacement gyro. The autopilot operates in this mode throughout the region of high aerodynamic loading, passing through maximum αq at about 66 seconds and maximum q at about 84 seconds. At 110 seconds of flight, the load-reduction loop is removed from the autopilot, the position gyro is removed from the system, and the guidance platform position reference signals are admitted through the limiter.

A complete stability analysis of a flexible-bodied vehicle, in which all of the interactions affecting stability are considered simultaneously, is not practical. Such an analysis would make the synthesis of an autopilot control system very difficult because the pertinent physical phenomena would be obscured. However, the various degrees of freedom of the configuration are, to a large extent, dynamically uncoupled. Thus, the stability of the rigid-body control and propellant-sloshing modes can be analyzed independently of the higher frequency elastic bending modes. This procedure considerably reduces the complexity of the problem.

The Atlas and Centaur liquid oxygen tanks employ baffles to dampen propellant sloshing. In the Atlas liquid oxygen tank, the baffling effect is present from about 105 seconds until BECO. For this reason, in the root-locus analysis to follow, propellant slosh damping due to baffles has been neglected.

The engine-positioning servo used on Atlas/Centaur vehicles is a nonlinear device which, at low frequencies, can be approximated by a single lag whose break frequency is a function of engine velocity. At low frequencies, the dominant nonlinear phenomenon is the Coulomb friction in the gimbal bearing, which produces an equivalent velocity deadzone. At high engine velocities, i.e., with high engine amplitudes and frequencies in a limit-cycle condition, the Coulomb friction has less effect in proportion to the total motion; and this results in a higher break frequency, or smaller time constant. The opposite is true at lower frequencies and amplitudes. In the root-locus analysis, various values of the actuator break frequency, K_c', are used, resulting in multiple loci. Fig. 10 shows the variation of K_c' with amplitude and frequency for the Atlas/Centaur booster actuators. With the aid of these data and the root loci shown in subsequent figures, an estimate of the limit-cycle amplitude may be obtained. The major factor to remember in this analysis is the presence of some sort of limit cycle resulting from the behavior of the engine-positioning servo.

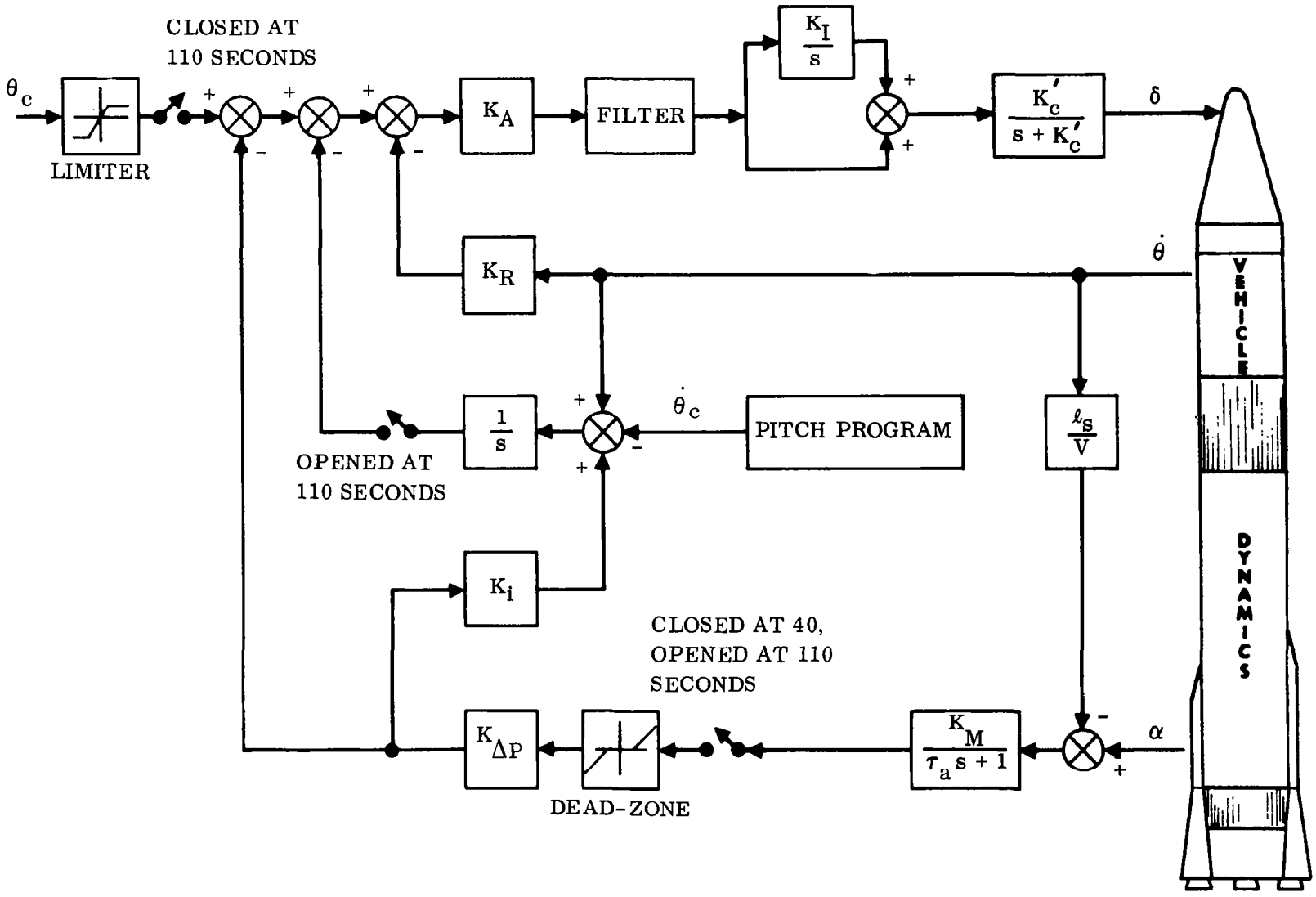

Figure 9. Load-Reduction Autopilot Block Diagram

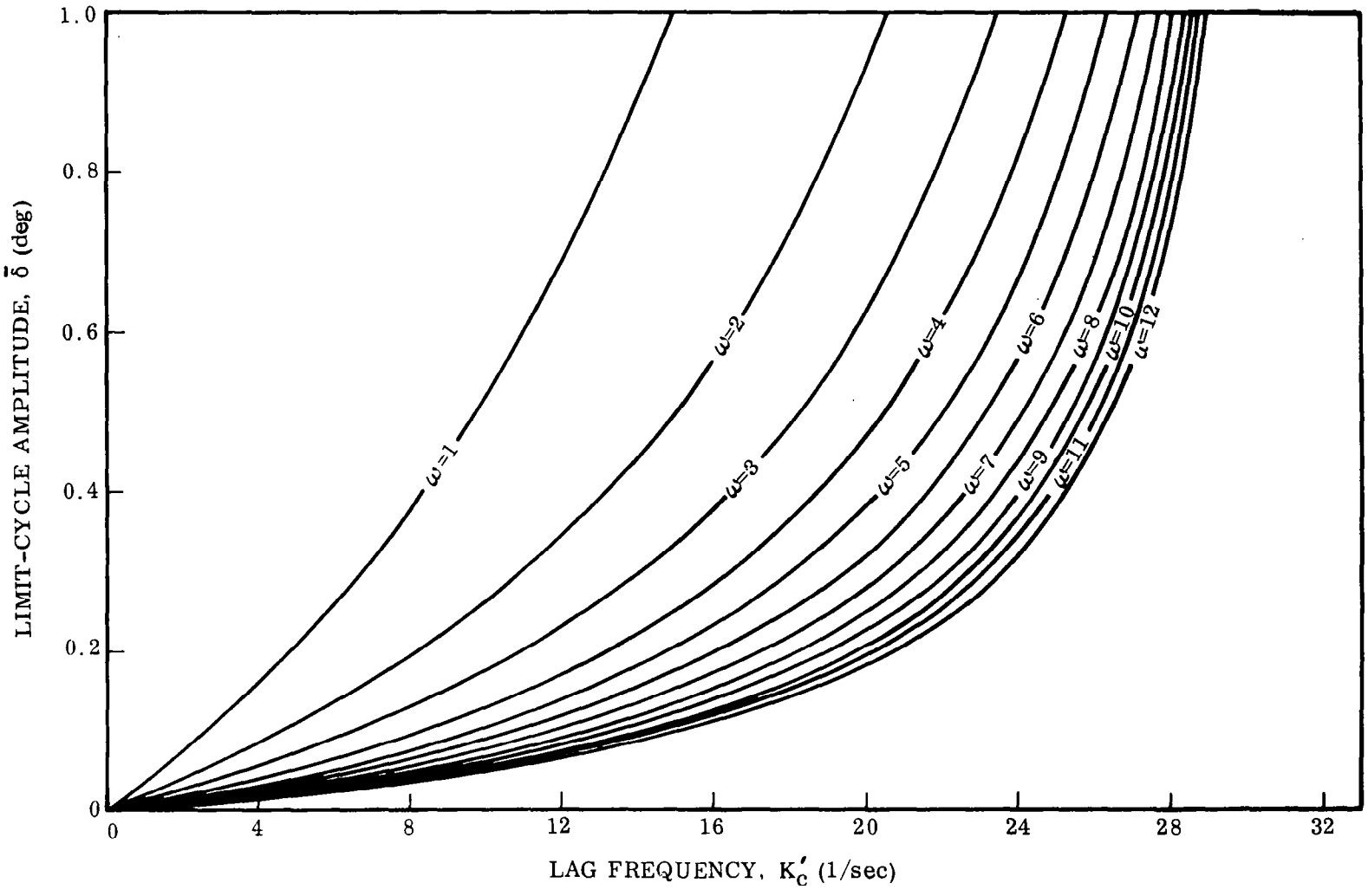

Figure 10. Low Frequency Approximation, $K_c'/(s + K_c')$, Atlas/Centaur Booster Actuator

The presence of a deadzone in the auxiliary loop requires that the autopilot be stable with no load-reduction loop even when the load-reduction loop is closed. This is essentially the situation when the signal level falls inside the deadzone of the auxiliary loop.

Fig. 11 illustrates the rigid body and sloshing loci for the vehicle with no load-reduction loop at 84 seconds. It should be noted that the aerodynamic coefficients used in these root loci are those defining the most depressed trajectory that can be flown and involving a nominal angle of attack of six degrees. The rigid body stability indicated is thus conservative. When the load-reduction loop is closed, all the loci depart from their previous root locations, as shown in Fig. 12. The poles shown on the loci are the closed-loop roots of the standard autopilot. In every instance, the loci depart in a direction to decrease the stability. In the case of the rigid body control mode, the stability properties predict a limit cycle amplitude of 0.2 degree at 84 seconds of flight. Since this occurs at a frequency of 3.0 radians per second, the resulting load due to the engine limit cycle is relatively small.

The bending stability analysis for the Atlas/Centaur vehicle also uses the root locus technique. An equivalent third-order actuator is derived from the basic actuator, engine, and servovalve parameters, using the describing function technique. The modal data are derived from consideration of the mass and stiffness distribution of the vehicle. Knowing the generalized mass, frequency, mode shapes and slopes, and the actuator describing function, it is then possible to obtain root loci for various values of the assumed engine half-amplitude, $\bar{\delta}$. The methodology employed in stabilizing the vehicle bending modes is the same as that followed in the past on Atlas space boosters, viz., to phase-stabilize the first bending mode and gain-stabilize the higher modes. The approach used is to place the gyros in a location which causes the locus to depart in an unstable direction early in the flight. An autopilot filter is then employed to lag the locus, or rotate it clockwise around the pole, until (for large engine amplitudes) it departs straight down the imaginary axis. The problem then is to obtain the required lag at launch. When this is done, the locus continues to rotate in a clockwise direction as flight time progresses. It thus continually improves the stability situation. In order to obtain the required departure angle, the rate gyro must be located ahead of the first mode antinode at SN 600. With this gyro configuration, the autopilot-stabilization filter must provide 90 degrees of phase lag at the first-mode frequency in order to stabilize the mode at launch. From this time onward the stability situation improves.

Unfortunately, the large phase-lag requirements for first-mode frequency deteriorates sloshing stability at lower frequencies. A quadratic lag provides the simplest solution to the problem of achieving a minimum phase lag at lower frequencies for a given lag at higher frequencies. The damping ratio of the filter is chosen so that peaking of the response through the autopilot can be minimized at and below the filter resonant frequency. The quadratic lag used (frequency, $\omega_f = 12.5$ rad/sec; damping ratio, $\zeta_f = 0.5$) has a resonant frequency lower than necessary for the vehicle, resulting

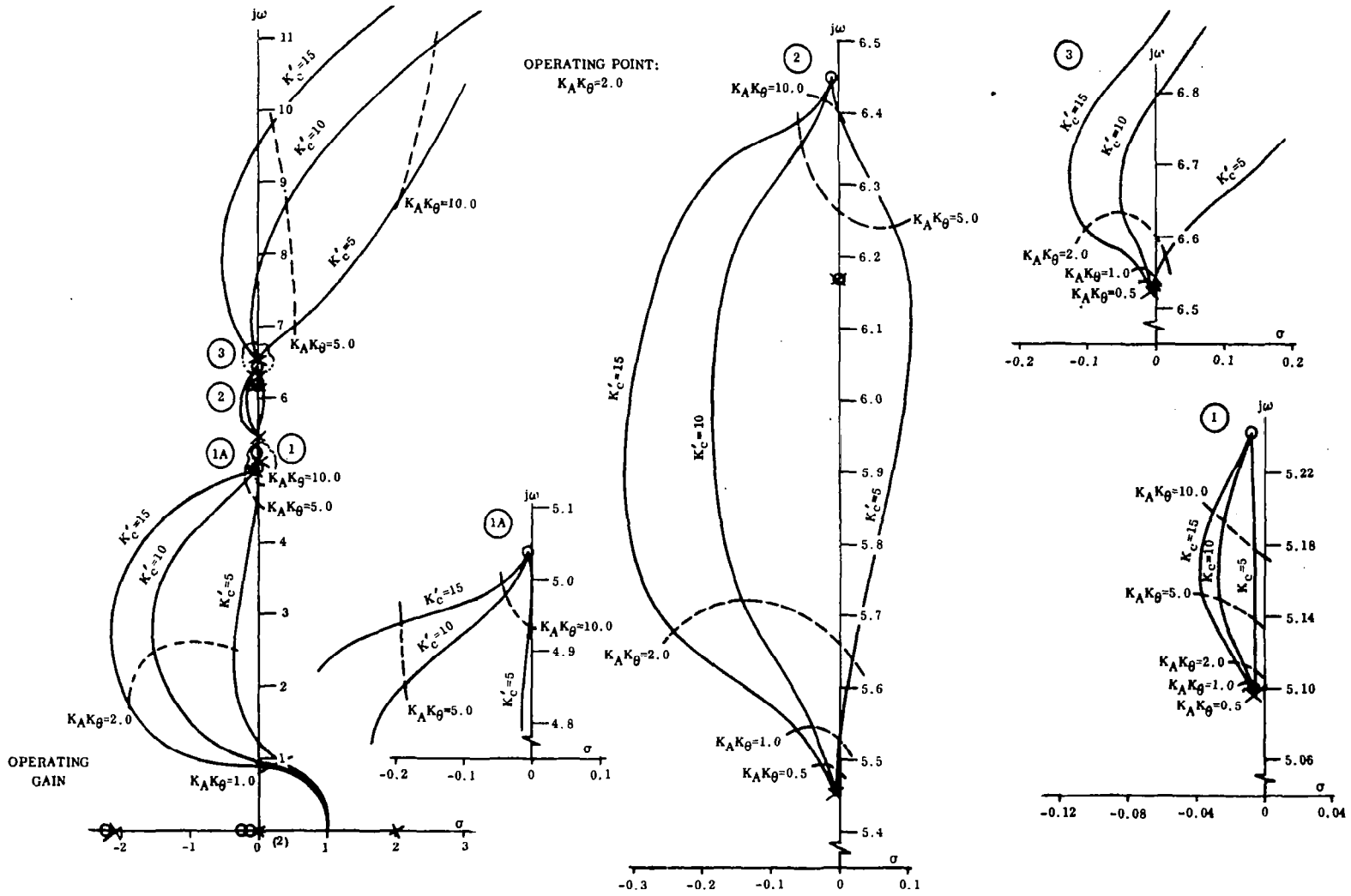

Figure 11. Rigid-Body/Propellant Sloshing Stability at 84 Seconds (Maximum q, After Filter Change, No Load-Reduction Loop)

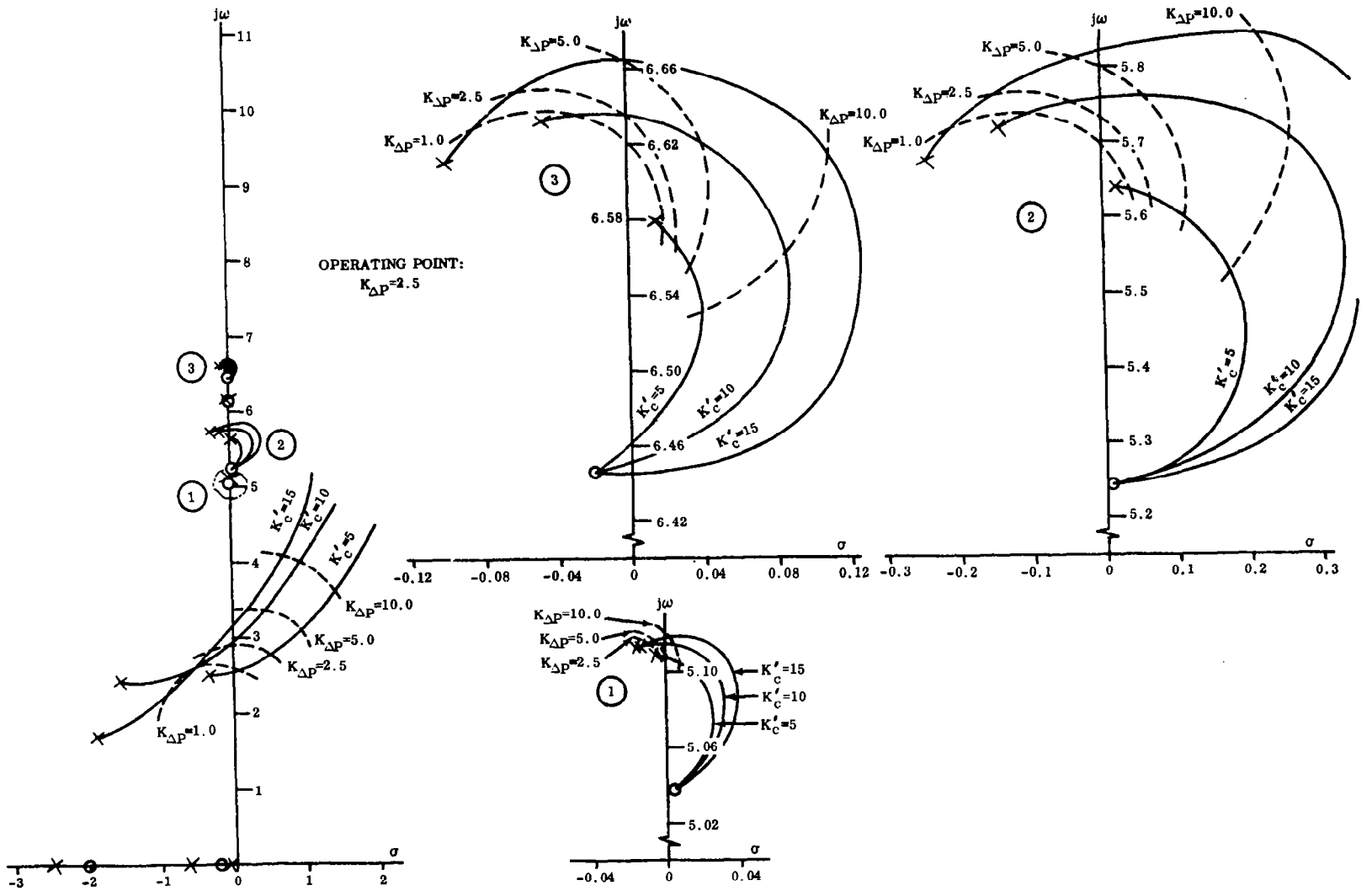

Figure 12. Rigid-Body/Propellant Sloshing Stability at 84 Seconds (Maximum q, After Filter Change, Load-Reduction Loop Closed)

in a larger phase margin than necessary at launch. After about 70 seconds of flight the filter is switched to a higher resonant frequency in order to improve the sloshing stability. The frequency is raised as much as possible to reduce the lag at lower frequencies while still maintaining stability of the first bending mode.

Fig. 13 illustrates the bending root loci for the first mode at 84 seconds without a load-reduction loop. The heavily lagged filter gain stabilizes the higher bending modes with a large amount of gain margin. The addition of the auxiliary loop presents no problems as far as the bending modes are concerned. The sensitivity of the differential-pressure sensors to the parasitic modes is very slight. This fact is indicated by the extremely small change in root location with variations in the auxiliary-loop gain. Fig. 14 illustrates the bending root loci for the auxiliary-loop gain variation. The poles in these loci are the closed-loop roots of the system with the auxiliary loop open.

The results of this analysis show that the load-reduction loop decreases stability at rigid body control frequencies and, to a lesser degree, at higher frequencies as well. It is possible to predict the existence of a small limit cycle during that region of flight when the dynamic pressure is at its maximum. At rigid body frequencies with the maximum allowable gains, the limit cycle will reach a maximum amplitude of ±0.2 degree engine deflection. Final confirmation of the figures shown here for the maximum gains depends upon the results of multidegree-of-freedom analog computer simulation, which gives a more accurate picture of the stability at rigid body and sloshing frequencies.

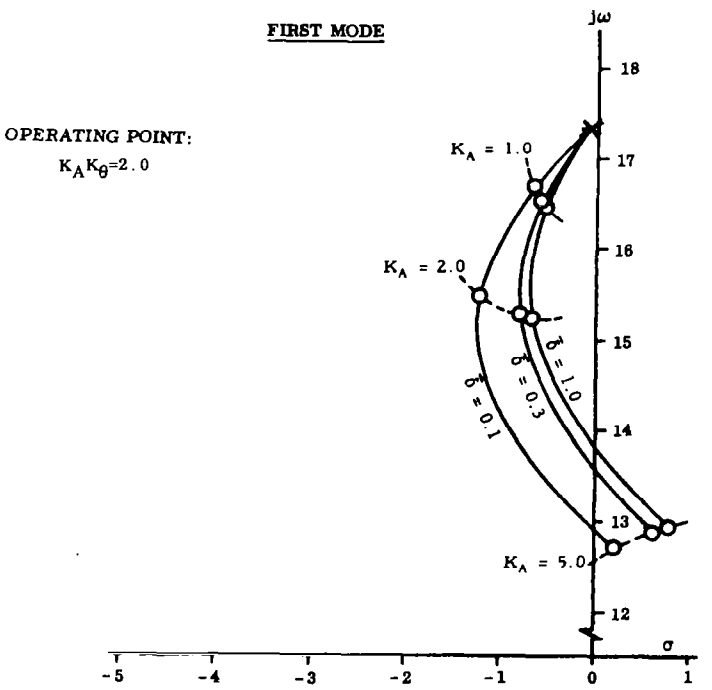

Figure 13. First Elastic-Mode Stability at 80 Seconds (No Load-Reduction Loop)

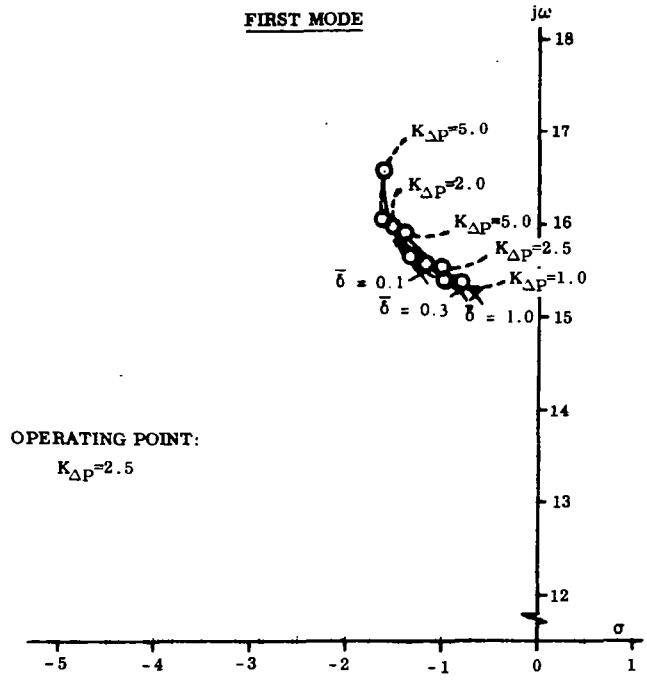

Figure 14. First Elastic Mode Stability at 80 Seconds (Load-Reduction Loop Closed)

These two examples of stability techniques illustrate approaches which can be selected for the stability analysis. Detailed explanations of both open- and closed-loop analysis techniques can be found in Ref. 13.

3.5 DETAILED CONSTRAINT AND CRITERIA ANALYSIS

It has been shown that the reduction of aerodynamic loads is possible by careful selection of an appropriate control law. However, preliminary load studies always have to be supplemented by more refined analysis, which, under certain circumstances, can lead to drastic re-evaluation or even rejection of control laws which had proven to be satisfactory under simplified assumptions. In addition, all other constraints have to be evaluated at this phase to ensure acceptable autopilot performance. This is usually the most difficult phase of the analysis. It pulls together the many technical disciplines involved in the load-relief autopilot analysis to perform the detailed analyses required for assurance that the design is acceptable for flight. This analysis falls into the bailiwick of the systems oriented analyst for coordination of a group of personnel from the required technical disciplines.

Refs. 5 and 6 summarize one such study. Ref. 6 presents vehicle loads, engine deflections, and launch availability; stability analysis; payload capability change and thermodynamic effects due to load-reduction-induced dispersions; and recommendations. Ref. 5 presents additional launch availability and trajectory dispersion analyses. Because of the classified status of Ref. 6, only Ref. 5 will be summarized here.

Although preliminary design work may be accomplished with planar studies, realistic vehicle response requires a three-dimensional trajectory analysis. An analog simulation was used to provide a continuous solution of the stability and trajectory equations in six rigid body degrees of freedom. The complete analog simulation can be broken into three major sets of equations: trajectory, vehicle, and autopilot — with wind data input from a digital computer which also stores data for bending moment calculations.

The trajectory equations, referenced to a rotating spherical earth, describe the path of the launch vehicle. Gravitational acceleration, velocity of sound, and atmospheric density are represented as functions of the vehicle altitude, an output parameter of the simulation. In addition to altitude, trajectory calculations include flight path angle, downrange position, crossrange position, and other parameters necessary for a complete trajectory description of the Atlas launch vehicle flight to sustainer engine cutoff.

The equations describing the launch vehicle motion are based on the fact that the liquid propellants comprise a major portion of the vehicle's mass during powered flight. A mechanical analogy is used to duplicate the forces and moments of the liquid propellant sloshing, consisting of a pendulum series plus a rigid mass. The rigid mass is constrained to move with the container (thus simulating the portion of fluid that does not participate in the sloshing motion) while a series of pendulums (one for each fluid mode) of specific length and mass are pivoted so that the sloshing forces and moments are duplicated. Only the first propellant mode for each of the four tanks is included in both the pitch and yaw planes, as the higher propellant sloshing modes produce negligible contributions. The anti-slosh baffles in the Atlas and Centaur liquid oxygen tanks and the shear membrane in the Atlas fuel tank introduce damping to the fluid modes and therefore have been included. This baffle damping is a function of both propellant height above a baffle and slosh amplitude. In addition to propellant sloshing forces acting on the rigid body vehicle, aerodynamic forces are present and create an inherently unstable vehicle.

Control of the vehicle is provided by pitch, yaw, and roll autopilot circuitry which duplicate autopilot gain and filter specifications throughout Atlas launch vehicle flight. Prior to 110 seconds, signals produced by vehicle motion (e.g., from rate gyros, position gyros, a differential pressure sensor, and the pitch programmer) combine to provide the autopilot error signal. Following 110 seconds a simplified guidance platform and computer simulation replaces the simulated position gyro. The differential pressure sensor is also switched out at this time. The autopilot outputs are fed into simulated nonlinear electro-hydraulic actuators which convert the signal into engine deflections. The nonlinearities reflect the effects of oil compressibility, orifice flows, and viscous and Coulomb friction and are closely approximated in the simulation. The autopilots, both conventional and load-relief, are shown on Fig. 15.

Determination of bending moments during vehicle flight with and without the load-relief autopilot is necessary, as structural launch availability is based upon the allowable

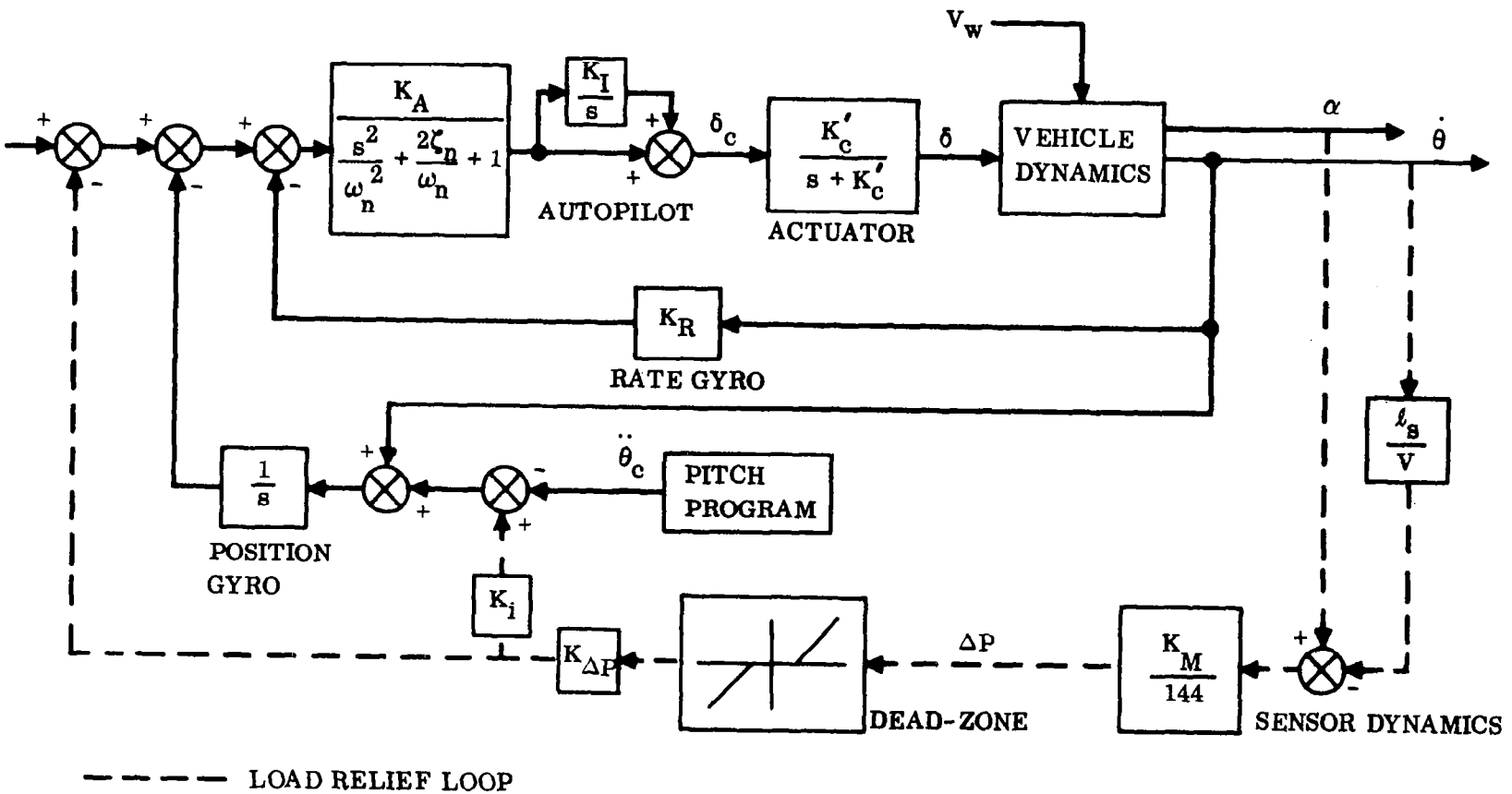

Figure 15. Autopilot Block Diagram, Load-Relief Loop

bending moments as shown on Fig. 16. Launch availability is defined as the percentage ratio of flights which do not exceed the allowable bending moments at any station and time to the total number of flights sampled. In this study, the launch availability was based on a sample of approximately 200 flights for both the standard and load-reduction autopilot using actual wind soundings.

The calculated bending moment includes the bending moment due to axial loading, gusts, and wind response. Since the structure is designed as a beam column, the axial load due to vehicle acceleration decreases the bending capability and is accounted for by converting it to an equivalent bending moment. The vehicle acceleration increases throughout booster phase as propellants are depleted, and, therefore, the equivalent bending moment increases.

To determine bending moment due to gusts, a gust was assumed to envelop the entire length of the vehicle instantaneously and to act in both the pitch and yaw planes perpendicular to the vehicle axis. The gust loading takes into account rigid body and aeroelastic response. Data for several time-slice analyses are input to a digital program to calculate bending moments with a (1 - cos kt) shape gust. By varying k, the maximum vehicle bending moment as a function of time for each station was determined.

The magnitudes of the bending moments due to wind are functions of the time history of the vehicle wind combination. It is therefore possible to predict those flight loads on the basis of a statistical wind analysis. Real wind velocity and direction profiles should be used because:

a. The velocity and shear rates of a synthetic series of flight wind profiles produce erroneous bending moments.

b. Inertial reactions vary widely between real winds and synthetic winds.

c. The dispersions of a load-reduction autopilot can be analyzed by using the long wavelength wind profiles.

The wind velocity and direction are recorded as a function of altitude with the individual wind soundings arranged in chronological order every third day for the months of December through February over a six-year period. A sample wind profile is shown in Fig. 17.

The vehicle response is measured in terms of lateral and rotational accelerations, which contribute to the encountered bending moments. In addition, the liquid propellant sloshing and aerodynamics create bending moments which must be accounted for. The analog digital system supplies this input data to a digital computer program for bending moment calculations in both the pitch and yaw planes. The resultant bending moment at each vehicle station analyzed was taken as the root-sum-square of the pitch and yaw bending moments.

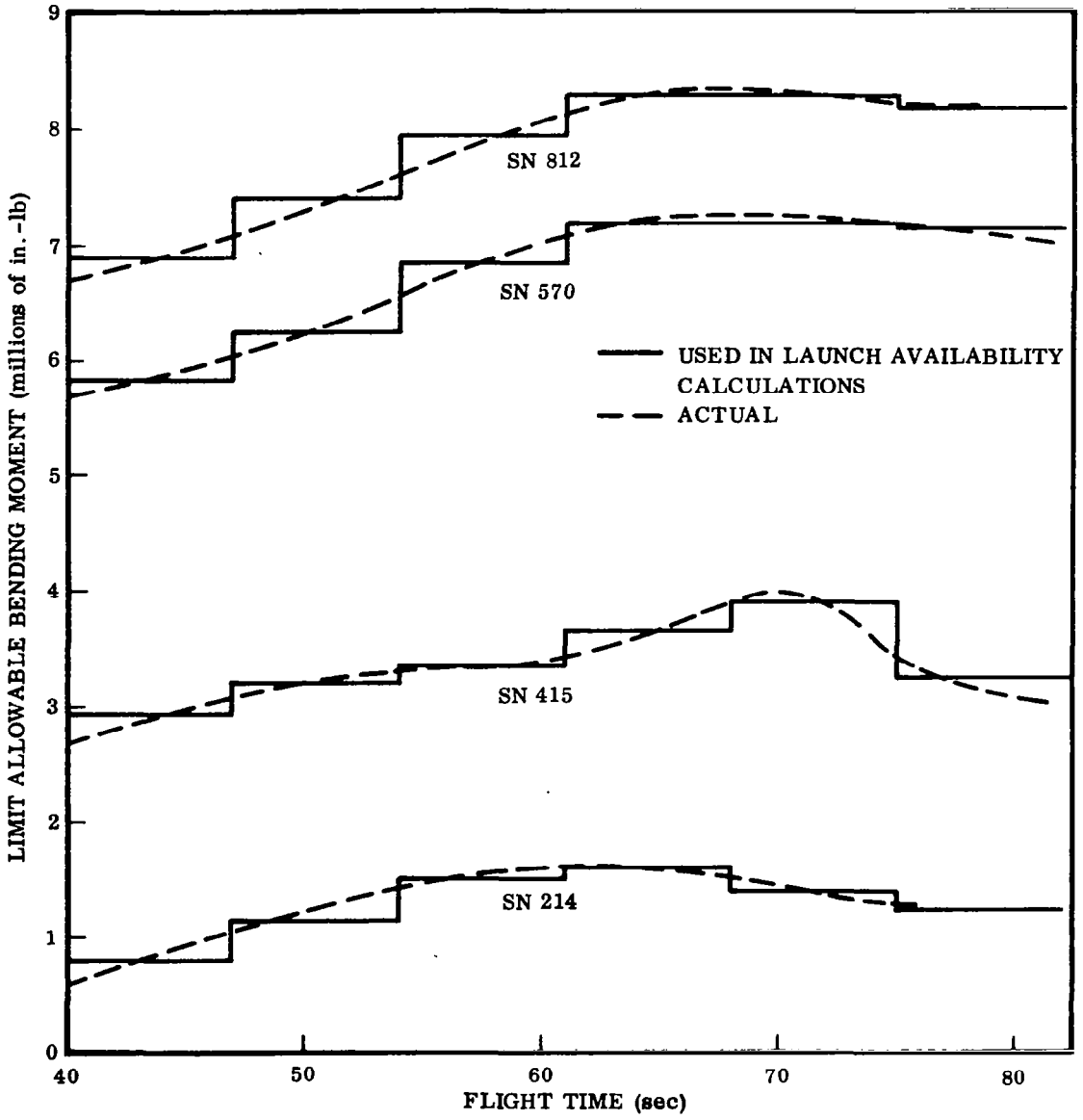

Figure 16. Limit Allowable Bending Moments

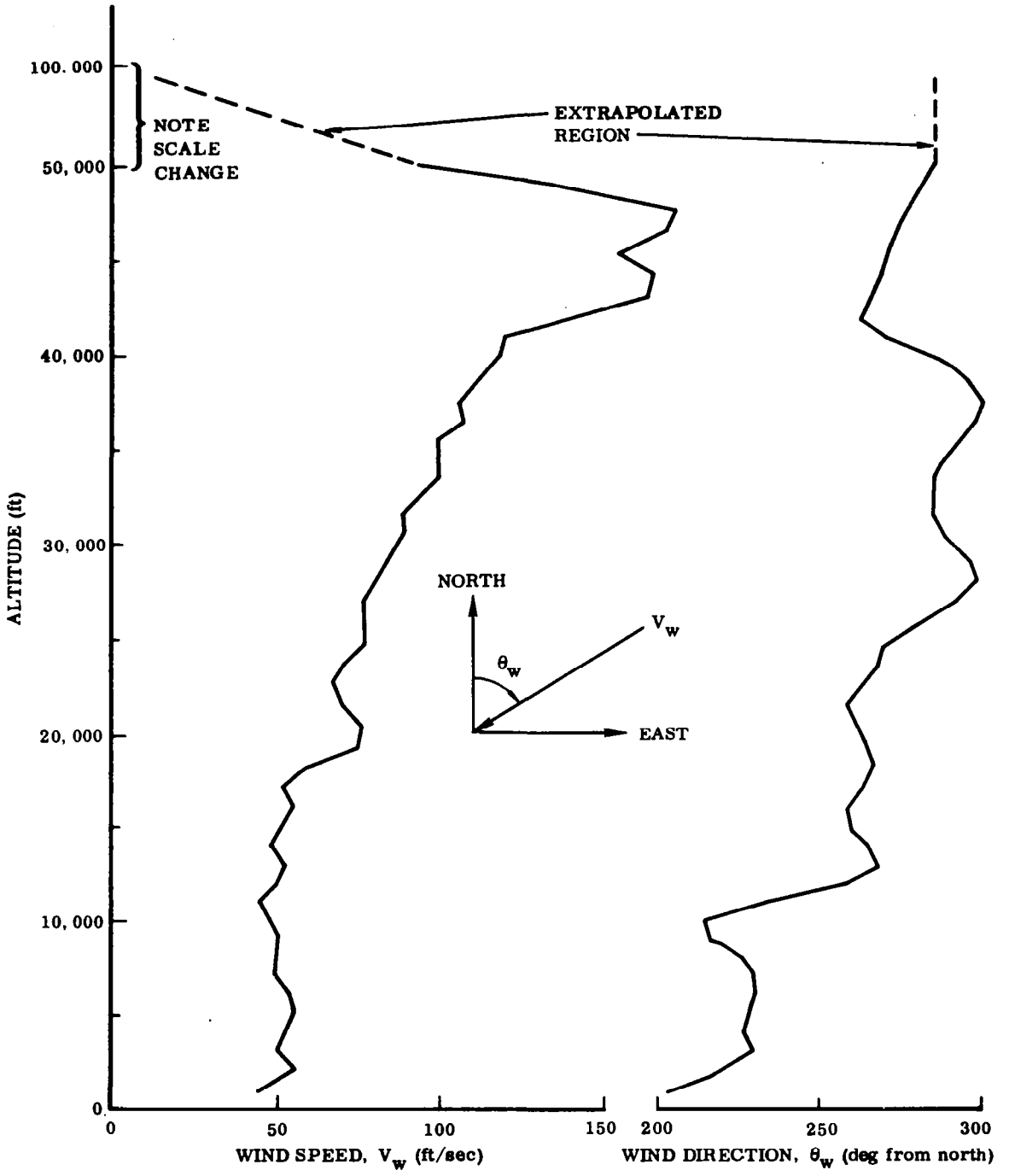

Figure 17. Avidyne Wind Profile, Montgomery, Alabama, 10 March 1955

The overall effectiveness of the load-relief autopilot in reducing loads can easily be illustrated by histograms (Fig. 18) of the maximum bending moment encountered during flight (at each station) with the standard autopilot and the load-relief autopilot. Six flights for the standard autopilot were discarded as invalid runs during the data post-processing. A large lowering of the mean value of bending moment and reduction of skewness to the right is indicated when using the load-relief autopilot. In most cases the upper limit encountered with the autopilot is about the same as the mean value encountered with the standard autopilot. The maximum bending moment encountered with the load-relief autopilot therefore is significantly less than the maximum encountered with the standard autopilot.

The launch availability was calculated by assuming that any flight that contains a calculated bending moment (at any station and time) which exceeded the limit allowable bending moment is not a successful flight. The overall launch availability using winter winds for the load-relief autopilot is 63%; for the standard autopilot it is 8.77%.

The critical stations are clearly shown on Fig. 19 which, in addition, shows launch availability "sensitivity" to an increase or decrease in limit allowable bending moments. The load-relief autopilot launch availability ranges from 19.5% at 90% of limit allowable bending moment to 79% at 110%. This means that the desirable overall launch probability of 80% could be met with an increase of structural integrity to approximately 110% of nominal at SN 812, combined with the load-relief autopilot. The standard autopilot has a launch availability of 0.0 at 90% of limit allowable bending moment and increases to only 14.5% at 110%. The critical station for either autopilot is SN 812 which has approximately the same launch availability as the overall vehicle.

Fig. 20 contains histograms of failure times for both the standard and load-relief autopilot. These plots indicate the first time of failure at each station. The plot labeled "overall vehicle" indicates first time of failure for any station for each flight. The standard autopilot overall vehicle plot in Fig. 20 indicates that the two critical times are the maximum dynamic pressure region (as expected) and also the 40- to 47-second flight time segment. For station 812 (the critical station) the critical time is the maximum dynamic pressure region. Station 214, however, is shown to be weak during the 40- to 47-second flight time regime. The effectiveness of the load-relief autopilot system is demonstrated by the reduction of failures during the maximum dynamic pressure region. The time segment from 40 to 47 seconds for stations 214 and 812 does not show this substantial decrease in failures and is therefore the critical time for the load-relief autopilot. In addition, station 214 is critical with the standard autopilot for this same time segment.

A review of the mission sequence indicates that a step in the pitch program and the activation of the load-relief autopilot occur simultaneously at 40 seconds. These events result in vehicle maneuvers that can increase angle of attack and hence can increase bending moments. For example, if the vehicle has negative angle of attack at 40 seconds, the load-relief autopilot command in the form of a step adds to the pitch program step command.

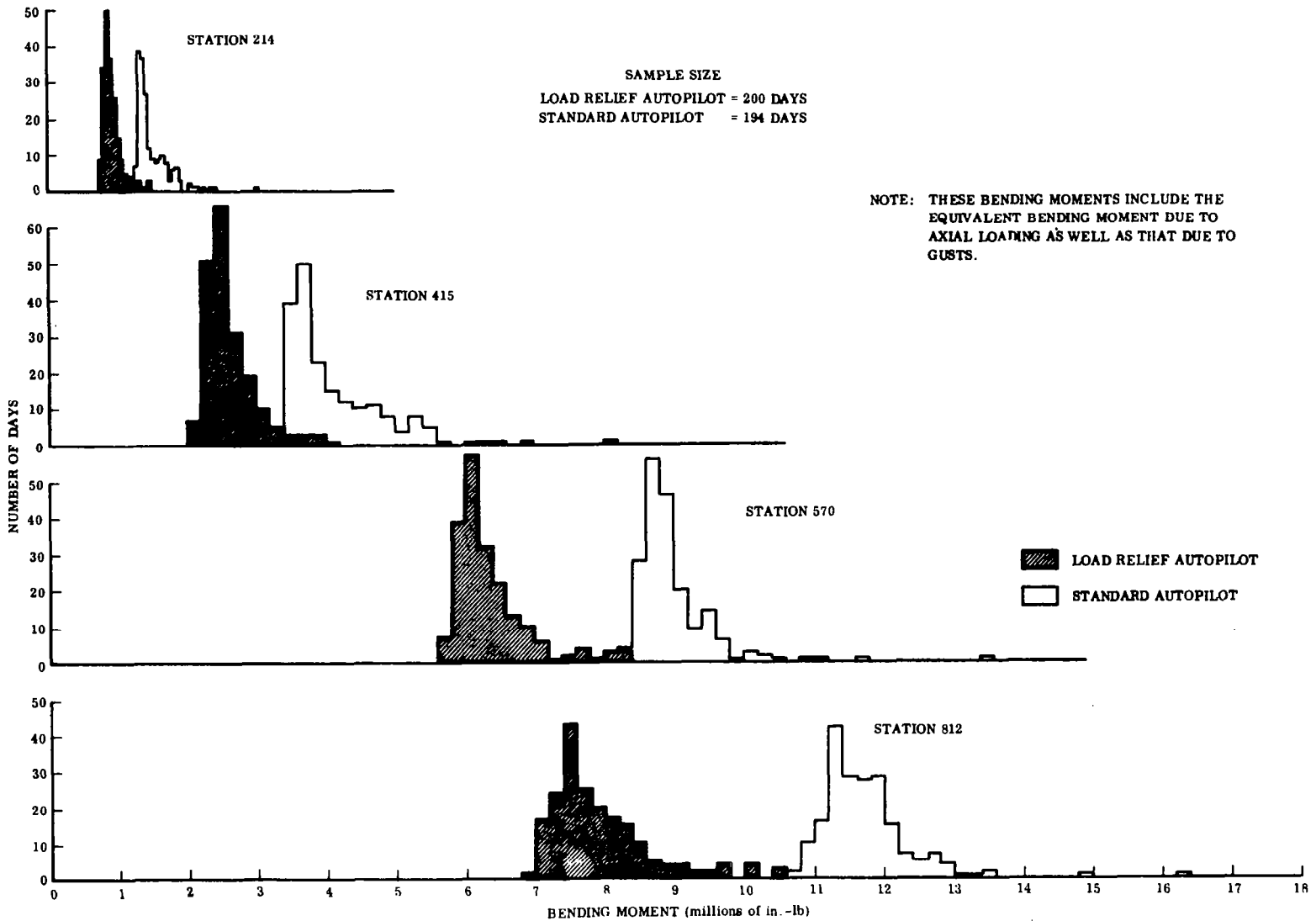

Figure 18. Maximum Bending Moment Encountered During Flight

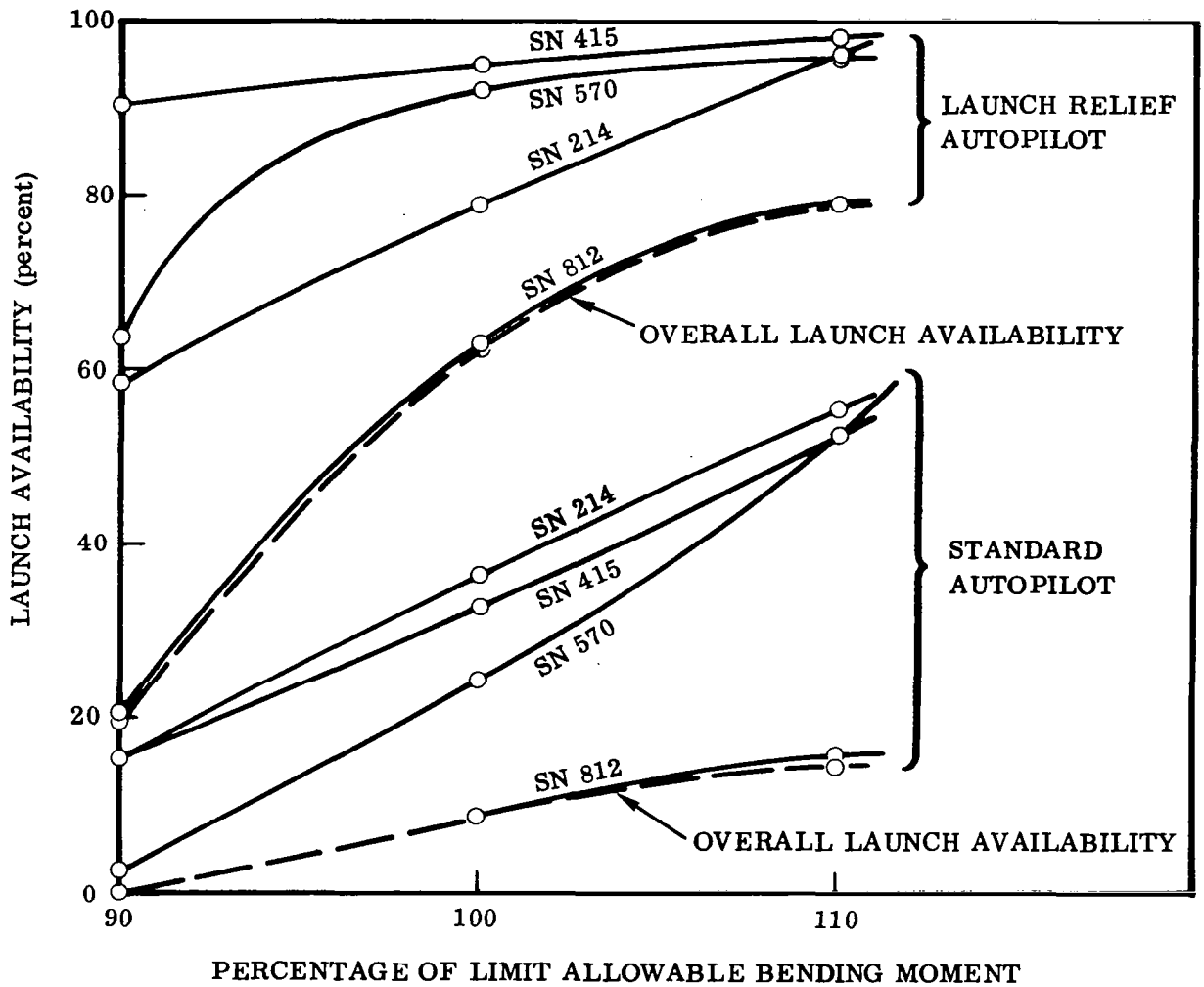

Figure 19. Launch Availability Sensitivity

Station 812, not critical at this early time for the standard autopilot, exhibits a majority of its failures for the load-relief autopilot between 40 and 47 seconds. This indicates that in addition to increases in structural strength for increased launch availability, a possible benefit would be the activation of the load-relief autopilot pressure sensor loop at a slightly earlier time in flight. An earlier initiation of the load-relief loop would reduce the vehicle transients, as they are a function of dynamic pressure times angle of attack.

Dispersions from the nominal trajectory can be seen in Fig. 21. This histogram shows altitude at 102 seconds with and without the load-relief loop. A comparison of

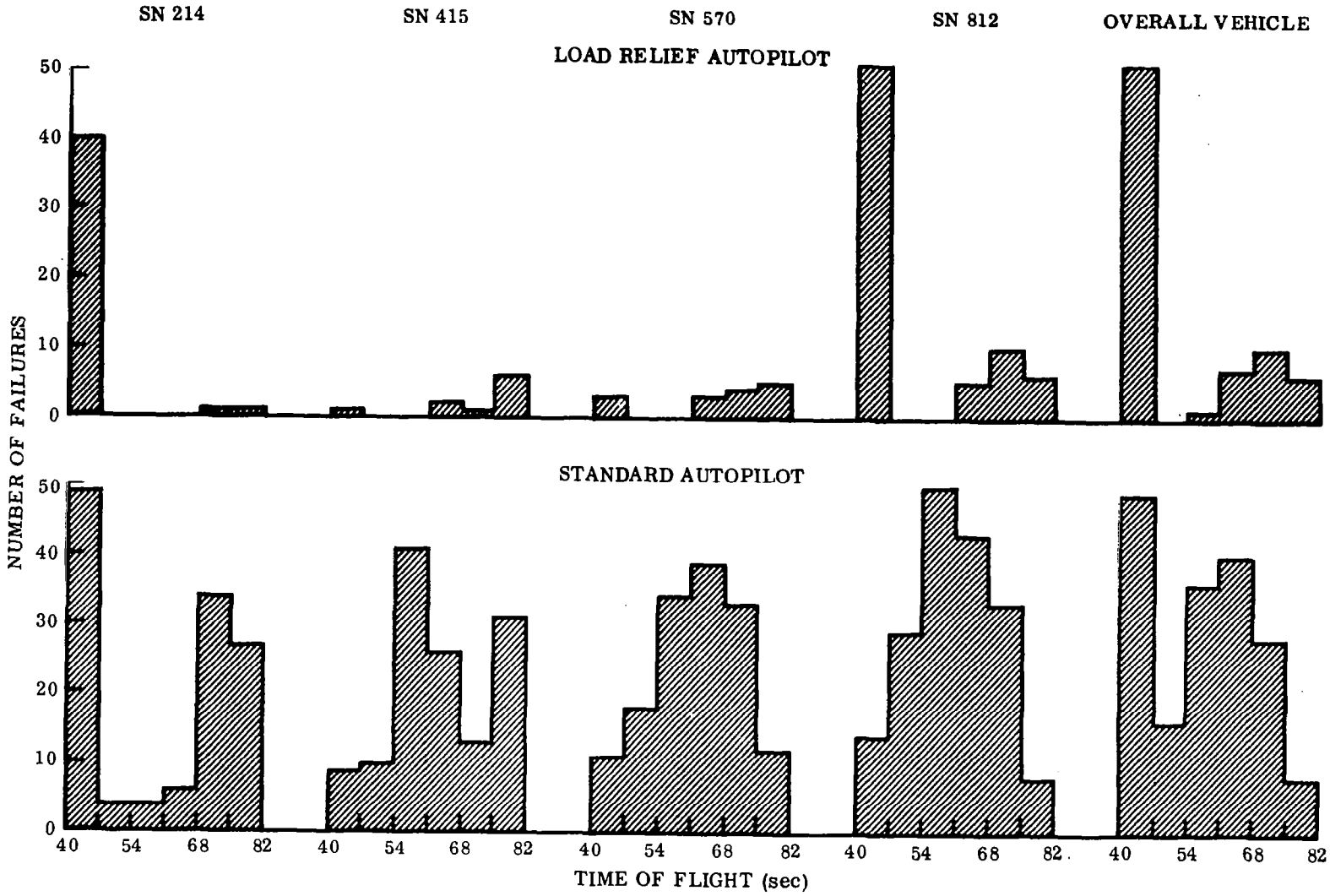

INDICATES FIRST TIME OF FAILURE DURING EACH FLIGHT

Figure 20. Failure Time Analysis

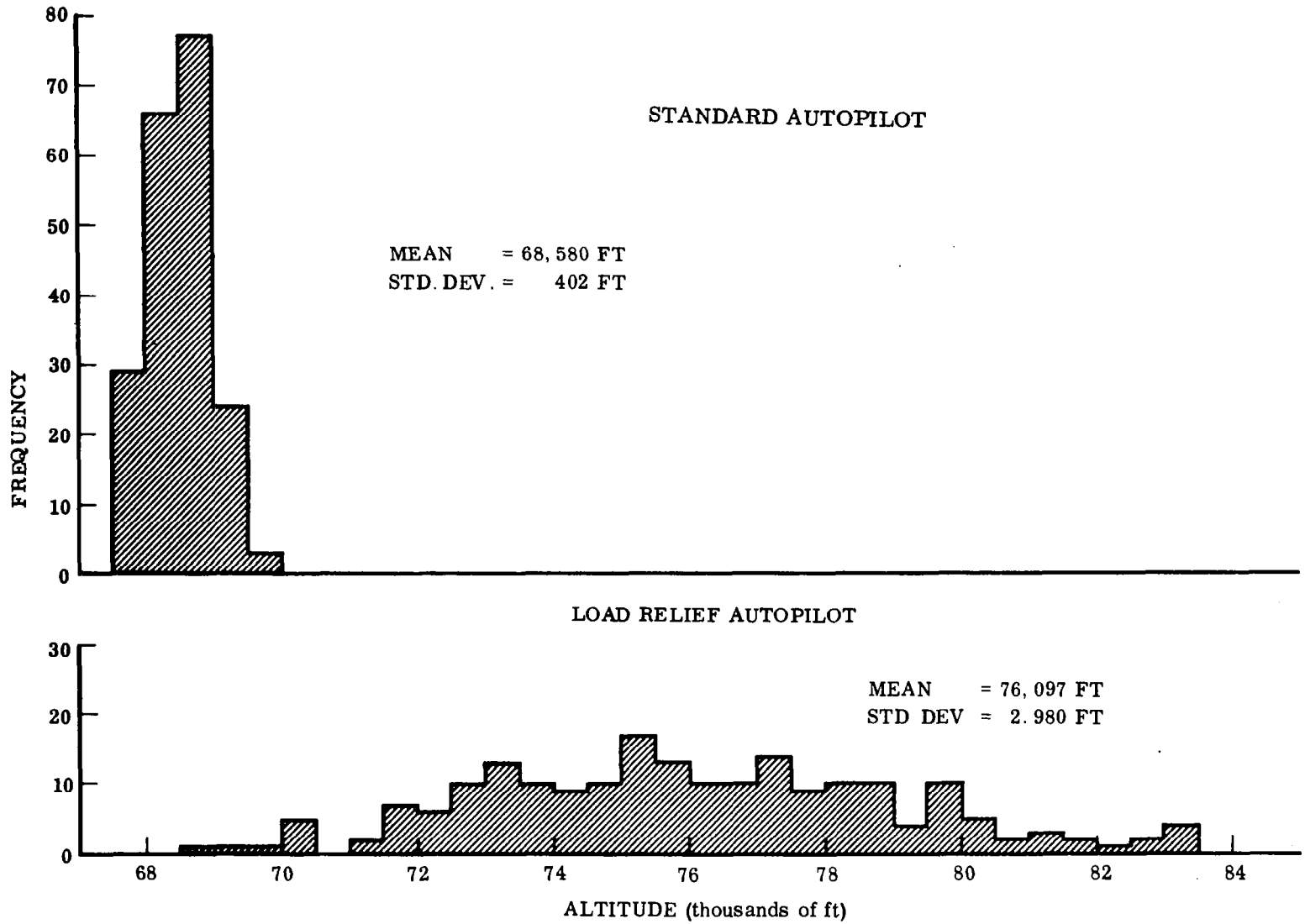

Figure 21. Altitude Dispersions, Standard and Load Relief Autopilot (T = 102 Sec)

the altitude histograms shows a much wider dispersion from the mean due to the load-relief loop. This is to be expected since the load-relief autopilot tends to follow a new zero-lift trajectory dependent upon the particular wind. Also, the load-relief autopilot distribution has a mean to the right or towards higher altitude when compared with the conventional autopilot. This trend is due to the predominance of tail winds in the set of Avidyne winter winds and also the lofted load-relief autopilot trajectory due to the slight positive angle of attack of the nominal no-wind trajectory (as provided by the pitch program).

These dispersions would be reduced starting at 110 seconds when guidance commands would revise the nominal trajectory to meet the mission requirements. Guidance equipment could handle the dispersions around the mean value, but structural and aerodynamic heating limitations would have to be observed. A pitch program for use with the load-relief autopilot could be used to shift the mean values of the trajectory parameters closer to those of the nominal conventional autopilot trajectory. Use of a pitch program tailored to the load-relief autopilot and guidance beginning at 110 seconds will allow reduction of dispersions and result in a more efficient vehicle from the performance viewpoint. A further discussion of these areas is contained in Ref. 6 but is too lengthy for inclusion here. However, the following conclusions can be made:

a. The load-relief autopilot provides adequate stability and control throughout the launch vehicle phase of the Atlas/Centaur AC-5 powered flight.

b. The load-relief autopilot provides a large reduction of the maximum encountered bending moments at all stations when compared with the standard autopilot.

c. The launch availability based on a sample of 200 Avidyne winter winds for the load-relief autopilot is 63%; and, based on a sample of 194 winter winds for the standard autopilot, is 8.77%.

d. A 10% increase in the allowable bending moment at station 812, the critical station, would raise the launch availability to 79% for the load-relief autopilot and 14.5% for the standard autopilot.

e. The critical times for the standard autopilot are the 40 to 47 second region and the maximum dynamic pressure region. The load-relief autopilot is most effective during the maximum dynamic pressure region and hence only the 40 to 47 second region remains critical.

f. The trajectory dispersions associated with the load-relief autopilot are much greater than those associated with the standard autopilot and result in a loss of performance.

g. Further studies in the area should include determination of an optimized sequence of events (pitch program, load-relief loop activation, guidance activation) with the investigation of launch availability, aerodynamic heating, and performance.

The following example of detailed analysis is concerned with induced nonlinearities in a body-mounted accelerometer feedback loop. The summary is based on the analysis and conclusions presented in Ref. 10.

An analog study indicated that a properly chosen accelerometer limit will reduce both maximum bending moment and drift. When the limit is reached a few seconds before the wind peak, the embedded jet on the wind angle is not passed through the accelerometer feedback loop, and the moment contribution from engine gimbal angle is thus reduced. This can be seen in Fig. 22 by comparing the analog results with and without a limited accelerometer. The maximum value of angle of attack is practically unaffected in either case, and hence the aerodynamic bending moment contribution is about the same. A comparison of engine gimbal angle shows that it is reduced by a factor greater than one-half at the time of the maximum wind angle of attack in the limited case due to the limiting action prior to the embedded jet. The primary reduction in bending moment is due then largely to the significant reduction in engine gimbal angle. Drift is reduced, because the large attitude angle which would normally persist unnecessarily after the wind peak is reduced by the limit. Drift rates which are unessential to the reduction of maximum bending moment are therefore inhibited.

Detailed digital simulations were run from liftoff to booster engine cutoff utilizing time-varying coefficients in order to check the bending moment reduction indicated in the analog work. An accelerometer location 34.3 meters from the engine gimbal was used since this offers the best results from a bending moment standpoint.

Since the highest moments occur at the 70 sec (max αq) time point, the 70 sec wind (Fig. 23) was used a base around which to build the load-relief gain schedule. Moments were also evaluated for the 64 sec (Mach 1), and 80 sec (max q) winds to ensure that these winds caused no moments higher than the 70 sec wind for a given schedule (see Fig. 23). Various accelerometer gains and periods of load-relief gain application were employed to determine a combination that would handle all three winds. The first objective was to reduce the moment arising from the 70 sec wind as much as possible. It was decided to linearly change the attitude gain to a value at or near zero while increasing accelerometer gain linearly to as high a value as possible while maintaining a non-oscillatory vehicle rotation into the wind during the high q portion of the digital trajectory simulation.

Through trial-and-error methods the time schedule of gain changes shown in Fig. 24 resulted. No values are shown for the various gain levels, because these are determined by the particular characteristics of the systems that were investigated. The plot merely shows the times at which gain changes are to occur. If the gain changes are started much earlier than those shown, the negative lateral velocity buildup is

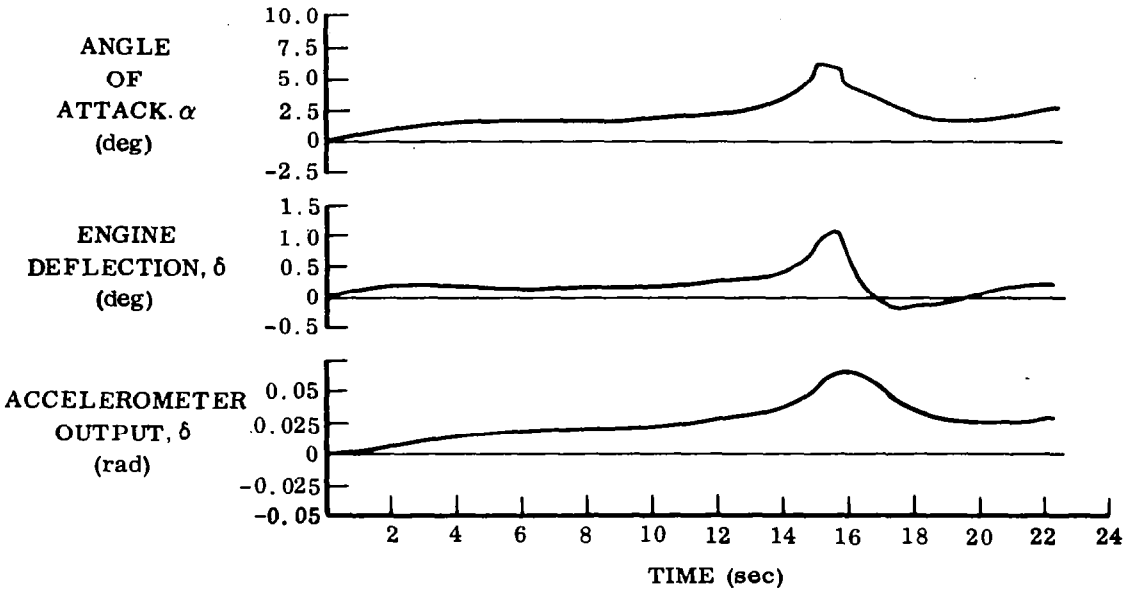

a. NO DEADBAND - NO LIMITER

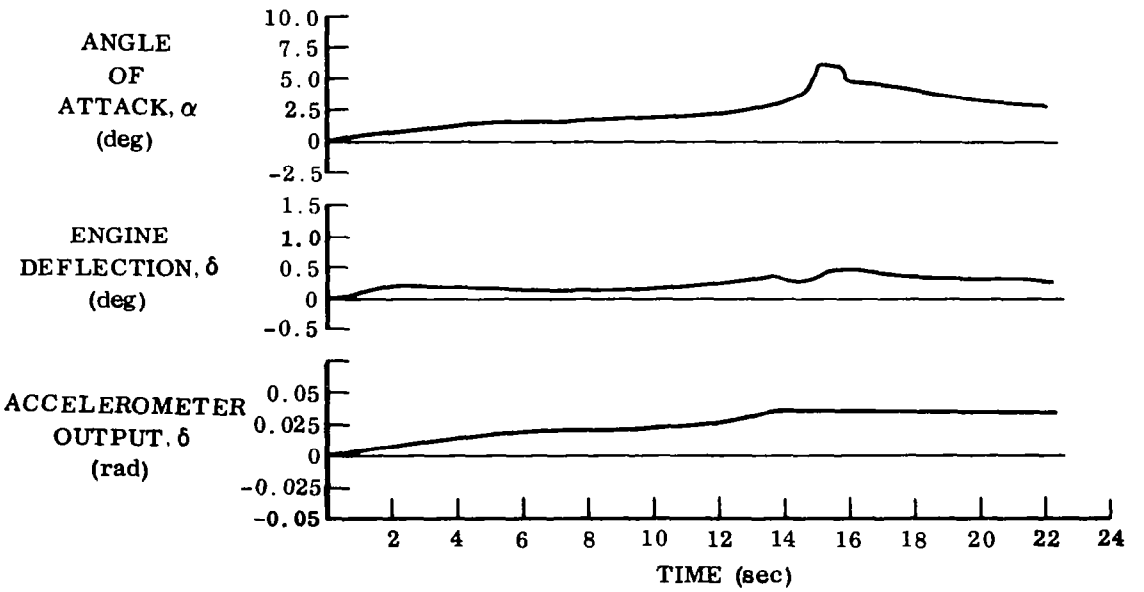

b. NO DEADBAND - 0.035 RAD. δ LIMIT ON ACCELEROMETER

Figure 22. Analog System Responses

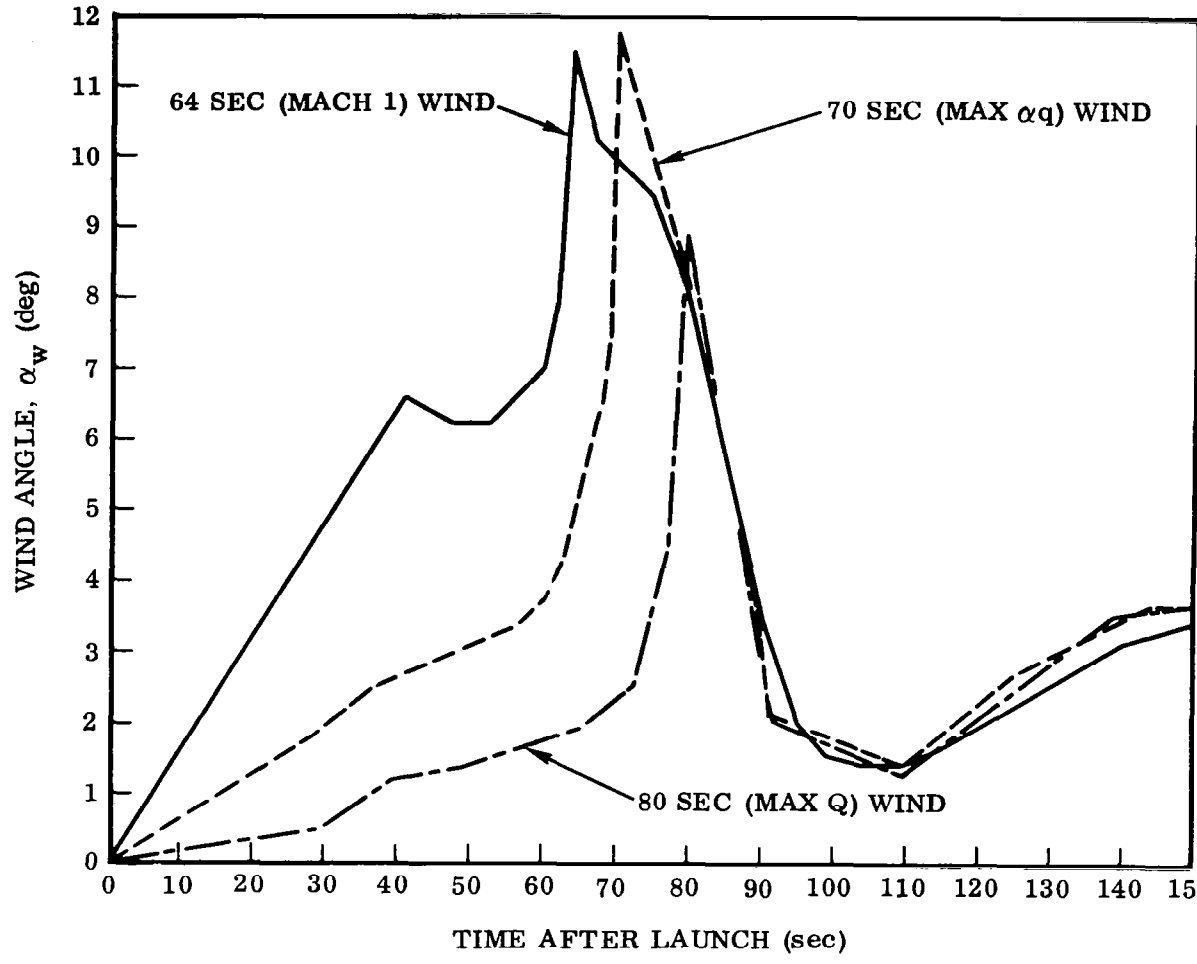

Figure 23. Wind Schedules

great enough to affect the angle of attack at 70 sec and thus the bending moment. If the change is started later, the moment for the 64 sec wind will not be reduced below that for the 70 sec wind. The schedule must also last long enough to effect a reduction in the 80 sec wind moment, while allowing a long enough period for removal of load-relief gains to avoid excessive reaction as the vehicle returns to attitude control. Another requirement is that the attitude gain be increased soon after the 70 sec wind peak in order to avoid excessive overshoot in attitude. During the rapid buildup of the 70 sec wind, $K_A K_\theta$ should be low so that the vehicle's rotation into the wind will not be inhibited. Thus, the choice of accelerometer and rate gains primarily determine the

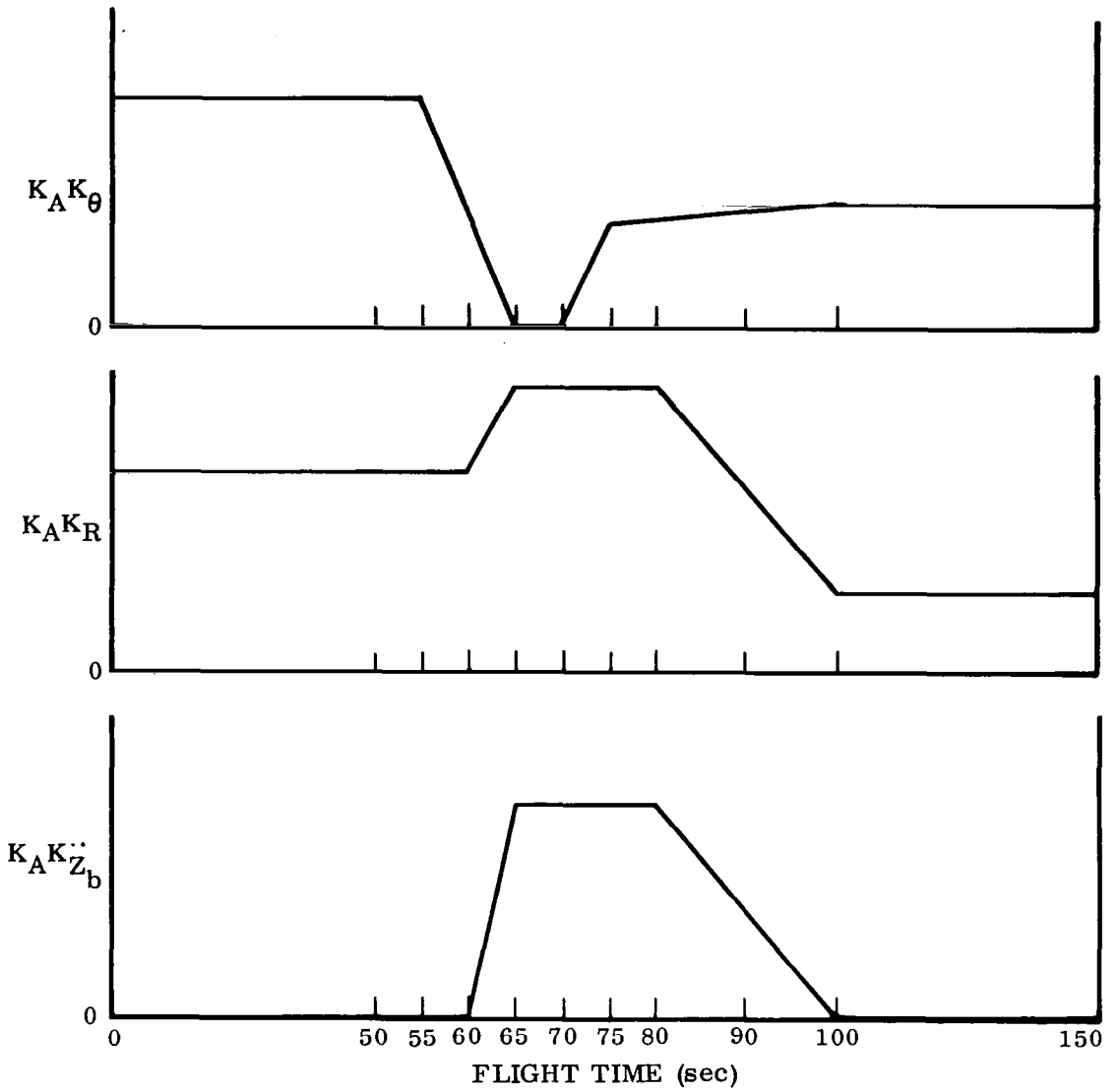

Figure 24. Basic Gain Change Schedule

systems response characteristics during this period. The times for changing gain shown in Fig. 24 were satisfactory for the three wind profiles used in this study.

The choice of gains has no effect on whatever accelerometer deadband may be included, for deadband is set up to depend only on the sensed lateral acceleration. The accelerometer gain acts only on what is passed through the accelerometer.

There is an effect on the choice of limit, however. Higher limits may be utilized with higher values of accelerometer gain, since accelerometer output will increase more rapidly. As the $K_A K_{\ddot{Z}_b}$ of the system increases, so does the optimum limit setting for maximum load reduction.

The system analyzed was a sixth-order system consisting of lags of 1 and 1.5 rad/sec on the accelerometer and a lag of 4 rad/sec on the actuator.

As a basis for comparison of all runs, an attitude control schedule with 0.15 Hz frequency and a 0.7 damping ratio for the entire flight gave a moment for the 70 sec wind of 24.10×10^7 in.-lb and a drift of 2900 meters.

Attitude gain was fixed at zero during the load-relief period while $K_A K_R$ and $K_A K_{\ddot{Z}_b}$ were varied to determine different frequencies at 70 sec for a 0.5 damping ratio. The result is a very narrow band of system frequencies (~0.1 Hz) for a reasonable range of rate gains, since the magnitudes of $K_A K_R$ and $K_A K_{\ddot{Z}_b}$ primarily affect damping. Higher frequencies require a value for attitude gain, but as attitude gain is increased, bending moment increases sharply. Several runs were made at 0.2 Hz and a 0.5 damping ratio with gains of 2.0, 3.0 and 0.104 in the attitude, rate, and accelerometer channels respectively. Maximum bending moment reached 21.12×10^7 in.-lb. Investigation of the sixth-order system was therefore restricted to frequencies around 0.1 Hz. Runs were made with zero deadband and a series of accelerometer output limits for system frequency of 0.08, 0.1, and 0.115 Hz and a 0.5 damping ratio at 70 sec. A system frequency of 0.12 Hz and 0.3 damping ratio at 70 sec was also run. These correspond to schedules A, B, C, and D (Table 6). The results are shown graphically in Fig. 25. Maximum bending moment decreases with an increase in frequency (as long as $K_\theta = 0$) since it is at these higher frequencies that $K_A K_{\ddot{Z}_b}$ is largest. Shown in the figure are the points corresponding to various limit values on the accelerometer in degrees of engine deflection for each set of gains. Again, moment reaches a minimum and then increases as the accelerometer limit is raised for each schedule of gains. The maximum moments arising from the 64 and 80 sec winds are below those shown in the plot. Terminal drift is a near-linear function of accelerometer limit. Vehicle responses for schedule B in the presence of the 70 sec wind are shown in Figs. 26 and 27.

In order to check the systems response to a small wind, a wind angle of attack of 1/3 the magnitude of the 70 sec wind (Fig. 23) was run. The resulting moment for schedule B was 5.52×10^7 in.-lb while attitude control yielded a moment of 7.46×10^7 in.-lb.

3.6 CONCLUSIONS

To provide a checklist or set of recommended procedures for the final phase of the analysis is difficult because of the large variety of possible criteria and constraints.

The selection of criteria and determination of constraints served as a guide for the analyses in Section 3.3 and 3.4. In a similar manner the detailed analysis phase is guided by the same set of criteria and constraints. Using Table 4 as a guide, analyses should be performed to satisfy questions regarding all constraints.

Table 6. Sixth-Order System

(Linear Gain Change Schedules)

TIME (sec)	SCHEDULE A			SCHEDULE B		
	$K_A K_\theta$	$K_A K_R$ (sec)	$K_A K_{\ddot{Z}_b}$ $\left(\frac{\text{rad}}{\text{m/sec}^2}\right)$	$K_A K_\theta$	$K_A K_R$ (sec)	$K_A K_{\ddot{Z}_b}$ $\left(\frac{\text{rad}}{\text{m/sec}^2}\right)$
0	0.661	1.15	0	0.661	1.15	0
55	0.661	1.15	0	0.661	1.15	0
60	0.3	1.15	0	0.3	1.15	0
65	0	1.5	0.055	0	3.0	0.130
70	0	↑	↑	0	↑	↑
75	0.4	↓	↓	0.4	↓	↓
80	0.402	1.5	0.055	0.402	3.0	0.130
100	0.409	0.70	0	0.409	0.70	0
150	0.409	0.70	0	0.409	0.70	0
	SCHEDULE C			SCHEDULE D		
0	0.661	1.15	0	0.661	1.15	0
55	0.661	1.15	0	0.661	1.15	0
60	0.3	1.15	0	0.3	1.15	0
65	0	6.0	0.28	0	3.0	0.174
70	0	↑	↑	0	↑	↑
75	0.4	↓	↓	0.4	↓	↓
80	0.402	6.0	0.28	0.402	3.0	0.174
100	0.409	0.70	0	0.409	0.70	0
150	0.409	0.70	0	0.409	0.70	0

(Attitude Control Comparison Case)

TIME (sec)	$K_A K_\theta$	$K_A K_R$ (sec)	$K_A K_{\ddot{Z}_b}$ $\left(\frac{\text{rad}}{\text{m/sec}}\right)$
0	0.661	1.15	0.0
70	0.9066	1.213	0.0
120	0.409	0.70	0.0
150	0.409	0.70	0.0

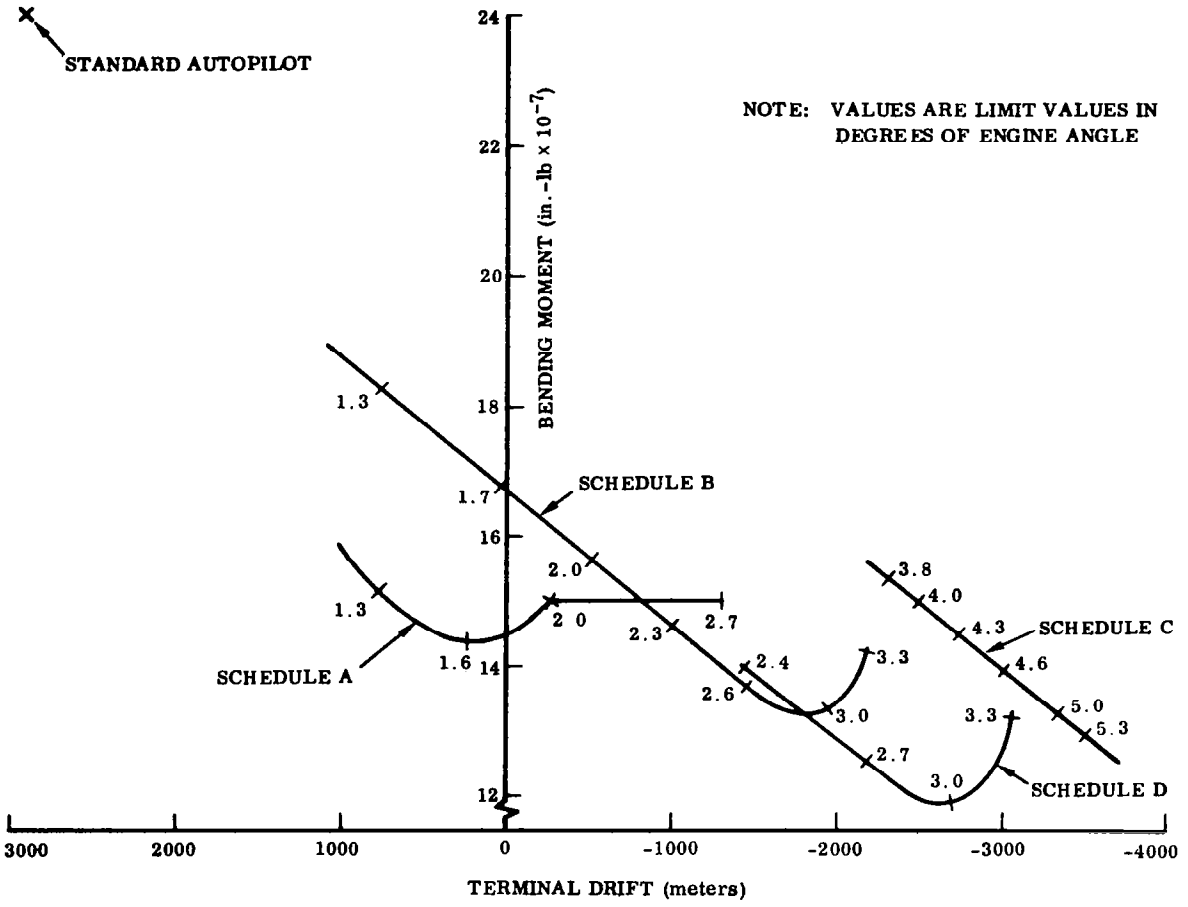

Figure 25. Maximum Bending Moment for 70-Second Wind

The ideal final result of this recommended procedure (Sections 3.1 through 3.5) is a load-relief autopilot which satisfies all the constraints and reaches or exceeds its criteria or goal. However, an analysis of this magnitude usually requires iteration between various phases to produce a final result. This final result reflects compromises in criteria and/or constraints but is the best available within the current state of the art.

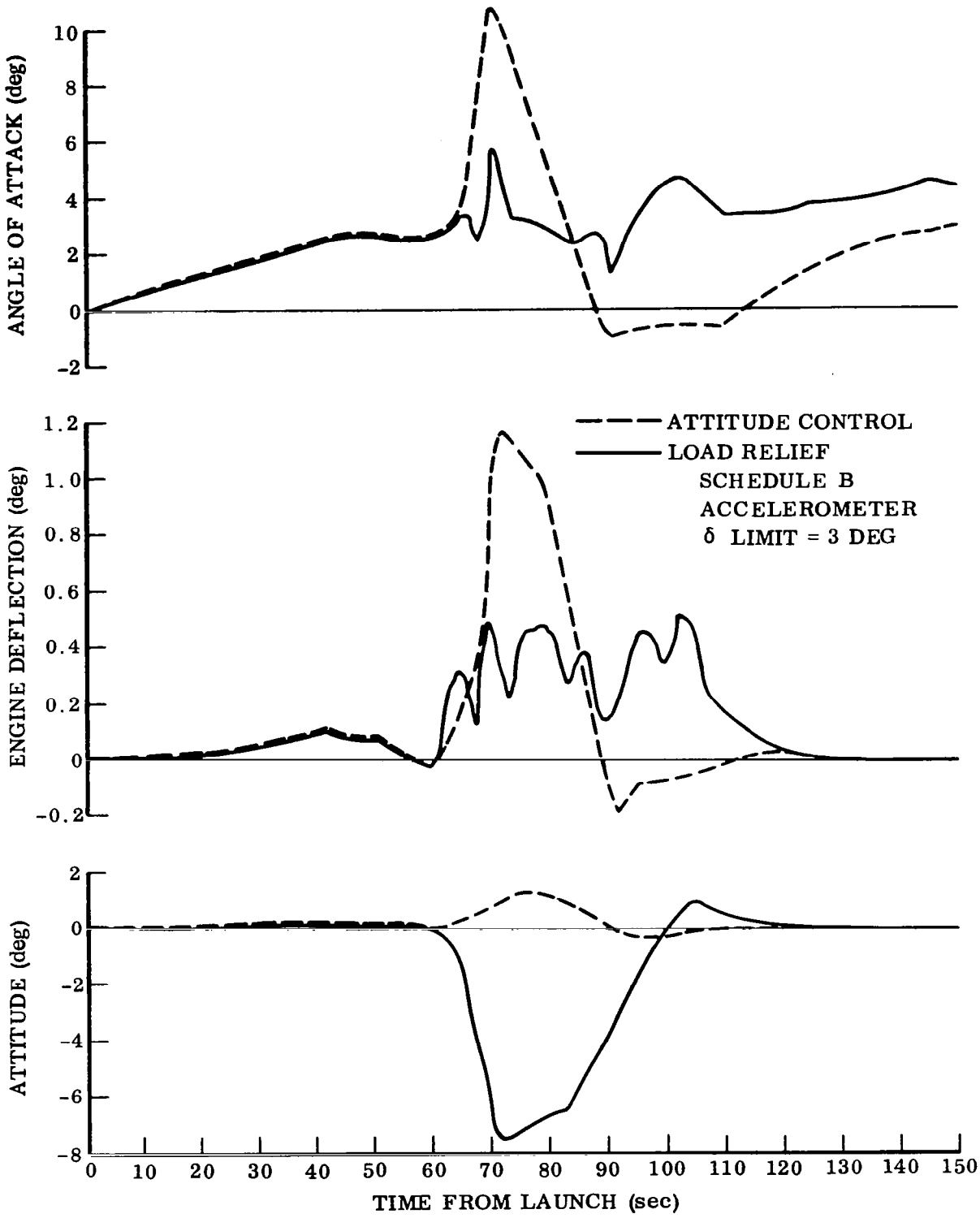

Figure 26a. Vehicle Responses to 70-Second Wind

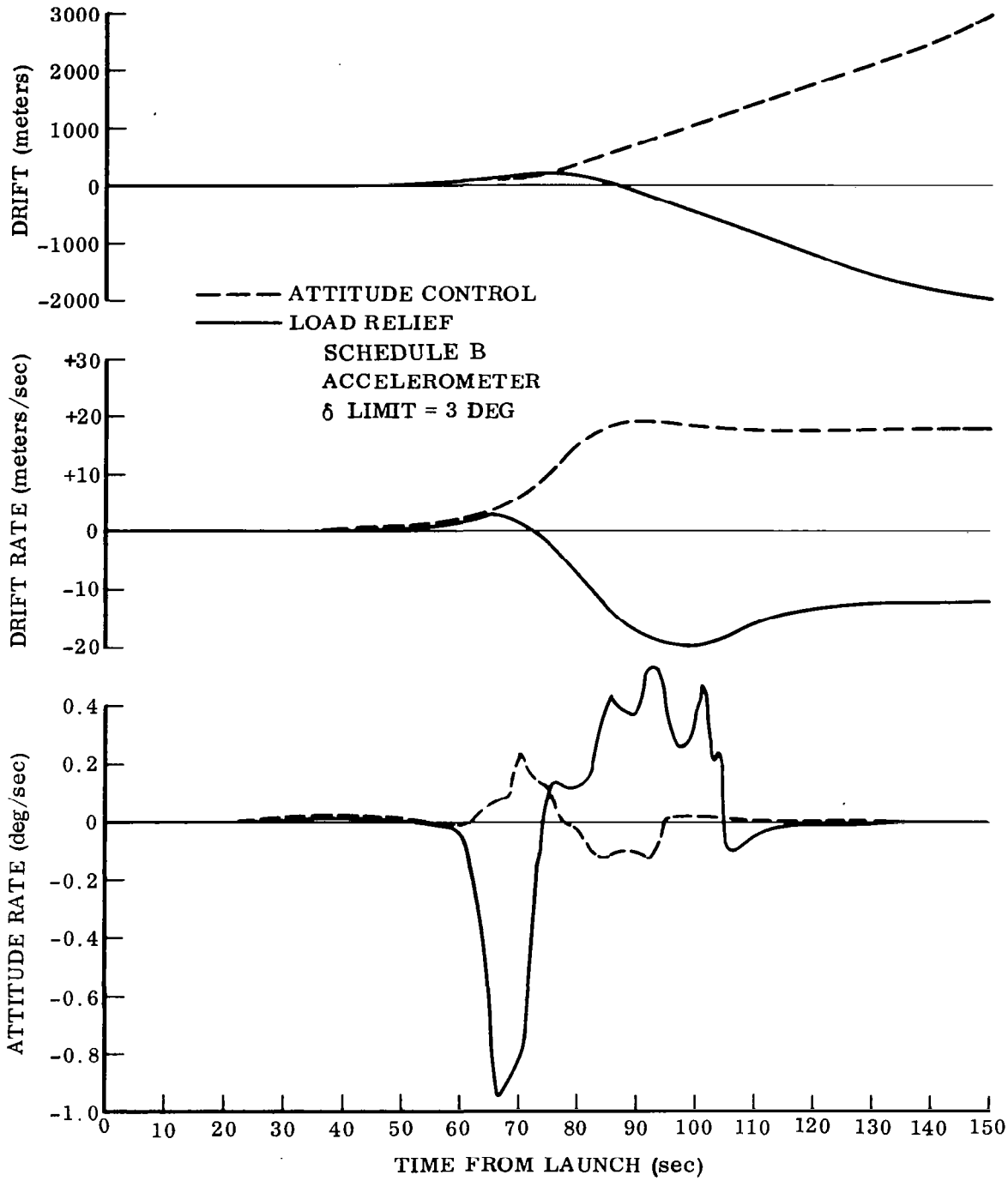

Figure 26b. Vehicle Responses to 70-Second Wind (contd)

4. REFERENCES

1. Greensite, A. — Design Criteria for Control of Space Vehicles, Vol III, Part 1, Attitude Control During Launch, Convair division of General Dynamics Report GDC-DDE66-028, 5 August 1966.

2. Hoelker, R. F. — Theory of Artificial Stabilization of Missiles and Space Vehicles with Exposition of Four Control Principles, George C. Marshall Space Flight Center, Technical Note NASA TN D-555, June 1961.

3. Russ, E. — A Study of Load Alleviation in Thrust-Vector-Controlled Boost Vehicles, Part 1, Use of Body-Fixed Sensor Control Loops, Convair division of General Dynamics Report ERR-AN-048, 3 May 1961.

4. Harmon, J. P., and Redus, J. R. — An Analysis of Two Linear Drift Minimum Control Systems Applied to Saturn V Class Vehicles, George C. Marshall Space Flight Center, Aero-Astrodynamics Internal Note R-AERO-IN-45-63, 29 October 1963.

5. Harris, R. — Atlas/Centaur/AC-5 Analog/Digital Load Reduction Autopilot Study, Convair division of General Dynamics Report GDA-BTD64-058, 13 February 1964.

6. Holt, R. L., Ringland, R. F., and Wilson, L. G. — Atlas/Centaur Load Reduction Autopilot System Study, Convair division of General Dynamics Report GD/A 63-0554, 12 August 1963 (Confidential), Addendum 1, 31 March 1964 (Unclassified).

7. Burke, W. H. and Storms, A. D. — Aerodynamic Load Reduction Techniques for Large Elastic Launch Vehicles: A Comparative Study, IEEE Convention Record, Part 7, 1964.

8. Decker, D. W., Echols, F. L., Rasch, J. E., and Sloan, M. A. — Stability and Response Comparisons of Drift Minimizing Control Laws for Saturn V Class Vehicles, Northrop Space Laboratories, NSL R&A Technical Memo No 26, 15 September 1964.

9. Gates, R. M. — A Study of Load Alleviating Control Systems for Large Launch Vehicles, The Boeing Company, Technical Summary Report, February 1965.

10. Coyne, G. W. — Nonlinear Accelerometer Feedback for Load Relief, Lockheed Missiles and Space Company, Huntsville Research and Engineering Center, Technical Memorandum TM-54/30-72, December 1965.

11. Rheinfurth, M. H. — The Alleviation of Aerodynamic Loads on Rigid Space Vehicles, AMS/AIAA Paper No. 66-350, 28 March 1966.

12. Dashiell, J. N. — Synthesis of an Optimal Load-Relief Control System, Lockheed Missiles and Space Company, Huntsville Research and Engineering Center, Technical Memorandum TM-54/30-90, March 1966.

13. Greensite, A. L. — Design Criteria for Control of Space Vehicles, Vol II, Part 1, Linear Systems, Convair division of General Dynamics Report GDC-DDE66-019, 25 April 1966.

APPENDIX

ATMOSPHERIC DISTURBANCES AND THEIR EFFECT ON VEHICLE LOADING

NOMENCLATURE

C_D	Drag coefficient	N.D.
C_{D_i}	Cumulative drag coefficient to the ith station	N.D.
$C_{N/\alpha}$	Normal force coefficient per pitch plane angle of attack	1/rad
C_{N0}	Normal force coefficient at zero pitch plane angle of attack	N.D.
$C_{Y/\beta}$	Yaw force coefficient per yaw plane angle of attack	1/rad
C_{Y0}	Yaw force coefficient at zero yaw plane angle of attack	N.D.
$C_{S\alpha}$	Shear coefficient per pitch plane angle of attack	1/rad
C_{S0}	Shear coefficient at zero pitch plane angle of attack	N.D.
$C_{S\ddot{z}}$	Shear coefficient per unit normal acceleration	lb/ft/sec^2
$C_{S\ddot{\theta}}$	Shear coefficient per unit pitch plane rotational acceleration	lb/rad/sec^2
$C_{M\alpha}$	Moment coefficient per pitch plane angle of attack	ft/rad
C_{M0}	Moment coefficient at zero pitch plane angle of attack	ft
$C_{M\ddot{z}}$	Moment coefficient per unit normal acceleration	ft-lb/ft/sec^2
$C_{M\ddot{\theta}}$	Moment coefficient per unit pitch plane rotational acceleration	ft-lb/rad/sec^2
F	Force	lb
I	Moment of Inertia	lb-sec^2-ft
K_A	Autopilot transfer functions described in text	rad/rad
K_R		rad/rad/sec
K_C		1/sec
K_{LR}		Variable

M_i	Mass supported by structure at i^{th} station	lb-sec^2/ft
M_N	Mach number	N.D.
M_T	Total mass of vehicle	lb-sec^2/ft
P	Axial load	lb
S	Shear	lb
S_R	Reference area	ft^2
T	Thrust	lb
V	Velocity	ft/sec
V_H	Horizontal wind velocity parallel to launch azimuth	ft/sec
V_L	Horizontal wind velocity normal to launch azimuth	ft/sec
V_S	Speed of sound at a particular altitude	ft/sec
X	Sensed parameter for load-relief autopilot	variable
h	Altitude	ft
m_i	Lumped mass at i^{th} station	lb-sec^2/ft
q	Dynamic pressure	lb/ft^2
t	Time	sec
x	Coordinate of longitudinal body axis	ft
y	Coordinate normal to longitudinal body axis, yaw plane	ft
z	Coordinate normal to longitudinal body axis, pitch plane	ft
α	Angle of attack, pitch plane	rad
α_g	Angle of attack, gust	rad
β	Angle of attack, yaw plane	rad
γ	Flight path angle (angle between local horizontal and velocity vector)	rad
δ	Engine gimbal angle	rad
θ	Angle between local horizontal and vehicle centerline; angle between undeformed axis and deformed axis	rad
ρ	Density	$\frac{\text{lb-sec}^2}{\text{ft}}/\text{ft}^3$
ψ	Angle between launch azimuth and vehicle centerline	rad

The main body of this report deals in launch vehicle load relief. In order to develop a better understanding of the nature of vehicle loading due to atmospheric disturbances, this appendix has been included. The reader is referred to Ref. A1 for a more complete dissertation on dynamic loads analysis during launch vehicle flight.

A.1 INTRODUCTION

The powered phase of flight through the atmosphere is a condition that often dictates design of a significant portion of the vehicle structure. Axial and lateral loads imposed during this period are functions of axial acceleration, atmospheric disturbances (winds and gusts), vehicle shape, Mach number, trajectory, and atmospheric density. Axial loads are primarily drag loads and inertial loads of the quasi-steady acceleration. Lateral loads are the result of vehicle (or structure) orientation with respect to the relative air velocity. The magnitudes of lateral loads are functions of angle of attack and dynamic pressure. The angle-of-attack magnitude is primarily a result of vehicle trajectory, atmospheric disturbances, and autopilot configuration. Vehicle shape, Mach number, and atmospheric density determine the distribution of drag and lateral loads. Also, vehicle shape and Mach number determine the type of air flow and can lead to phenomena such as buffeting, which will not be discussed herein.

Axial load values are relatively straightforward computations of trajectory parameters such as acceleration, Mach number, altitude, dynamic pressure, and weight. Lateral load calculations are also straightforward computations of these parameters with the addition of angle of attack; however, the angle of attack is a function of atmospheric disturbances which are random in nature. Thus, the major problem in lateral loads is the determination of wind criteria. Once these are established, analytical techniques are used to obtain the loads.

Winds are large-scale movements of air persisting for a period of time considerably longer than the vehicle flight and extending over a significant altitude range. Figure A1a presents a detailed wind profile taken by the smoke-trail method. Figure A1b shows the same wind as measured by a balloon system and also the averaged (smoothed) smoke-trail data.

Wind speeds at launch are small (compared with wind speeds at altitude) and increase with altitude in an uneven manner, reaching a peak in the 25,000- to 40,000-foot-altitude range. The wind speed then decreases up to approximately 100,000 feet where it starts to increase. Little data are available on wind speeds above 60,000 feet; however, loading due to wind above this altitude is quite small because of low dynamic pressure and is rarely considered. Gusts are defined as short-period disturbances in the air and are usually considered to account for the profile detail not measured by the balloon system (see Fig. A1). For highly accurate wind profiles only the elastic response to gust is generally considered. For most launch vehicles the time span of exposure to a discrete gust is on the order of less than one second. While data on gusts are meager they are usually considered to exist in the same altitudes in which high wind speed is prevalent.

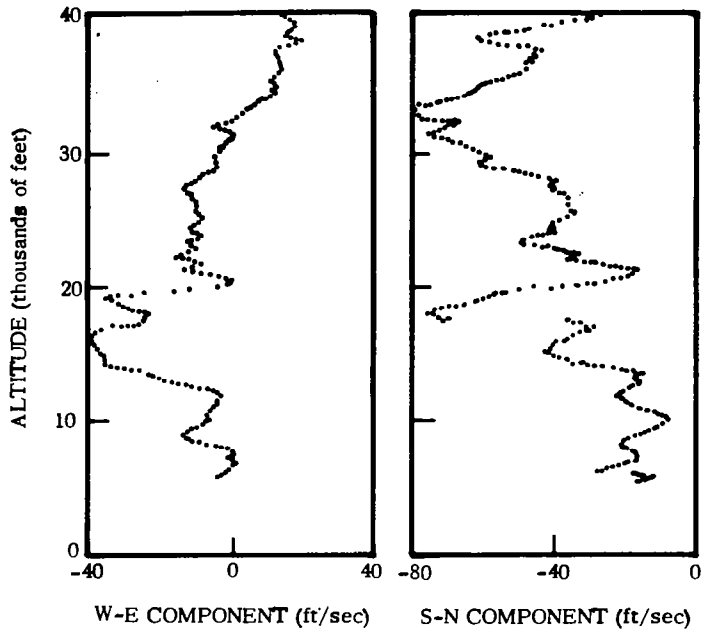

a. Measured Smoke-Trail Winds

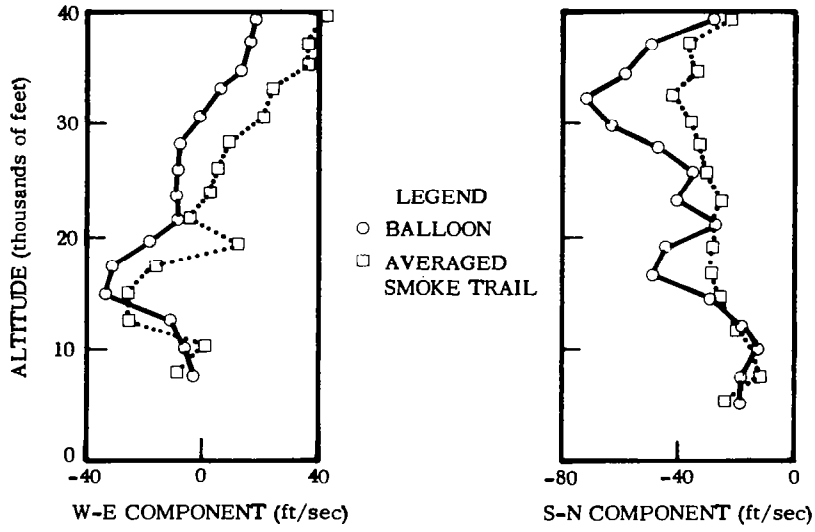

b. Balloon and Averaged Smoke-Trail Winds

Figure A1. Typical Wind Profile

The general procedure for calculation of lateral loads consists of a trajectory simulation through a specified wind and gust profile (or profiles) to obtain the required parameters for loads. Generally rigid-body plus aeroelastic loads due to wind are obtained and added to the loads due to elastic response to a gust.

A.2 DEVELOPMENT OF WIND CRITERIA

The development of wind criteria has taken two approaches. One approach is to do a statistical analysis of the wind data and then develop synthetic wind profiles. Loads are then obtained by application of these profiles. The first widely used profile was the Sissenwine profile developed in the early 1950's. It is given in Ref. A2 and has since been modified by Ref. A3. Currently, the most widely used synthetic profile criteria are the Marshall Space Flight Center (MSFC) criteria. MSFC has developed a computer analysis of wind data that yields, for a given launch site and azimuth, wind speed and shear data from which synthetic profiles are constructed. References A4 and A5 are examples of the criteria generated by MSFC.

The second approach is to obtain loads for each wind sounding in a set of soundings and then do a statistical analysis of the loads. This approach is referred to as a statistical load survey. The original development of this approach was done by Avidyne Research, Inc., and reported in Refs. A6, A7, and A8. The approach requires a trajectory simulation for each sounding and hence entails a considerable amount of computer time. To decrease the computer time involved, several approximate methods have been developed. The influence coefficient method uses an influence coefficient matrix derived from "basic" profiles, i.e., triangular spike, ramp, etc. The vector of wind speeds from a particular wind sounding is multiplied by an appropriate influence coefficient matrix to obtain loads for that sounding. The method was studied by Avidyne and the results are given in Ref. A9. Clingan (Ref. A10) uses a closed-form trajectory solution to reduce computer time for the statistical load survey. The trajectory solution is obtained by using perturbation equations and neglecting rotational rate and acceleration. Van der Maas (Ref. A11) developed a method that uses two basic parameters of a wind sounding to obtain loads on a vehicle. The parameters are maximum wind velocity and the integral of the wind velocity from ground to the altitude of the maximum wind velocity.

The statistical load survey, as developed by Avidyne, is the most accurate method since no assumptions are made concerning either the trajectory simulation or the correlation between wind data and resulting loads (as is done for synthetic profiles). Avidyne investigated the several methods and compared them, using the statistical load survey as the standard of comparison. The results are given in Ref. A9. In order of decreasing accuracy, Avidyne ranked the methods as follows: influence coefficient method, Clingan's method, discrete profiles, and Van der Maas method.

The data available on which to base gust criteria are sparse. References A12 and A13 give some of the available data. These data were gathered by aircraft flying

horizontally and then measuring the aircraft vertical accelerations. Randomness of the data is not necessarily established, and correlation with wind speed is lacking. Also, most of the data were taken below a 20,000-foot altitude; however, peak launch vehicle loads generally occur in the 25,000- to 40,000-foot-altitude range. Thus, assumptions have to be made when applying these data to launch vehicles. Currently, the gust criteria cover any short-period disturbance not adequately measured during the wind sounding. As wind soundings become more accurate, and especially as the incremental altitude for measurement becomes smaller, the wind sounding will include more and more of what is now included as gust. Thus the question of improving gust criteria will probably be resolved not by gust measurements but by highly accurate wind soundings.

Analysis for loads due to atmospheric disturbances consists of a five or six degree-of-freedom rigid-body trajectory simulation through the design wind profile. The parameters from the simulation are used to calculate vehicle loads. With large boosters the trajectory simulation should include the low-frequency bending modes (less than 2 Hz) since these modes can be excited by the wind profile. As wind profile representation improves, it will be necessary to include elastic modes for most vehicles in the trajectory simulation. Reference A14 presents work examining the inclusion of elastic modes in the simulation with detailed wind profiles. Here the problem is not one of methodology but one of determining a sufficiently accurate procedure with economical execution.

The gust effects are added by either of two methods: 1) adding the gust profile to the wind profile to obtain rigid-body gust loads, and performing an elastic analysis with the gust only to obtain those loads due to elastic response, and 2) calculating rigid and elastic body gust loads independently of the wind profile and adding these to the loads resulting from the wind profile. The end result is essentially the same, and use of either method is usually at the discretion of the analyst.

A.3 QUASI-STEADY FLIGHT LOADS

The term, "quasi-steady flight loads," is used to describe loads and/or response produced by long-period maneuvers and disturbances. The primary sources are winds, autopilot configuration, and steering to accomplish a desired trajectory, either by a predetermined pitch program or by a guidance system. The period is sufficiently long that the vehicle is characterized elastically as deflecting statically and possibly responding in its lower frequency normal modes. The gross wind speed changes take place during altitude spans of several thousand feet; however, recent wind data are providing wind detail for altitude spans of less than a hundred feet.

A.3.1 Analytical Approach

The initial step in obtaining quasi-steady flight loads is to simulate, analytically, the trajectory so that the required trajectory parameters can be obtained. While all

trajectory simulations have the same basic analytical features, they usually differ in the detail of these features. Factors influencing the detail composition of a trajectory simulation include optional ways of calculating some parameters, the intended use of the simulation (loads analysis, performance analysis, etc.), the degree of complexity deemed necessary to provide accurate results, and the coordinate system(s) used. With this in mind, the basic form and equations will now be outlined. The vehicle coordinate system is shown in Fig. A2. The vehicle forces are illustrated in Fig. A3.

The equations of motion for the trajectory of a launch vehicle are derived in Ref. A15. An inertial reference frame, usually having its origin at and fixed to the center of the earth, is used. However, forces on the vehicle are expressed in body axes. It

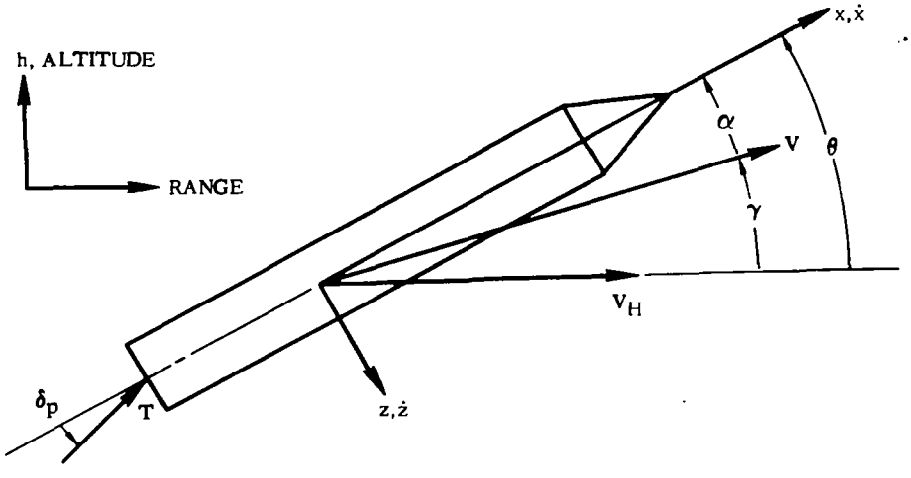

a. Pitch Plane

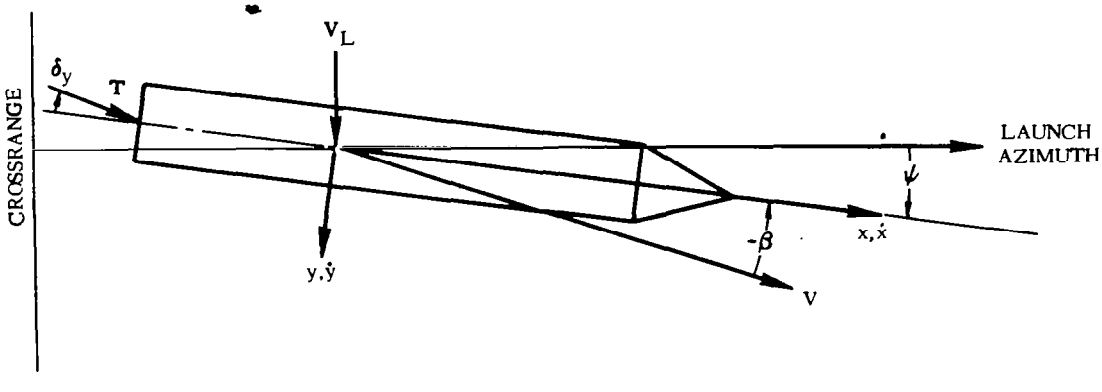

b. Yaw Plane

Figure A2. Coordinate System

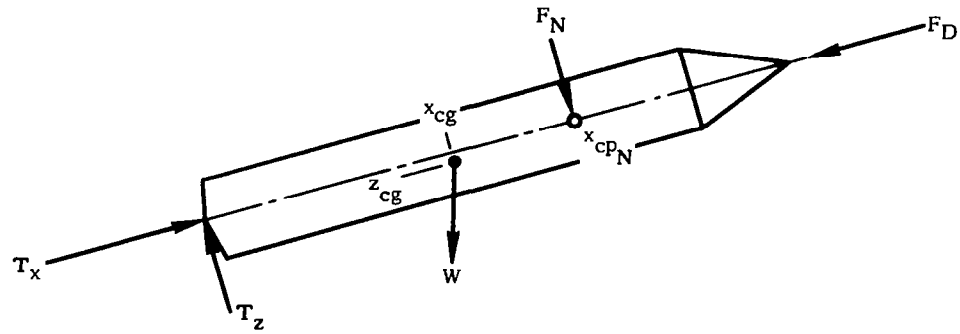

a. Pitch Plane

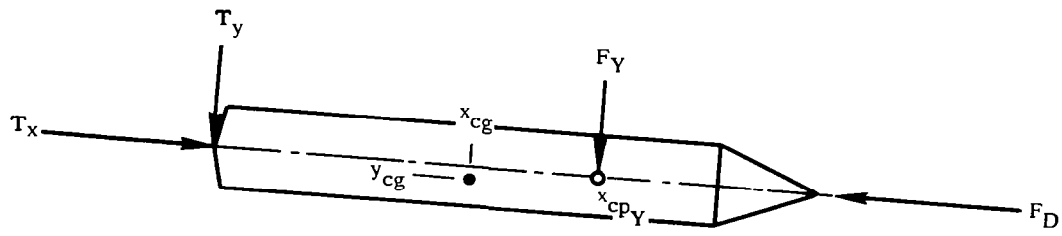

b. Yaw Plane

Figure A3. Vehicle Force Diagrams

is also desirable to fix the vehicle position relative to the launch site. Thus several coordinate systems and the accompanying coordinate transformations are needed. The range of launch vehicles while in the atmosphere is usually on the order of 20 to 30 miles; hence, a flat nonrotating earth will suffice for determining quasi-steady flight loads. The acceleration of the vehicle is obtained by consideration of the thrust, aerodynamic, gravitational, and centrifugal forces. The resultant acceleration produces, over its time integral, a vehicle velocity, V, which is relative to still air and a fixed launch point. The flight path angle, γ, is defined as the angle between the horizontal datum at a fixed launch point and the vehicle velocity vector. The altitude is given by

$$h = \int V \sin \gamma \, dt \tag{A1}$$

In vehicle coordinates, the axial, lateral, and vertical velocities with respect to the atmosphere are (assuming a flat nonrotating earth and α and β to be small)

$$\left.\begin{aligned} \dot{x} &= V - V_H \cos\theta \\ \dot{y} &= V \sin\beta - V_L \cos\psi \\ \dot{z} &= V \sin\alpha - V_H \sin\theta \end{aligned}\right\} \tag{A2}$$

The Mach number is

$$M_N = \frac{\sqrt{\dot{x}^2 + \dot{y}^2 + \dot{z}^2}}{V_S} \tag{A3}$$

The dynamic pressure is

$$q = \frac{1}{2}\rho(\dot{x}^2 + \dot{y}^2 + \dot{z}^2) \tag{A4}$$

The angles of attack in the pitch and yaw planes are

$$\left.\begin{aligned} \alpha &= \frac{\dot{z}}{\dot{x}} \text{ (pitch plane)} \\ \beta &= \frac{\dot{y}}{\dot{x}} \text{ (yaw plane)} \end{aligned}\right\} \tag{A5}$$

The total aerodynamic drag, normal, and yaw forces are

$$\left.\begin{aligned} F_D &= q S_R C_D \\ F_N &= q S_R (\alpha C_{N/\alpha} + C_{N0}) \\ F_Y &= q S_R (\beta C_{Y/\beta} + C_{Y0}) \end{aligned}\right\} \tag{A6}$$

The normal and yaw centers of pressure are defined as x_{cp_N} and x_{cp_Y}. They are functions of M_N and α or β as appropriate. The weight is the weight at launch minus all propellant weight expended and jettisoned weight as appropriate. The centers of gravity (x_{cg}, y_{cg}, and z_{cg}) and the moments of inertia, I_{yy} (pitch) and I_{zz} (yaw), are easily computed. The information required for the autopilot simulation is now available. It is simply stated here that the autopilot will provide engine angles in pitch, δ_P, and in yaw, δ_Y, and the angular attitude of the vehicle in pitch, θ, and in yaw, ψ. The axial, lateral, and normal thrust forces are

$$\left.\begin{aligned} T_x &= T\cos\delta_P\cos\delta_Y \\ T_z &= -T\delta_P \\ T_y &= T\delta_Y \end{aligned}\right\} \qquad \text{(A7)}$$

The thrust, aerodynamic, and inertial forces can now be combined to obtain the total acceleration vector; the computational loop is complete. The problem is one of numeric integration, and standard techniques are employed.

The function of the autopilot, standard or load relief is threefold:

a. Stabilize the vehicle.

b. Ensure reasonable rapid response to guidance commands.

c. Provide an adequate safety margin for anticipated atmospheric disturbances.

The load-relief autopilot is basically the standard autopilot with an additional feedback loop or loops. The form considered herein is shown in Fig. A4. The autopilot can therefore be represented by the engine gimbal quantities in the following form:

$$\left.\begin{aligned} \ddot{\delta}_P &= f\,(K_A, K_R, K_C, \theta_G, \dot{\theta}_G, \dot{\theta}_c, K_{L_R}, X) \\ \dot{\delta}_P &= \int \ddot{\delta}_P\,dt \\ \delta_P &= \int \dot{\delta}_P\,dt \end{aligned}\right\} \qquad \text{(A8)}$$

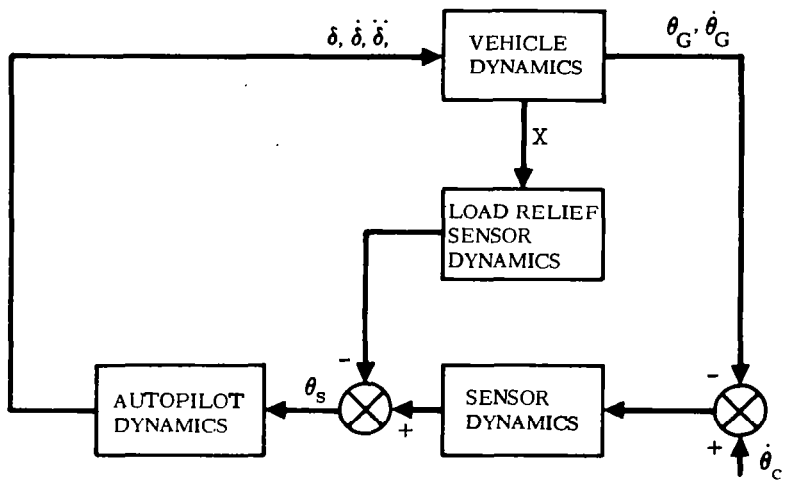

Figure A4. Load-Relief Autopilot Block Diagram

With the trajectory parameters available, the shear and bending moment distributions for the vehicle can now be calculated. Two approaches can be taken in calculating rigid-body shear and bending moment due to airloads. One approach is to apply the airloads due to αq (or βq) from the trajectory and to balance moments with the engine, so that the rotational acceleration and rate are zero. This approach, referred to as the "trimmed vehicle condition," is a good approximation and is widely used. Here, the aerodynamic normal force distribution along the vehicle is lumped at panel points in the same manner as the weight is lumped. The required engine angle is

$$\delta = \frac{F_N (x_{cp_N} - x_{cg})}{T (x_T - x_{cg})} \tag{A9}$$

The normal acceleration is

$$\ddot{z} = \frac{T\delta + F_N}{M_T} \tag{A10}$$

The net force at each panel point is

$$F_i = q S_R \left[\alpha C_{N/\alpha_i} + C_{N0_i}\right] - m_i \ddot{z} \tag{A11}$$

When $x_i = x_T$ the thrust force $T\delta$ is added. The shear and bending moment distribution can now be obtained in the classical manner of summation and integration of forces. When the mathematical model contains branch beams, the analyst must be careful to sum and integrate correctly.

The second approach is to calculate shear and bending moment coefficients for aerodynamic forces, translational accelerations, and rotational accelerations and to use these in conjunction with trajectory parameters to obtain shear and bending moment. The equations for shear and bending moment are

$$\left.\begin{aligned} S_i &= q S_R (\alpha C_{S\alpha_i} + C_{S0_i}) + \ddot{z} C_{S\ddot{z}_i} + \ddot{\theta} C_{S\ddot{\theta}_i} \\ M_i &= q S_R (\alpha C_{M\alpha_i} + C_{M0_i}) + \ddot{z} C_{M\ddot{z}_i} + \ddot{\theta} C_{M\ddot{\theta}_i} \end{aligned}\right\} \tag{A12}$$

The quasi-steady axial loads come from the vehicle axial acceleration and aerodynamic drag. The axial load at the ith station is

$$P_i = M_i \ddot{x} + q S_R C_{D_i} \tag{A13}$$

The foregoing discussion on loads applies to a rigid vehicle. Aerospace vehicles are usually sufficiently flexible to have considerable deflection under limit (design)

load. In the case of air loads, this deflection causes changes in local angle of attack and, in turn, the load distribution on the vehicle. The change in load distribution again changes the local angle of attack. Thus an iterative process is begun which rapidly converges on a suitable airload distribution. Experience to date indicates that inclusion of quasi-static aeroelastic effects in analysis can give loads for aerospace vehicles of 5 to 20 percent over rigid vehicle loads.

Two methods employed for obtaining static aeroelastic effects are: 1) finding deflections and changes in load using the flexibility matrix and 2) obtaining deflections and changes in load by using normal mode theory. These methods are presented in detail in Ref. A1.

A.3.2 Illustrative Example

A trajectory simulation, with a wind included, of the Atlas/Centaur/Surveyor vehicle is used to illustrate the determination of vehicle response and loads due to winds. The wind used was picked at random simply for illustration; hence, no significance is to be attached to the results for design purposes or for launch probability considerations. Simulations were made with an attitude control law (standard autopilot) and a load-relief control law to show the effect of these laws.

The trajectory simulation used is, in its basic form, that described in subsection A.3.1. Propellant sloshing is not included. A linear control system is employed, even though the actual Atlas control system is nonlinear. The vehicle and aerodynamic data used are those employed in the wind monitoring procedure for the Atlas/Centaur/Surveyor vehicle. The wind speed and direction are shown in Fig. A5.

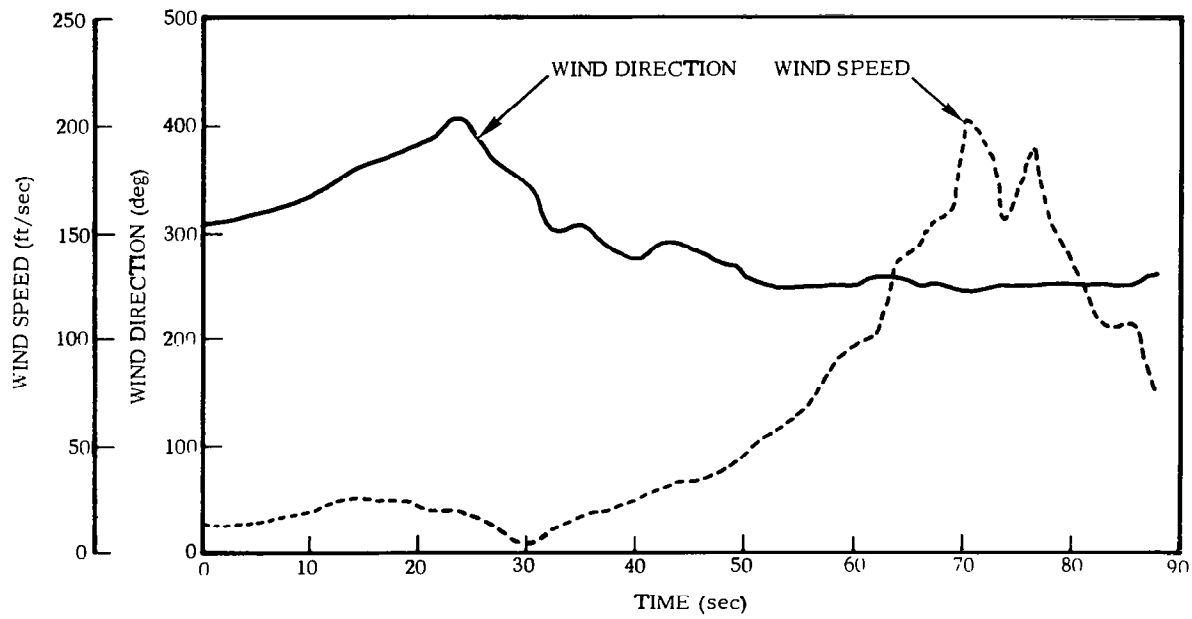

Figure A5. Wind Speed and Direction Time History

The wind loads, which included the static aeroelastic effects, have been calculated for the pitch and yaw planes and then summed vectorially. The translational accelerations, shears, and bending moments at the Centaur/Surveyor interface are shown in Fig. A6. The loads using the load-relief autopilot simulation are, of course, significantly lower at the peaks than with the standard autopilot.

A.4 GUST RESPONSE

A.4.1 Analytical Approach

The equations for gust response are presented in Ref. A1. These basic equations are applicable to any vehicle; however, the autopilot equations are for a particular form of autopilot and may need modification for the particular vehicle under analysis. The general approach is well illustrated and little additional work should be required to accommodate various autopilot representations.

Two types of gusts can be considered in gust response analysis to determine gust angle of attack. For an "immersion" gust the vehicle is subjected to the same gust velocity over its entire length. In this case, α_g is constant with respect to vehicle station and it varies in time according to the gust shape. Another representation for aerodynamic forces is a "penetration" gust, for which the forces are applied along the vehicle as it penetrates the gust or shear layer. For a penetration gust the α_g is a function of vehicle station as well as time.

Because of the specialized nature of this analysis area the reader is referred to Ref. A1 for detailed techniques. However, the following example should provide some insight into the nature of these calculations.

A.4.2 Illustrative Example

The gust response of the Atlas/Centaur/Surveyor vehicle in the yaw plane at 60 seconds flight time has been obtained as an illustration of gust response analyses. The gust wavelength has been "tuned" in the sense that the vehicle transit time through the gust has produced (on the computer) the maximum response in a particular mode; here, the third bending mode. The transit time for maximum excitation of a particular mode is nearly equal to the period of that mode. In this example, with a third mode period of 0.088 second and vehicle velocity of 1128 feet per second, the "tuned" wavelength is 100 feet. Both "immersion" and "penetration" gusts have been used with "1-cosine" gust profiles. The gust, in this example, is applied normal to the vehicle longitudinal axis.

The spacecraft response is greater at short gust wavelengths due to higher response of the second, third, and fourth bending modes at these wavelengths. These modes produce high translational and rotational accelerations at the ends of a vehicle; however, the first bending mode and the rigid-body modes produce the highest bending moments

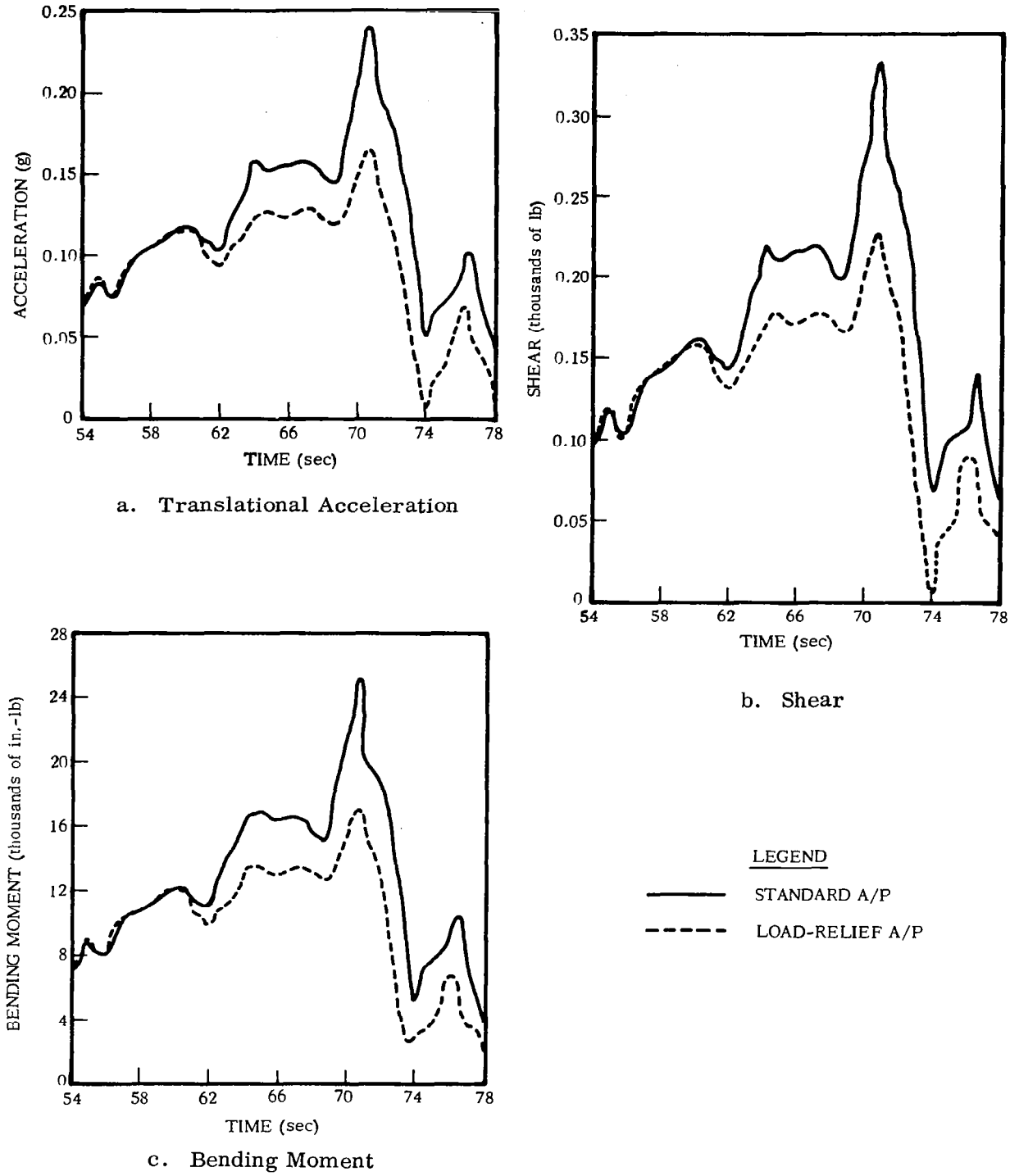

Figure A6. Centaur/Surveyor Interface Loads Due to Wind

in the central portion of a vehicle. The lower frequency modes have peak gust response at longer wavelengths. A 30-foot-per-second gust velocity, which is rather unrealistic for such a short wavelength, has been used in this illustration.

The translational accelerations, rotational accelerations, shears, and bending moments at the Centaur/Surveyor interface are shown in Fig. A7. The dominant response is in the tenth mode (third bending mode at 11.33 Hz) with some structurally significant response in the lower modes. Since the gust wavelength was set equal to the period of the tenth mode, this behavior is to be expected. The bending moments at the Atlas/Centaur interface are presented in Fig. A8. Here the dominant response is in the sixth mode (second bending mode at 6.24 Hz). The difference in the characteristics of the bending moments at the two interfaces (see Figs. A7d and A8) is attributable to the type of loading encountered. At the Centaur/Surveyor interface the loads are inertial loads due to spacecraft response. This condition illustrates the variation in response characteristics that can occur for various points on the vehicle. The loads from both the "immersion" and "penetration" gusts shown for the Atlas/Centaur/Surveyor vehicle are quite similar; however, there is no reason to expect this similarity for other atmospheric descriptions or space vehicle configurations.

A.5 COMBINED LOADS

The loads discussed previously, and other minor dynamic loads neglected herein, need to be combined for design purposes and for comparison with allowable loads.

In summary, the following procedure should be followed for calculating loads caused by atmospheric disturbance.

a. Wind and gust criteria for design must be specified.

b. Proceed with rigid trajectory simulation using a nonrotating flat earth model and a simplified rigid body autopilot.

c. Calculate wind loads using a trimmed vehicle condition or the coefficient method.

d. Calculate gust loads with immersion or penetration gust.

e. Calculate axial inertial and drag loads.

f. Calculate other loads such as center-of-gravity offset and misalignment effects and trajectory dispersions (if necessary).

g. Combine loads using the methods of Ref. A1.

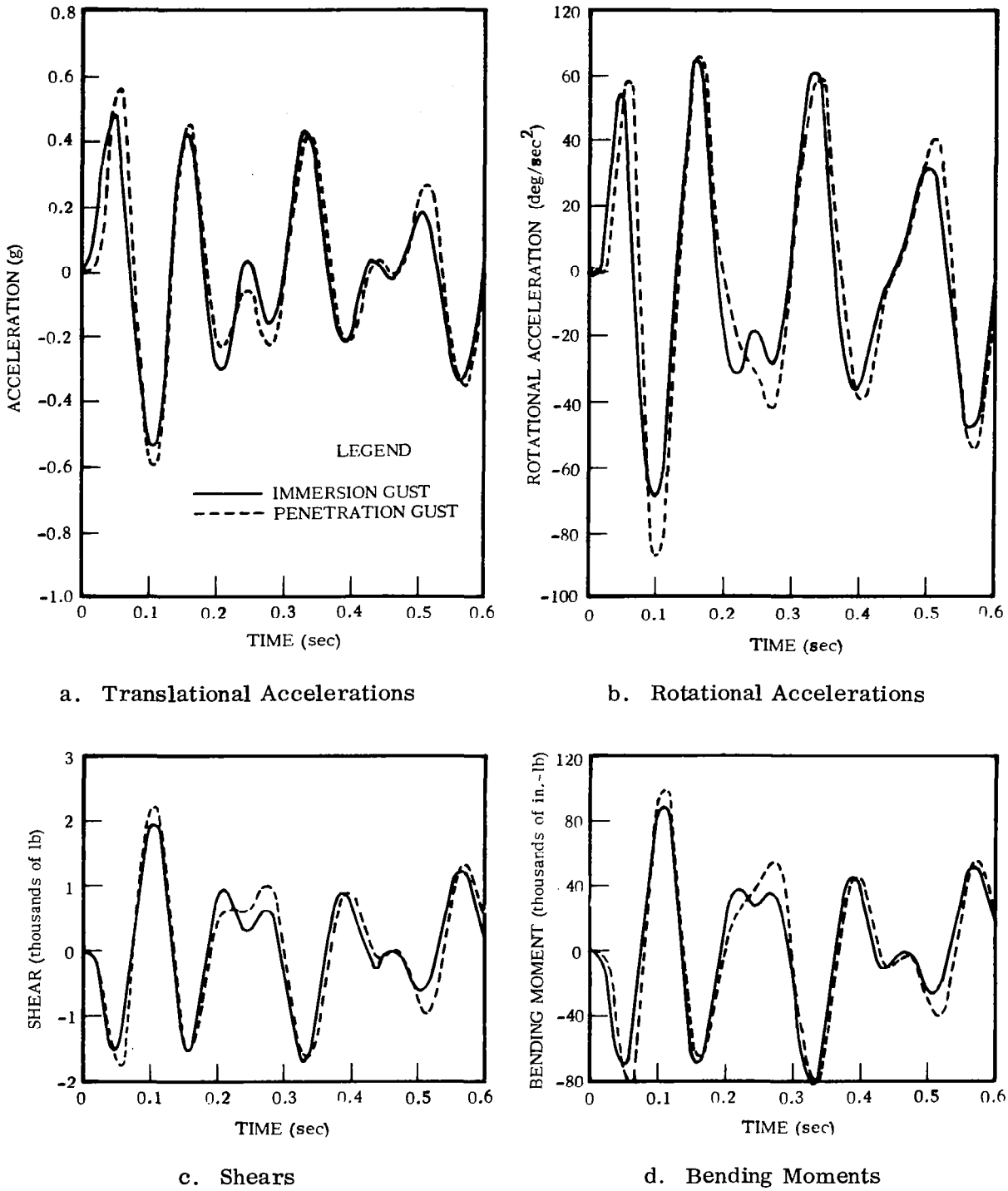

a. Translational Accelerations

b. Rotational Accelerations

c. Shears

d. Bending Moments

Figure A7. Centaur/Surveyor Interface Loads Due to Gust

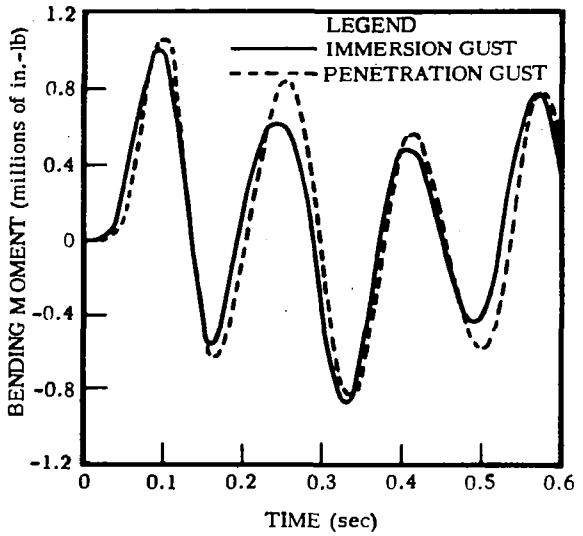

Figure A8. Atlas/Centaur Interface Bending Moments Due to Gust

A.6 REFERENCES

A1. Schuett, R. H., Appleby, B. A., and Martin, J. D. — Dynamic Loads Analysis of Space Vehicle Systems, Launch and Exit Phase, Convair division of General Dynamics Report GDC-DDE66-012, June 1966.

A2. Sissenwine — Wind Speed Profile, Wind Shear, and Gusts for Design of Guidance Systems for Vertically Rising Air Vehicles, AFCRC TN-54-22, November 1954.

A3. Sissenwine — Revised 1% Synthetic Wind Profile, AFCRC, June 1959.

A4. Scoggins and Vaughan — Description of Wind Shears Relative to a Missile/Space-Vehicle Axis and a Presentation of the Cape Canaveral, Florida, 95 and 99 Percent Probability Level Standardized Wind Profile Envelopes (1-80 km) and Associated Wind Shears for Use in Design and Performance Studies, MSFC MTP-Aero-61-48, 8 June 1961.

A5. Daniels — Revision of Natural Environmental Design Criteria, In-Flight Wind Conditions, Saturn C-1, Block II Vehicle, MSFC M-Aero-G-35-62, 19 October 1962.

A6. Mazzola, L. L., Hobbs, N. P., and Criscione, E. S. — Wind, Wind Shear, and Gust Design Criteria for Vertically Rising Vehicles as Recommended on the Basis of Montgomery, Ala., Wind Data (U), WADD TR 61-99 (AD 333174), Avidyne Research, Inc., August 1962 (Secret).

A7. Mazzola, L. L., Putukian, J., Criscione, E. S., and Hobbs, N. P. — Wind, Wind Shear, and Gust Design Criteria for Vertically Rising Vehicles as Recommended on the Basis of Wind Data from Eleven United States and Foreign Locations (U), ADS-TDR-62-908 (AD 338892), Avidyne Research, Inc., June 1963 (Secret).

A8. Hobbs, N. P., Criscione, E. S., Mazzola, L. L., and Frassinelli, G. J. — Development of Interim Wind, Wind Shear, and Gust Design Criteria for Veritically Rising Vehicles (U), WADC TR 59-504 (AD 316913), Avidyne Research, Inc., July 1959 (Secret).

A9. Hobbs, N. P., Criscione, E. S., and Ayvazian — Simplified Analytical Methods for Use in Preliminary Design of Vertically Rising Vehicles Subjected to Wind Shear Loads, FDL-TDR-64-8, Part 1, Avidyne Research, Inc., May 1964.

A10. Clingan, B. E. — "A Rapid Method for Determining Wind Shear Design Loads Based on a Set of Measured Profiles," Proceedings of the National Symposium on Winds for Aerospace Vehicle Design, Vol II, pp 49-69, Air Force Surveys in Geophysics No. 140 (AD 275846), AFCRL-62-273 (II), March 1962.

A11. Van Der Mass, C. J. — High Altitude Wind Response of Missile Systems, Lockheed Aircraft Corporation, Missile Systems Division, Report No. LMSC-A062400 (AD 408258), 30 October 1962.

A12. Press, Meadows, and Hadlock — Estimates of Probability Distribution of RMS Gust Velocity of Atmospheric Turbulence from Operational Gust-Load Data by Random Process Theory, NASA TN 3362, March 1955.

A13. Walker and Copp — Summary of VGH and V-G Data Obtained from Piston-Engine Transport Airplanes from 1947 to 1958, NASA TN D-29, September 1959.

A14. Clingan, B. E., Gates, R. M., and Andrews, J. S. — Dynamic Loads During Boosted Flight, The Boeing Company, ADD-TDR-63-302, May 1963.

A15. Greensite, A. L. — Design Criteria for Control of Space Vehicles, Vol. I, Part 3, Trajectory Equations, Convair division of General Dynamics Report GDC-DDE65-058, November 1965.

NASA-Langley, 1967 —— 31 CR-833

"The aeronautical and space activities of the United States shall be conducted so as to contribute . . . to the expansion of human knowledge of phenomena in the atmosphere and space. The Administration shall provide for the widest practicable and appropriate dissemination of information concerning its activities and the results thereof."

—NATIONAL AERONAUTICS AND SPACE ACT OF 1958

NASA SCIENTIFIC AND TECHNICAL PUBLICATIONS

TECHNICAL REPORTS: Scientific and technical information considered important, complete, and a lasting contribution to existing knowledge.

TECHNICAL NOTES: Information less broad in scope but nevertheless of importance as a contribution to existing knowledge.

TECHNICAL MEMORANDUMS: Information receiving limited distribution because of preliminary data, security classification, or other reasons.

CONTRACTOR REPORTS: Scientific and technical information generated under a NASA contract or grant and considered an important contribution to existing knowledge.

TECHNICAL TRANSLATIONS: Information published in a foreign language considered to merit NASA distribution in English.

SPECIAL PUBLICATIONS: Information derived from or of value to NASA activities. Publications include conference proceedings, monographs, data compilations, handbooks, sourcebooks, and special bibliographies.

TECHNOLOGY UTILIZATION PUBLICATIONS: Information on technology used by NASA that may be of particular interest in commercial and other non-aerospace applications. Publications include Tech Briefs, Technology Utilization Reports and Notes, and Technology Surveys.

Details on the availability of these publications may be obtained from:

SCIENTIFIC AND TECHNICAL INFORMATION DIVISION

NATIONAL AERONAUTICS AND SPACE ADMINISTRATION

Washington, D.C. 20546